

Diss. ETH No. 16887

Observations and Models of the Dynamical Evolution of Solar Flares

A dissertation submitted to the
SWISS FEDERAL INSTITUTE OF TECHNOLOGY ZURICH

for the degree of
Doctor of Natural Sciences

presented by

PAOLO C. GRIGIS
Dipl. Phys. ETH

born September 24, 1977
citizen of Onsernone TI

accepted on the recommendation of
Prof. Dr. Arnold O. Benz, examiner
PD Dr. Manuel Güdel, co-examiner
Prof. Dr. Jan O. Stenflo, co-examiner

2006

Contents

Abstract	iii
Riassunto	v
1 Introduction	1
1.1 Short History of Flare Observations	2
1.2 The Ramaty High-Energy Solar Spectroscopic Imager (RHESSI)	5
1.3 Hard X-ray Emission and Flare Spectra	6
1.3.1 Bremsstrahlung Emission	7
1.3.2 Observed X-ray Spectra	11
1.4 Hard X-ray Images and Flare Scenarios	14
1.5 Coronal Heating and Flares	15
1.5.1 Different Sizes of Solar Flares	18
1.6 RHESSI Observation of Microflares	21
2 Spectral Evolution of Solar Flares	25
2.1 Introduction	26
2.2 Observations and Data Reduction	27
2.2.1 Event Selection	27
2.2.2 Data Reduction and Analysis	28
2.2.3 Automatic Spectral Fitting	29
2.2.4 Best-fit Parameters Selection and Results	31
2.3 Relation between Flux and Spectral Index	33
2.4 Discussion	39
2.5 Conclusion	41
3 Comparison of Observation with Models	45
3.1 Introduction	46
3.2 Observations and Data Reduction	47
3.3 Acceleration Scenarios	48
3.3.1 The Constant Productivity Scenario	49
3.3.2 The Stochastic Acceleration Scenario	49
3.3.3 Relations with the Pivot-Point Model	51
3.4 Comparison with the Data	52

3.4.1	Fittings in δ - Φ_{ϵ_0} Plane	52
3.4.2	Comparing Model Parameters	53
3.5	Discussion	60
3.6	Conclusion	60
4	Stochastic Acceleration Modeling	63
4.1	Introduction	64
4.2	Pivot-Point Theory	66
4.2.1	Proof of the Equivalence between Pivot Point and Cor- relation of δ with $\log F$	67
4.2.2	Implications	68
4.3	The Model	69
4.3.1	The Transit-Time Damping Model	70
4.3.2	Transit-Time Damping and Escape	71
4.3.3	Method of Solution	75
4.3.4	From Electrons to Photons	75
4.4	Results	76
4.4.1	Results for the Default Values of the Model Parameters .	76
4.4.2	Exploration of the Parameter Space	79
4.4.3	Alternative Escape Modeling	83
4.5	Discussion	85
4.6	Conclusions	86
5	Evolution of Reconnection along an Arcade	89
5.1	Introduction	90
5.2	Observations	91
5.3	Conclusion	95
6	Summary and Outlook	99
A	Diffusion Equation in Energy Space	101
B	Approximate Analytical Solution	103
	Curriculum Vitæ	105
	List of Publications	107
	Acknowledgments	111
	Bibliography	113

Abstract

Solar flares and associated Coronal Mass Ejections (CMEs) are the biggest explosions in the solar system, converting huge amounts of magnetic energy into kinetic energy of accelerated particles and heat. The key questions at the core of flare physics research are: how is the energy stored in the solar corona before the flare? What triggers the sudden release of that energy? How are the particles accelerated and heated during the flare? Notwithstanding the strong theoretical and observational progress of the last few decades, these questions still remain open.

Hard X-ray observations of the Sun, such as provided by the Reuven Ramaty High-Energy Solar Spectroscopic Imager (RHESSI), are the best tools to probe the population of flare-accelerated particles, because X-rays are the direct signature of energetic electrons. In this thesis, novel RHESSI hard X-ray observations of solar flares are compared with quantitative predictions from modern theoretical models of stochastic acceleration of electrons. The focus lies on the spectral evolution, which has been discovered in the early days of hard X-ray observations, but, with a few exceptions, neglected by theorists.

The work presented here starts with RHESSI observations of the spectral evolution of the non-thermal component in the hard X-ray spectrum of solar flares. A representative sample of 24 M class impulsive flares is analyzed. They show rapid changes in the spectral hardness during distinct emission spikes. The maximum hardness is reached at peak time, thus the spectral behavior can be classified as soft-hard-soft. A quantitative relation between the normalization of the power-law component and its spectral index is found, holding for single emission spikes, as well as for the whole dataset comprising all events.

The analysis is then expanded, transforming the data from photon space to electron space and comparing the results with predictions from simple available electron acceleration models featuring soft-hard-soft behavior. This simple approach yields plausible best-fit model parameters for about 77% of the 141 events consisting of rise and decay phases of individual hard X-ray spikes. This success suggests that stochastic acceleration is a viable mechanism to explain the observed spectral evolution.

Therefore, a recent stochastic acceleration model, the transit-time damping acceleration scenario, was chosen for further investigation. A mechanism

that accounts for particle trapping in the accelerator was added in order to account for changes in the spectral hardness. The model predictions for the spectral evolution were compared with spectral observations of *looptop* hard X-ray sources, delivering a snapshot of the particles still residing in the accelerator. A novel parameter was used for the comparison, the *pivot point* (that is, a common crossing point of the accelerated particle spectra at different times). The model computations show the presence of a pivot point at an energy of 10 keV. This value can be brought in agreement with the observed value of 20 keV by enhanced trapping through an electric potential.

Lastly, some puzzling observations of the motion of hard X-ray sources during an impulsive M class flare are reported. The double sources, interpreted as footpoints of magnetic loops, show continuous motion along an arcade of magnetic loops, contradicting the predictions of the translation invariant 2.5D reconnection models, where motion perpendicular to the arcade is expected. Therefore, the development of more realistic 3D models is needed to account for such behavior.

Riassunto : osservazioni e modelli dell'evoluzione dinamica nei brillamenti solari

Le esplosioni più potenti del sistema solare sono i brillamenti solari e le espulsioni di massa coronale. Essi trasformano enormi quantità di energia magnetica in calore ed accelerano particelle fino a velocità relativistiche. La fisica dei brillamenti solari cerca di rispondere alle seguenti domande fondamentali: come viene immagazzinata l'energia nella corona prima di un brillamento? Qual è il meccanismo che innesca l'improvviso sprigionamento di tale energia? Come avviene l'accelerazione delle particelle e la liberazione del calore durante il brillamento? Nonostante i grandi progressi compiuti durante gli ultimi decenni nel campo della teoria e delle osservazioni, questi problemi rimangono tuttora irrisolti.

Il satellite RHESSI (Reuven Ramaty High-Energy Solar Spectroscopic Imager) osserva i raggi X provenienti dal sole e permette di studiare la popolazione di particelle accelerate dai brillamenti, visto che l'emissione nei raggi X può essere direttamente ricondotta agli elettroni energetici. In questa tesi, le nuove osservazioni di RHESSI sono comparate alle predizioni quantitative di moderni modelli teorici sull'accelerazione stocastica degli elettroni. Il paragone viene effettuato concentrandosi sull'evoluzione spettrale, un tema conosciuto fin dal principio delle osservazioni nei raggi X, ma, con poche eccezioni, trascurato dai teorici.

Si parte da osservazioni compiute da RHESSI sull'evoluzione spettrale della componente non termica nei brillamenti solari. L'analisi dei dati mostra rapidi cambiamenti della durezza spettrale durante i distinti picchi dell'emissione di 24 brillamenti di classe M. La massima durezza spettrale è raggiunta contemporaneamente al massimo del flusso, e quindi il comportamento spettrale comporta un andamento in cui lo spettro è dapprima soffice, poi duro e poi soffice ancora. Si osserva una relazione quantitativa tra l'indice spettrale e la normalizzazione della componente non termica. Questa legge è valida non solo per i singoli picchi di emissione, ma anche per l'insieme dei dati di tutti gli eventi.

L'analisi viene poi estesa ricostruendo la distribuzione degli elettroni ac-

celerati a partire dagli spettri osservati nei raggi X, e confrontando i risultati con le predizioni di semplici modelli sull'accelerazione degli elettroni, i cui parametri fisici possono essere stimati dai vincoli osservazionali. Nonostante i modelli considerati siano molto semplici, questo approccio produce risultati ragionevoli per i parametri fisici dei modelli in circa il 77% dei 141 eventi studiati (corrispondenti ognuno ad una fase di crescita o declino di un picco dell'emissione nei raggi X). Questi risultati suggeriscono che l'accelerazione stocastica possa essere un meccanismo atto a spiegare l'evoluzione spettrale osservata.

Quindi un modello più moderno di accelerazione stocastica, lo scenario del *transit-time damping*¹, è stato scelto per ulteriori investigazioni. Tramite l'aggiunta di un termine che descrive il meccanismo di fuga delle particelle dalla zona in cui avviene l'accelerazione, è possibile rendere conto dei cambiamenti osservati nello spettro. Le predizioni di questo modello sull'evoluzione spettrale sono state comparate con le osservazioni degli spettri di sorgenti di raggi X situate in cima agli archi del campo magnetico, dove avviene l'accelerazione. Per il confronto si utilizza un parametro detto *punto pivotale*, ovvero un punto di intersezione comune agli spettri osservati in tempi diversi. Il modello prevede la presenza di un punto pivotale ad energie intorno ai 10 keV. Modificando il modello riducendo il tasso di fuga delle particelle a basse energie, questo valore raggiunge il livello osservato di 20 keV.

Infine sono riportate alcune osservazioni sul moto delle sorgenti di raggi X durante un brillamento impulsivo di classe M. Le sorgenti doppie, osservate alla base degli archi magnetici, mostrano un movimento continuo lungo un sistema di archi coronali. Questo contraddice i modelli di riconnessione 2.5 dimensionali (invarianti rispetto alla traslazione nella terza dimensione), che prevedono moti perpendicolari al sistema di archi magnetici coronali.

¹letteralmente: “ammortizzazione nel tempo di transito”, un concetto di fisica del plasma che descrive un meccanismo per il trasferimento di energia da onde a particelle.

Chapter 1

Introduction

Flare: The action or quality of giving forth a dazzling and unsteady light

Oxford English Dictionary

The Sun supports life on Earth by steadily emitting $3.8 \cdot 10^{26}$ W of radiant energy, mainly concentrated in the range of visible light and near infrared. Aside from this steady radiation, transient events occur, lasting from a few minutes to several hours: *solar flares*. These are localized events of energy release whose power is just a tiny fraction of the total solar luminosity (of the order of 0.1% for large flares). Nevertheless, since they happen in a relatively small volume on the Sun, they have strong consequences for the solar atmosphere: plasma is heated to a temperature of tens of millions K and both electrons and ions are accelerated to ultrarelativistic energies. Thus the solar flare emission in UV, X-rays, gamma-rays and radio wavelengths strongly exceeds the quiet Sun.

Another manifestation of violent energy release on the Sun is the appearance of Coronal Mass Ejections (CMEs). During these, a cloud of matter from the corona is violently hurled into interplanetary space, at speeds of up to a few thousands km s^{-1} . Large flares are nearly always associated with CMEs, but the relation between them is not fully understood. A CME impacting on Earth can severely disrupt its magnetosphere, generating geomagnetic storms and accelerating particles causing the auroras. Electrons and ions accelerated near the Sun by flares or CMEs can escape into interplanetary space. These are registered on Earth as Solar Energetic Particles (SEP) events, which can have destructive effects on artificial satellites. The temporary modifications of

the environment around the Earth, collectively named *Space Weather*, have attracted considerable interest because of their damaging potential.

Flares, coronal mass ejections and energetic particle events are all different pieces of a big jigsaw puzzle. The ultimate goal of high energy solar physics is to fit them together into a coherent picture explaining the underlying physical processes. The *bottom-up* paradigm commonly used in the physical sciences states that the properties of each building block have to be well understood before a meaningful synthesis can be done. Consequently, this thesis is focused mostly on solar flares.

Solar flare research addresses the following fundamental key questions:

- (a) How is the energy stored in the solar corona before the flare?
- (b) What causes the stored energy to be suddenly released?
- (c) Where and how are the particles energized during the flare?

Briefly, these are the problems of, respectively, *energy storage*, *flare triggering* and *particle acceleration*. While many ideas and models exist, these questions have not yet been satisfactorily answered. One of the reasons for that is the relatively poor knowledge of the physical parameters of the flaring regions: for some quantities believed to play a critical role, like the magnetic field strength in the corona, no direct measurements exist. Furthermore, in observations of solar flares, sometimes it is hard to ascertain whether a given feature is directly related to the acceleration mechanism or is a secondary manifestation not connected with the main energy release.

The flare observations and models presented in this thesis are aimed to help solving question (c), the acceleration problem. Observations and model focused on that question are presented in Chapters 2, 3, 4, and 5, based on, respectively, Grigis & Benz (2004, 2005a, 2006 and 2005b).

This introduction continues with a short historical review of solar flare observations, an overview of the Ramaty High Energy Solar Spectrometric Imager (RHESSI), an explanation of the X-ray emission mechanism with examples of actual hard X-ray spectra and images from solar flares, which are interpreted in the context of a physical scenario. We then move on to a discussion of the importance of flares of different size for the coronal heating problem and present some results from RHESSI observations of microflares.

1.1 Short History of Flare Observations

The first confirmed observation of a solar flare have been described by Carrington (1859) and Hodgson (1859), who independently observed a brightening in a projected white-light image of the Sun. Carrington's drawing is shown on Fig. 1.1.

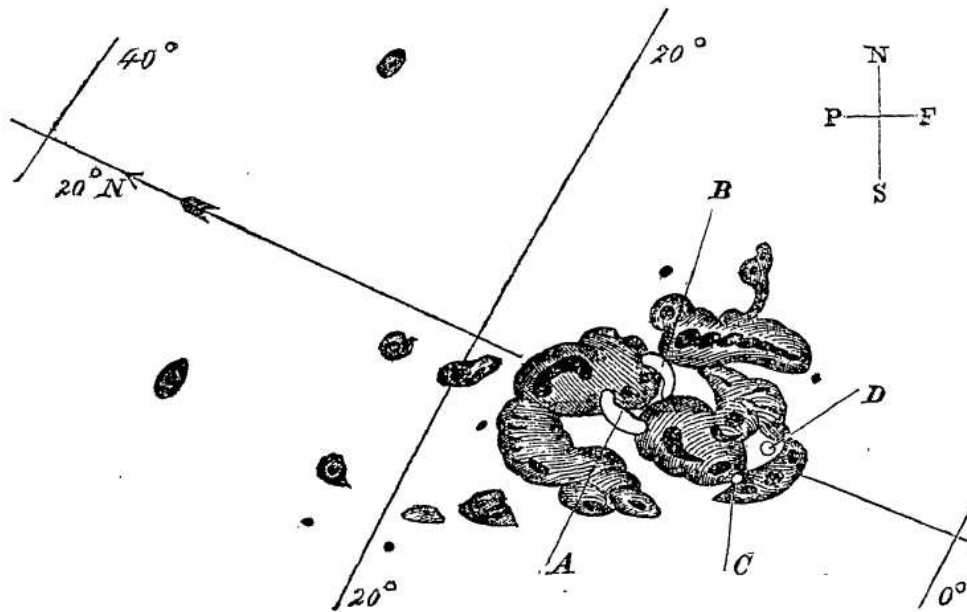


Figure 1.1: First drawing of a solar flare, seen in white light by Carrington (1859). At the beginning of the flare, the emission comes from the two ribbons A & B. A few minutes later, the emission has shifted to positions C & D. The motion is parallel to the direction of the ribbons (cfr. Chapter 5).

Bright white light flares with an enhancement of the continuum emission, such as the one observed by Carrington and Hodgson, are rare. On the other hand, brightenings of spectral lines are quite common. The invention of the spectroheliograph in 1892 by G. Hale (and, independently, by H. Deslandres) made possible to take pictures of the Sun in the light of a single spectral line instead of the continuum, and indeed brightenings were often seen in active regions. Traditionally flares are observed in the strong chromospheric hydrogen $H\alpha$ line, but they also show strong emission features in lines from other elements like calcium, helium, sodium, etc. Until the early 1940s, spectroheliographic observation were the only practical way to observe solar flares. Figure 1.2 shows the first published photograph of a solar flare taken with the Hale spectroheliograph.

The flare behavior seen in these early $H\alpha$ observations was puzzling enough to prompt Richardson (1937) to write that “it is difficult to generalize about bright chromospheric eruptions¹ because notable exceptions can be found to almost any statement made”, a sentence which still rings true in 2006.

The technological progress brought forth the discovery of radio emission from the Sun at meter wavelengths during World War II by Hey (1946). The

¹The term *flares* was not in common use before the late 1940s (Cliver 1995).

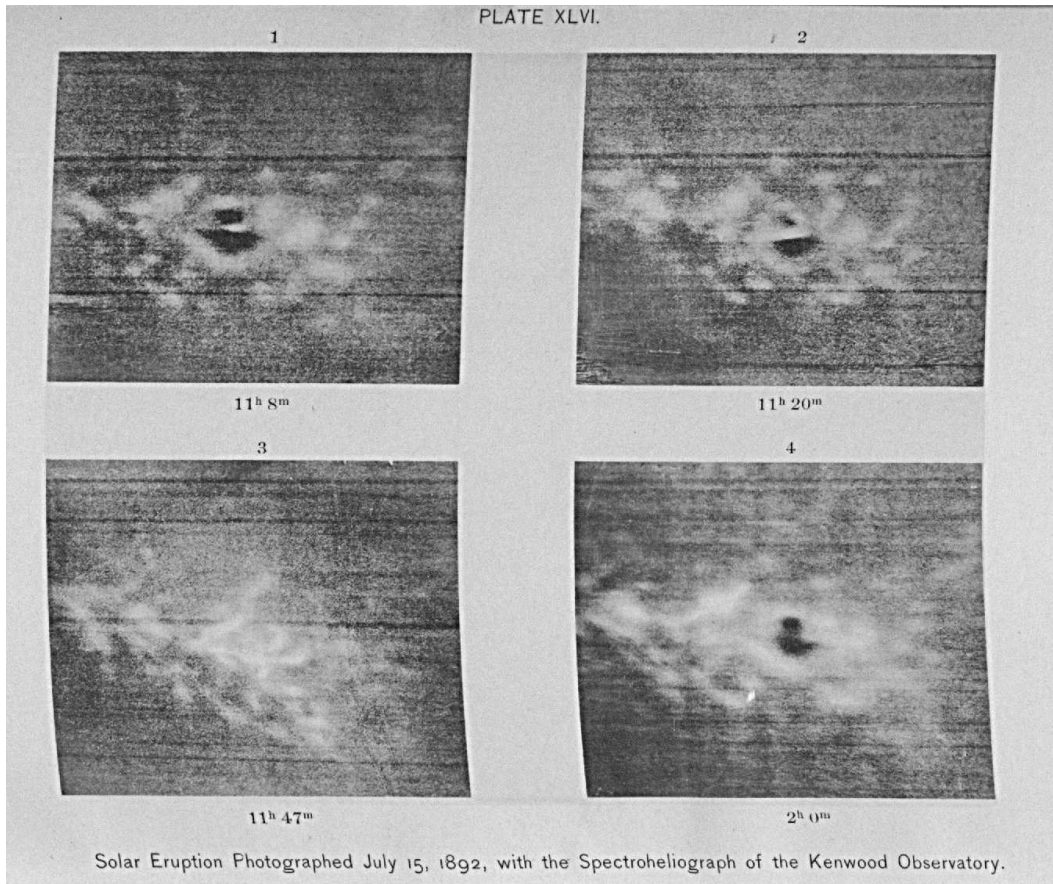


Figure 1.2: First photograph of a solar flare taken in a line of ionized calcium with the newly invented spectroheliograph (from Hale 1892).

rash technical development soon permitted the building of radiospectrographs (capable of sampling many different frequencies, thus yielding radio spectra) and radioheliographs (yielding images of the Sun). Most large flares have strong emission in the range of frequency easily observable from the Earth's surface (about from 10 MHz to 100 GHz).

Radio emission can be generated by both thermal and suprathermal electrons, so the very first radio observations could not establish how strongly particles are accelerated in solar flares. The first indication that particles are accelerated to relativistic energies in solar flares came from observation of GeV protons by ground stations (Forbush 1946). Later, balloons, sounding rockets and satellites opened the window of the high energy radiation from UV to gamma-rays, and high-energy solar physics could really start.

Hard X-rays are an especially valuable tool for observing the signature of fast particles, because they propagate straightforwardly from the Sun to

the Earth, and their relatively simple emission process yields reliable energy estimates. Furthermore, the background of thermal particles in the corona at 1-2 MK does not contribute appreciably to the X-ray emission above 10 keV.

Regular observation of the Sun in hard X-rays and γ -rays began with the Orbiting Solar Observatory (OSO) series, launched in the period 1962–1975, exploring the X-ray emission and discovering γ -ray line emission during solar flares. These successful observations led to the development of the Solar Maximum Mission (SMM), launched in 1980, which achieved crude imaging in the hard X-ray range. The Hinotori satellite, launched in 1981, also had hard X-ray imaging capabilities. Progress in hard X-ray imaging capabilities went on with the Yohkoh satellite, launched in 1991 and operating until 2001. To date, the best imaging and spectral data are delivered by the RHESSI satellite described in the next section.

1.2 The Ramaty High-Energy Solar Spectroscopic Imager (RHESSI)

The RHESSI satellite is a NASA small explorer mission (SMEX) designed to explore the basic physics of particle acceleration and explosive energy release in solar flares. It has been launched in February 2002 and has operated flawlessly since then, observing more than 20 thousand flares. It observes hard X-rays and gamma-rays in the range of 3 keV to 17 MeV, with an energy resolution of about 1 keV in the hard X-ray range and a few keV in the gamma-ray range.

RHESSI has 9 identical germanium detectors with a diameter of 7.1 cm each. In front of each detector there is a pair of grids which are used for imaging: the rotation of the satellite (about 15 RPM) produces a modulation of the signal of sources seen through the grids. It is then possible to reconstruct the images from the modulation patterns. Each grid pair has a different pitch, in order to sample different size scales. The nominal resolution of the finest grid is of 2.3". In practice, however, a large number of photons from the source is needed to achieve good imaging at that resolution, requiring long integration times in large energy bands.

RHESSI's energy range extends well into the range where thermal emission dominates, allowing a clean separation of the thermal from the non-thermal component. Thus it is well suited to study the evolution of the spectra in time. Spatially integrated spectroscopy can be easily achieved down to integration times of about 4 s (one spin period). To reach higher cadences the modulation introduced by the grids has to be removed, which is by no means a straightforward task (see for example Arzner 2002).

Large flares produce so many low-energy photons that they can completely saturate the germanium detectors of RHESSI, therefore attenuators are put in



Figure 1.3: RHESSI mission logo.

place: they are thin aluminum discs which are put in front of the detectors and absorb low-energy photons. When no large flares are expected, the attenuators are moved away from the detectors' field of view, in order to achieve maximum sensitivity for small flares.

A detailed description of the instrument, the detectors and the imaging system of RHESSI can be found in Lin et al. (2002), Smith et al. (2002) and Hurford et al. (2002a), respectively.

1.3 Hard X-ray Emission and Flare Spectra

Hard X-ray emission during solar flares is generated mainly by electrons, because they have a much larger charge-to-mass ratio than the ions. Thus they are subjected to stronger acceleration, which leads to emission of radiation. The main mechanisms acting are:

- *Free-free radiation*: this describes the bremsstrahlung emission from an electron deflected by another charged particle, but not captured during the process. The emission is more efficient if the collision happens with

a heavy particle, such as a proton or a heavier atomic nucleus. This mechanism produces a continuum emission.

- *Free-bound radiation*: this is the emission from an electron captured by an ion (recombination). The capture probability depends on the charge of the ion and is larger for heavier elements, like iron, and relatively slow electrons. Therefore the strength of free-bound radiation is more sensitive to, say, iron abundance, than free-free radiation is. This process also produces a continuum with additional sharp steps corresponding to the atomic energy levels of the final bound state of the electron.
- *Bound-bound radiation*: this is the emission of excited electrons in an ion falling into a lower energetic state. This mechanism produces lines. In the astrophysical context, where the abundance of elements heavier than nickel can be neglected, the maximum energy of the line emission lies around 8 keV.

Other processes (for instance involving 3 particles) are possible but do not contribute strongly to the total emission above a few keV and will not be discussed here.

Energetic electrons in a plasma can be classified as being *thermal* if they obey a Maxwell-Boltzmann distribution and *nonthermal* otherwise. In a plasma, faster particles have a smaller chance to undergo collisions than slower particles: the collision time increases with energy. In the solar corona the collision times for energetic electrons (above, say, 20 or 30 keV, depending on density) are so large that they are not immediately thermalized, thus enabling the observation of nonthermal particle distributions. If these fast particles impact onto a region of higher density (such as the lower part of the solar atmosphere), their collision rate increases strongly and they will emit X-rays.

1.3.1 Bremsstrahlung Emission

To be able to compute the free-free emission of a fast electron coming into a cold target (that is, a target whose particles are much slower than the impinging electron) a *cross section* for the emission of radiation must be used. The bremsstrahlung cross section gives the probability for the emission of a photon of a given energy and momentum as a function of the energy and momentum of the incoming and scattered electron. The cross section can be calculated by solving the Dirac equation for an electron in the Coulomb field of the nucleus. The use of the Born approximation delivers a closed analytical expression, first computed by Bethe & Heitler (1934). The cross section depends on the direction of propagation of the emitted photon, such that a beam of collimated electrons would have a strongly anisotropic radiation pattern. However, if the emitting electrons are isotropically distributed, the radiation pattern will

also be isotropic and can be obtained by integrating the cross section over all possible angles. A useful list of cross sections computed under different approximations is given by Koch & Motz (1959).

The energy differential bremsstrahlung cross section, integrated over all possible directions for both the emitted photon and the outgoing electron, is given by $d\sigma(\varepsilon, E)/d\varepsilon$, a function of the photon energy ε and the incoming electron kinetic energy E , where both energies are given in units of mc^2 , with m representing the electron mass.

Using the following notations for the incoming and outgoing total energies and momenta of the electron

$$\begin{aligned} E_{\text{in}} &= 1 + E & E_{\text{out}} &= E_{\text{in}} - \varepsilon \\ p_{\text{in}} &= \sqrt{E_{\text{in}}^2 - 1} & p_{\text{out}} &= \sqrt{E_{\text{out}}^2 - 1} \end{aligned}$$

we can express the cross section as:

$$\frac{d\sigma(\varepsilon, E)}{d\varepsilon} = Z^2 r_0^2 \alpha \frac{p_{\text{out}}}{\varepsilon p_{\text{in}}} Q, \quad (1.1)$$

where Z is the charge of the nucleus, $r_0 = e^2/mc^2$ is the classical electron radius, α is the fine structure constant and Q is given by

$$\begin{aligned} L_{\text{in}} &= \ln \frac{E_{\text{in}} + p_{\text{in}}}{E_{\text{in}} - p_{\text{in}}} & L_{\text{out}} &= \ln \frac{E_{\text{out}} + p_{\text{out}}}{E_{\text{out}} - p_{\text{out}}} \\ L &= 2 \ln \frac{E_{\text{in}} E_{\text{out}} + p_{\text{in}} p_{\text{out}} - 1}{\varepsilon} \\ F_1 &= \frac{L_{\text{in}}}{p_{\text{in}}^3} (E_{\text{in}} E_{\text{out}} + p_{\text{in}}^2) - \frac{L_{\text{out}}}{p_{\text{out}}^3} (E_{\text{in}} E_{\text{out}} + p_{\text{out}}^2) + 2\varepsilon \frac{E_{\text{in}} E_{\text{out}}}{p_{\text{in}}^2 p_{\text{out}}^2} \\ F_2 &= \frac{8}{3} \frac{E_{\text{in}} E_{\text{out}}}{p_{\text{in}} p_{\text{out}}} + \varepsilon^2 \frac{E_{\text{in}}^2 E_{\text{out}}^2 + p_{\text{in}}^2 p_{\text{out}}^2}{p_{\text{in}}^3 p_{\text{out}}^3} + \frac{\varepsilon}{2} \frac{F_1}{p_{\text{in}} p_{\text{out}}} \\ Q &= \frac{4}{3} - 2E_{\text{in}} E_{\text{out}} \frac{p_{\text{in}}^2 + p_{\text{out}}^2}{p_{\text{in}}^2 p_{\text{out}}^2} + E_{\text{out}} \frac{L_{\text{in}}}{p_{\text{in}}^3} + E_{\text{in}} \frac{L_{\text{out}}}{p_{\text{out}}^3} - \frac{L_{\text{in}} L_{\text{out}}}{p_{\text{in}} p_{\text{out}}} + L F_2. \end{aligned}$$

This Born approximation is relativistically correct but the formula fails when the scattered electron has low energy. Elwert (1939) proposed a multiplicative correction factor to improve the cross section in that limit. The cross section with the Elwert correction factor has been shown to better reproduce the results of numeric solutions of the Dirac Equation for scattering off low Z nuclei than the uncorrected cross section (Pratt & Tseng 1975).

The Elwert factor is

$$f_{\text{E}} = \frac{E_{\text{out}}}{E_{\text{in}}} \frac{p_{\text{in}}}{p_{\text{out}}} \frac{1 - \exp(-2\pi\alpha Z E_{\text{in}}/p_{\text{in}})}{1 - \exp(-2\pi\alpha Z E_{\text{out}}/p_{\text{out}})}$$

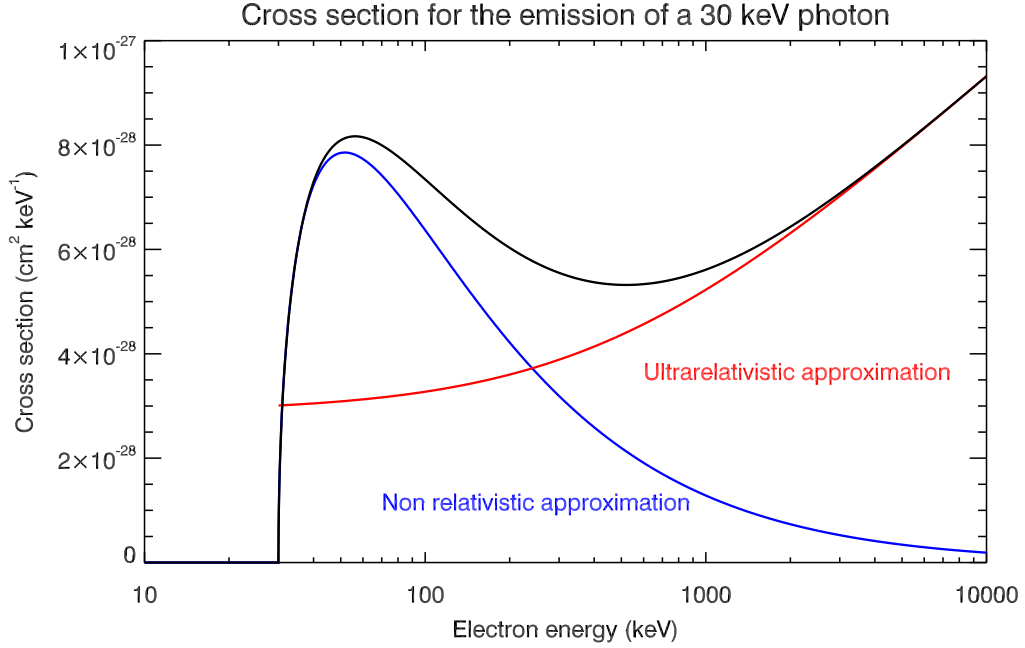


Figure 1.4: Cross section for the emission of a 30 keV photon (Born approximation without Elwert factors, for atomic charge $Z = 1$). *Black*: Bethe-Heitler formula, Eq. (1.1). *Blue*: nonrelativistic approximation, Eq. (1.2). *Red*: ultrarelativistic approximation, Eq. (1.3).

We note that it is necessary to use the relativistically correct formula also at relatively low photon energy (say, 50 keV) because there is a non-negligible chance that a photon of that energy is emitted by an electron with an energy several times higher, where the use of a nonrelativistic formula is no longer permitted.

The much simpler nonrelativistic approximation ($\varepsilon < E \ll 1$) of Eq. (1.1) is

$$\frac{d\sigma}{d\varepsilon} = \frac{16}{3} Z^2 r_0^2 \alpha \frac{1}{\varepsilon p_{\text{in}}^2} \ln \frac{p_{\text{in}} + p_{\text{out}}}{p_{\text{in}} - p_{\text{out}}} \simeq \frac{8}{3} Z^2 r_0^2 \alpha \frac{1}{\varepsilon E} \ln \frac{1 + \sqrt{1 - \varepsilon/E}}{1 - \sqrt{1 - \varepsilon/E}}, \quad (1.2)$$

often used for analytical work (e.g. Brown 1971). There also is a simple ultrarelativistic approximation $E \gg 1$:

$$\frac{d\sigma}{d\varepsilon} = 4Z^2 r_0^2 \alpha \frac{1}{\varepsilon} \left[1 + \left(\frac{E_{\text{out}}}{E_{\text{in}}} \right)^2 - \frac{2}{3} \frac{E_{\text{out}}}{E_{\text{in}}} \right] \left[\ln \frac{2E_{\text{in}}E_{\text{out}}}{\varepsilon} - \frac{1}{2} \right]. \quad (1.3)$$

The difference between the above approximations and the complete formula is shown in Fig. 1.4, where the cross section for the emission of a 30 keV

photon is shown as a function of the energy of the incoming electron. The nonrelativistic approximation becomes quite bad above 100 keV.

The emission from an isotropic electron population in a target can be computed using Eq. (1.1). However, the electrons undergo different processes leading to energy losses, which modify the electron distribution and thus the photon spectrum. For simplicity, we discuss here two extreme cases for stationary emission: the *thin-target* and the *thick-target* cases. The former simply refers to the situation where the electrons have the same energy distribution everywhere in the target. This can be realized in practice by injecting an homogenous beam into a spatially thin target, where the chance of any electron interacting with the target is low enough that the injected distribution is not changed appreciably in the target. Another possibility is the emission from a homogeneous population of electrons in equilibrium with the ambient plasma: this also guarantees that the distribution does not change with time or location. The latter case considers the situation where an *initial* distribution is injected into a target and it loses all its energy in the target until it is thermalized. The emitted photon spectrum depends on the details of the energy loss processes in the target.

Thin-Target Emission

We first consider an uniform electron beam with area S of N monoenergetic electrons $\text{cm}^{-2} \text{s}^{-1}$ propagating with kinetic energy E into a thin target with uniform ion density n_{TAR} and thickness L . It will emit photons with a rate of

$$\underbrace{J(\varepsilon) d\varepsilon}_{\text{Number of photons emitted per second}} = \underbrace{SN}_{\text{Number of electrons hitting the target per second}} \cdot \underbrace{n_{\text{TAR}} d\sigma(\varepsilon, E)L}_{\text{Number of target particles colliding with one electron and producing a photon with energy } \varepsilon}$$

This can be immediately generalized by going from the electron flux N to the energy differential electron distribution function $F(E)$, given in electrons $\text{cm}^{-2} \text{s}^{-1} (mc^2)^{-1}$, producing a total photon spectrum $I(\varepsilon)$ in photons $\text{s}^{-1} (mc^2)^{-1}$

$$I(\varepsilon) d\varepsilon = n_{\text{TAR}} L S \int_{\varepsilon}^{\infty} F(E) d\sigma(\varepsilon, E) dE \quad (1.4)$$

Then the photon flux at Earth $J(\varepsilon)$ in photons $\text{cm}^{-2} \text{s}^{-1} (mc^2)^{-1}$ is

$$J(\varepsilon) = \frac{I(\varepsilon)}{4\pi R^2} \quad (1.5)$$

where R is the distance from the source (about 1 AU for the Sun).

Thick-Target Emission

In the thick-target scenario, an electron distribution $F_{\text{INJ}}(E)$ is injected into the target. The most effective collisions leading to energy loss for the injected electrons are electron-electron collision. The assumption that only this collisions are acting leads to an expression for the photon spectrum $J(\varepsilon)$ in this scenario:

$$J(\varepsilon) = \frac{S}{4\pi R^2} \int_{\varepsilon}^{\infty} \frac{d\sigma_{\text{BREMS}}(\varepsilon, y)}{y d\sigma_{\text{ELOSS}}(y)} \int_y^{\infty} F_{\text{INJ}}(x) dx dy \quad (1.6)$$

where $d\sigma_{\text{BREMS}}$ is the cross section for Bremsstrahlung producing collisions and $d\sigma_{\text{ELOSS}}$ is the cross section for collisions leading up to energy losses. For the nonrelativistic case, the energy losses are given by

$$d\sigma_{\text{ELOSS}}(E) = \frac{2\pi e^4 \ln \Lambda (mc^2)^2}{E^2} \quad (1.7)$$

where $\ln \Lambda$ is the Coulomb logarithm.

We note here that while collisions with nuclei can produce bremsstrahlung X-rays, collisions with other electrons are much more efficient at slowing down the fast electrons, and therefore only a small part (about 10^{-5}) of their energy is radiated away: most of the energy is transferred to the ambient plasma which is heated. The radiated energy from, say, an electron beam, is therefore a small fraction of its total energy content.

1.3.2 Observed X-ray Spectra

The hard X-ray spectrum observed during a typical solar flare is shown in Fig. 1.6, where the black line represent the observed flare photons, and the black crosses the pre-flare background. The models fitted are shown by colored lines. Fig. 1.5 shows the model spectra only.

The components shown in Fig. 1.5 are:

- *Thermal*: the purple line is the emission from a hot isothermal plasma, composed of the continuum and the atomic lines. It is characterized by its temperature T and its emission measure $\mathcal{M} = \int n^2 dV$, where n is the electron density in the plasma. The black curve is the same spectrum seen with a resolution of 1 keV, representing what RHESSI should be able to see.
- *Nonthermal*: the red line represents a broken power-law function:

$$F(E) = \begin{cases} F_0 \left(\frac{E}{E_0}\right)^{-\gamma_1} & \text{if } E \leq E_B \\ F_0 \left(\frac{E_B}{E_0}\right)^{-\gamma_1} \cdot \left(\frac{E}{E_B}\right)^{-\gamma_2} & \text{if } E > E_B \end{cases} \quad (1.8)$$

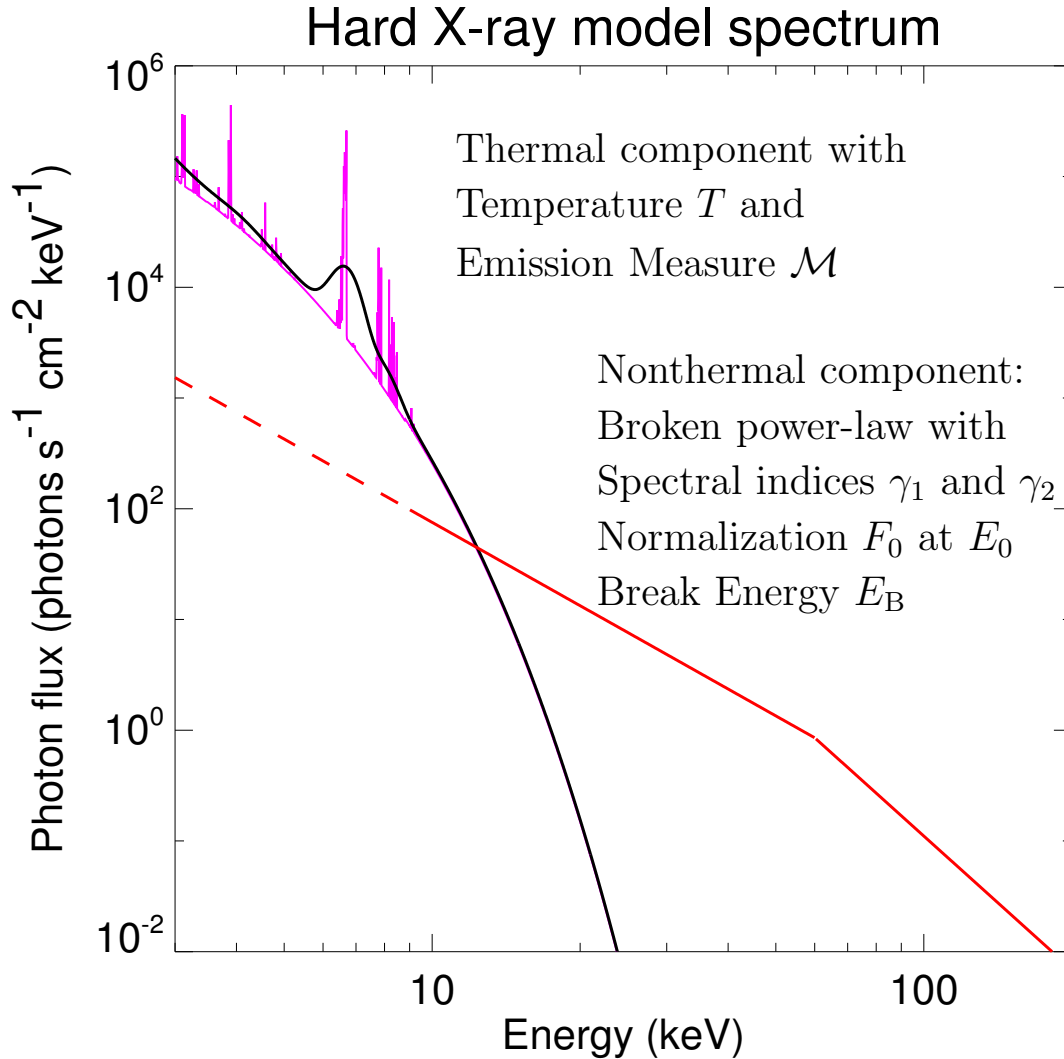


Figure 1.5: Model flare spectrum, showing the different components. The thermal continuum with atomic emission line is shown in purple. The black line is the same curve seen with a Gaussian FWHM resolution of 1 keV (representing what RHESSI should be able to see). The red line is a broken power-law component.

Here γ_1 and γ_2 are the spectral indices below and above the break, respectively. The power-law normalization at energy E_0 is given by $F_0 = F(E_0)$.

In Fig. 1.6 the residuals from the fitting are shown. It can be seen that the model fits well the overall trend observed, but there are systematic deviations around it. The (broken) power-law model is not so good: the spectrum is more complicated. While the double power-law model is often assumed, it is not a proven best-fit curve. Smoother, slightly downward bending curves (like the

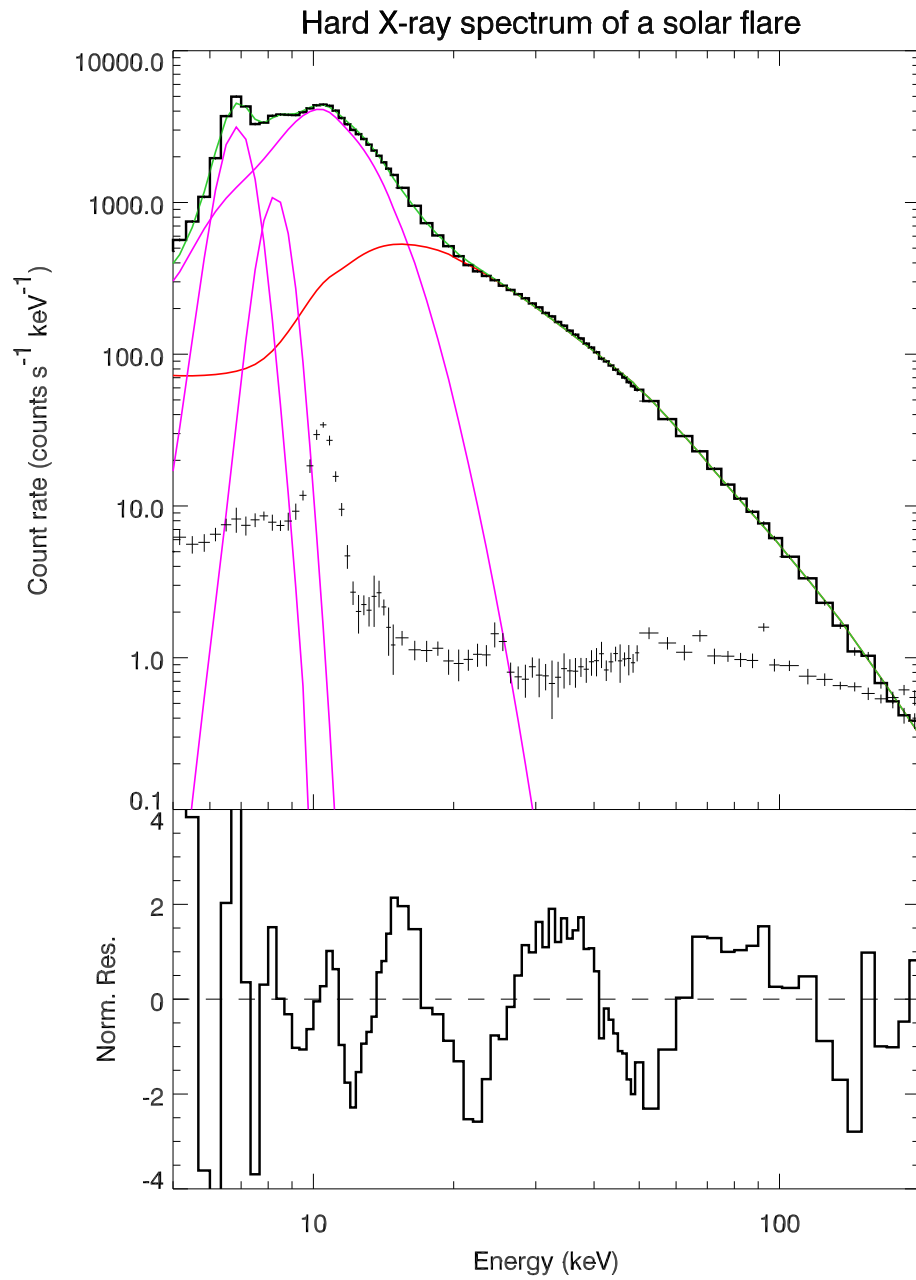


Figure 1.6: Hard X-ray spectrum of a solar flare (see text for a discussion of the meaning of the different components fitted). The lower panel shows the normalized residuals of the best-fit model. This spectrum is in count space, therefore the model components have been folded with the instrumental response function. See Fig. 1.5 for a representation of the components in photon space.

ones computed from theoretical acceleration models in Chapter 4) also fit the data. However, at this level of accuracy, instrumental effects gets important, and the behavior might also be due to some extent to calibration errors.

1.4 Hard X-ray Images and Flare Scenarios

The source of the energy released by a solar flare is the magnetic field, mainly because other types of energy storage (potential, thermal etc.) are just too weak to produce a large flare. The detailed mechanism responsible for the conversion of the magnetic energy is believed to be an event of *reconnection*. This is a process by which two separate regions of plasma, carrying magnetic flux pointing in opposite directions, are brought in contact with each other. During this process the magnetic field annihilates, releasing its energy. In the region where the two differently magnetized plasmas flow into each other, a current sheet is formed, since there the curl of the magnetic field becomes large. The energy thus released is converted into plasma waves, shock fronts and direct acceleration of particles in the current sheet. Since the current sheet, a two-dimensional interface between oppositely magnetized plasmas, is thin, not many particle can be directly accelerated there, and therefore additional acceleration has to occur elsewhere.

The idea behind *stochastic acceleration models* is that the waves created by the reconnection event are turbulent, and therefore their energy is quickly transferred into short-wavelength modes. The charged particles, gyrating in the magnetic field, can then resonantly exchange energy with the waves. By any interaction of a particle with a wave-train, energy can either go from the waves to the particles or *vice versa*. It is however possible to have a net average energy gain for the particles if the interactions leading to energy gains are more frequent than the ones leading to energy losses. Thus the particles describe a (possibly asymmetric) *random-walk* in energy space, which corresponds to a diffusion process. In stochastic acceleration models, the diffusion equation is solved to study the evolution of the accelerated particles.

The accelerated electrons that leave the acceleration region can travel down the loop all the way into the denser chromosphere, where they lose their energy, heating the plasma and radiating X-rays, showing up as footpoint sources in X-ray images. Fig. 1.7 shows an X-ray image of a solar flare, taken with RHESSI and integrated over a broad energy range. One source, called the *looptop* source, lies above the Sun's limb. Its spectrum is softer and it dominates at lower energies. Two further sources, called *footpoint* sources, are seen on the Sun's disk. They are harder and dominate at high energy. The different components of the scenario presented above are indicated. The primary energy release site, where the reconnection process presumably happens, is not visible.

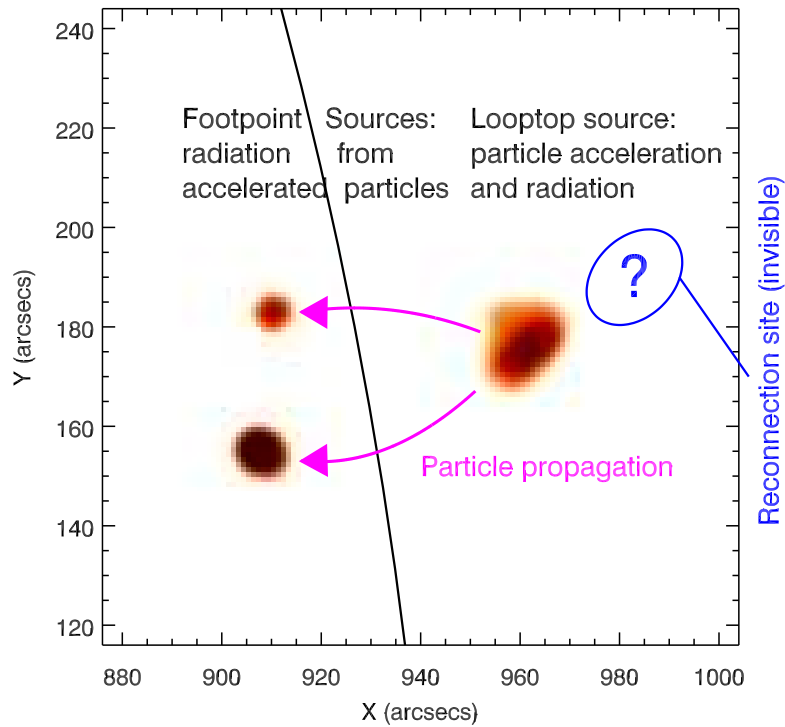


Figure 1.7: RHESSI hard X-ray image taken during a solar flare (image data courtesy of M. Battaglia). Physical interpretation (see text for more details): energy is released by a reconnection event in an invisible low-density region and transported (by waves or shock fronts) into a higher density region where particles are accelerated. Fast particle can escape from the acceleration region and travel down the loop legs to the footpoint sources, where the density is so large that the energetic particles are immediately stopped, strongly emitting X-rays in the process.

1.5 Coronal Heating and Flares

One of the biggest unsolved enigmas in solar physics is the coronal heating problem: why is the corona so hot? Its temperature lies between 1 and 2 MK above the quiet Sun, but it reaches 6 MK and more in active regions. This is much hotter than the photosphere and the chromosphere, and without additional energy input the corona would cool off quickly (timescale of hours to days). Different heating mechanisms have been proposed (for a review,

see chapter 9 in Aschwanden 2005). The main idea beyond most models is dissipation of energy residing either in waves or in currents, but they differ in the details of how and where the waves or currents are created and dissipated. Flares belong to the latter category, seen as explosive energy dissipation events. A related problem is the supply of matter into the corona, continually depleted by solar-wind losses (e.g. Brown et al. 2000). A mechanism of steady or explosive evaporation is needed to deliver mass from the lower solar atmosphere into the corona.

An important distinction needs to be made between heating of the active-region corona, the quiet-Sun corona and coronal holes. Active regions are usually dominated by the presence of closed magnetic field lines, such that hot material cannot escape easily into interplanetary space during non-flaring times. This explains why active regions are usually hotter and denser than the rest of the corona. Thermal conductivity across field lines is low, such that heat exchange between the active regions and their surroundings is not very strong, and the corona can stay inhomogeneous in temperature. Therefore, the quiet-Sun corona needs a heating mechanism independent from active regions (this is confirmed by the fact that the corona is not substantially cooled or depleted when no active regions are present on the disk).

Directly relevant to this thesis is the idea that energy release from flare-like phenomena is responsible for the heating. Parker (1988) proposed that the corona is heated by the collective effect of a large number of *nanoflares*, that is, small impulsive energy release events. Observational confirmation of this idea is hard, because the energy input of one event is tiny. Therefore, these events can be below the detection threshold of all instruments used to observe them, and one needs to observe larger events and extrapolate down to smaller sizes, with all the risks that such an operation entails.

Are small events relevant to coronal heating? The size of their contribution depends on the number of small events relative to large ones: if the frequency distribution is steep enough, the energy input is dominated by small events, whereas a shallow distribution shifts the importance toward large events (Hudson 1991). The observations show that the frequency distribution is usually given as a power-law function of the released energy with negative index: small events are much more frequent than large events.

The argument goes as follows: suppose that the number of flares releasing an energy between E and $E + dE$ is $n(E)dE$, and that the distribution is given by a power law with index α

$$n(E) = K \cdot E^{-\alpha}, \quad (1.9)$$

with positive constants K and α . The total energy E_{TOT} released can then be easily computed integrating the distribution between its low and high energy

thresholds E_{\min} to E_{\max} :

$$E_{\text{TOT}} = \int_{E_{\min}}^{E_{\max}} E \cdot n(E) dE = \int_{E_{\min}}^{E_{\max}} K E^{1-\alpha} dE$$

$$= \begin{cases} \frac{K}{2-\alpha} (E_{\max}^{2-\alpha} - E_{\min}^{2-\alpha}) \simeq \frac{K}{2-\alpha} E_{\max}^{2-\alpha} & \text{if } \alpha < 2 \\ K \ln \frac{E_{\max}}{E_{\min}} & \text{if } \alpha = 2 \\ \frac{K}{\alpha-2} \left(\frac{1}{E_{\min}^{\alpha-2}} - \frac{1}{E_{\max}^{\alpha-2}} \right) \simeq \frac{K}{\alpha-2} \frac{1}{E_{\min}^{\alpha-2}} & \text{if } \alpha > 2 \end{cases}$$

where the approximations hold if

$$\ln \frac{E_{\max}}{E_{\min}} \gg \frac{1}{|2-\alpha|}. \quad (1.10)$$

We see that if $\alpha < 2$, the total energy depends approximatively on E_{\max} only, and therefore the largest events dominate the energy release. On the other hand, if $\alpha > 2$ the smallest events dominate the total amount of energy released. If α is nearly 2, both small and large events contribute similarly. Observationally, there are large uncertainties in the computation of the total energy released from each event. The power-laws empirically found in frequency distributions lies in the range from 1.4 to 2.6. Many uncertainties related to selection effects can produce biases in the determination of such power-law indices. The largest events are easily observable, but the small events may be too weak to be successfully observed. It should be noted that even very sensitive instruments may miss small events, since they may add up together to produce the observed signal, which cannot easily be decomposed in the tracks from individual events.

In any case, current estimates of the energy input in the corona by observed flares suggest that it is too low by a factor of about 3. Therefore a better characterization of small events is useful in trying to understand how far this power-law frequency distribution goes and to compute the total energy input in the corona by flare-like events.

Normal flares are not observed outside active regions, so they cannot be used to explain heating of the quiet-Sun corona. Small energy release events outside active regions were discovered in soft X-rays (Krucker et al. 1997) and EUV observations (Krucker & Benz 1998) above the magnetic network. These *nanoflares* show characteristics roughly similar to regular flares, but for the smaller amount of released energy and different location. Their small size renders detailed observations very hard, so it is not yet clear if their energy release mechanism is different from regular flares.

Table 1.1: *Left*: List of time intervals where GOES satellites featuring soft X-ray detectors were active. GOES 10 and 12 are still operational at the time of writing. *Right*: GOES flare size classification.

Name	Operational		GOES Class	Total flux in 1-8 Å band
	from	to		
GOES 6	04 JAN 1980	18 AUG 1994	A1	10^{-8} Wm^{-2}
GOES 7	01 JAN 1994	03 AUG 1996	B1	10^{-7} Wm^{-2}
GOES 8	21 MAR 1996	18 JUN 2003	C1	10^{-6} Wm^{-2}
GOES 9	20 MAR 1996	24 JUL 1998	M1	10^{-5} Wm^{-2}
GOES 10	10 JUL 1998	—	X1	10^{-4} Wm^{-2}
GOES 12	13 DEC 2002	—		

1.5.1 Different Sizes of Solar Flares

Since the end of the 1980s (see Table 1.1), the GOES satellite family has provided continuous monitoring of the Sun in two soft X-ray bands ranging approximately from 1 to 8 Å (soft channel) and from 0.5 to 4 Å (hard channel). This has prompted a classification of flare size based on the power irradiated in the soft band that gradually replaced the former classification based on the area and luminosity of the brightening in $H\alpha$ images. The events are classified as belonging to class A, B, C, M, X if their peak emission increases over 10^{-8} , 10^{-7} , 10^{-6} , 10^{-5} , 10^{-4} Wm^{-2} , respectively (see Table 1.1). For more precise subdivision, a number after the class letter is intended as a multiplicative factor.

An example of flares of different sizes, from A to X, is shown in Fig. 1.8. The peak emission of the smallest flare is more than 4 orders of magnitude weaker than the largest. This large range of variation in the strength of the emission at short wavelengths means that sensitive instruments for flare observations can be easily saturated during large flares, whereas less sensitive instruments will not be able to observe small events.

RHESSI copes with this problem by using *attenuators* (or shutters). These are thin aluminum disks which can be put in front of the detectors. If no attenuators are put in front of the detectors, RHESSI has excellent sensitivity to small events down to 3 keV. If a larger flare happens, the attenuators are moved in, strongly absorbing the emission below 10-20 keV.

Figure 1.9 shows RHESSI observations without attenuators. Four different orbits are shown with decreasing solar activity level. In panel (a) the GOES

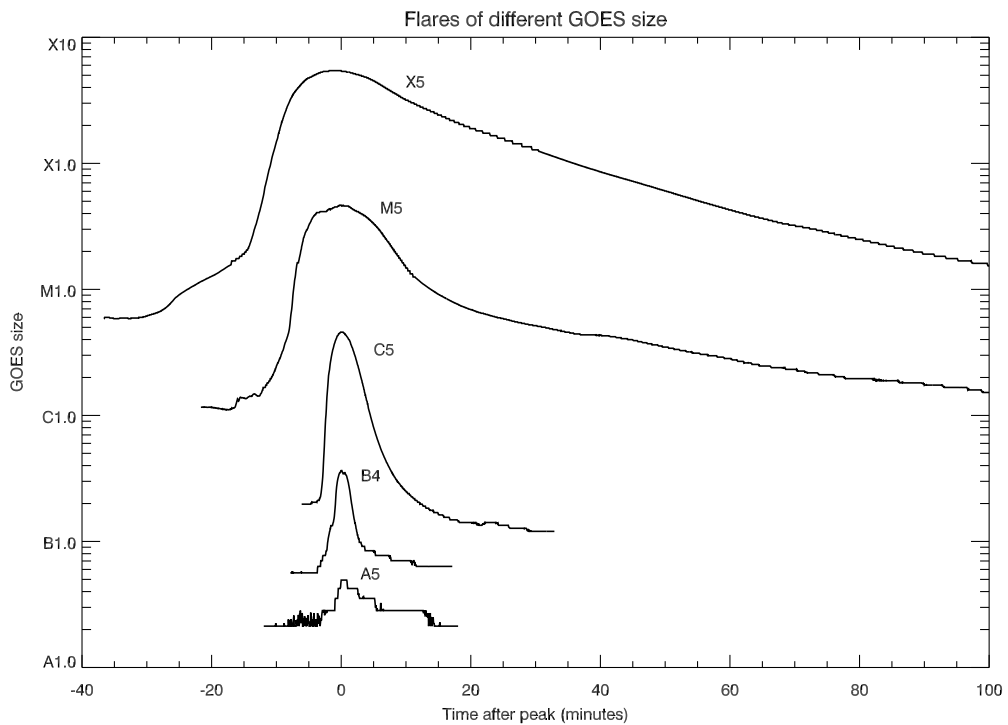


Figure 1.8: Five flares of different GOES size are shown. The time scale has been shifted such that the peak of each event is at time zero. The steps seen in the lightcurve are instrumental artifacts. Note the difference of more than 4 orders of magnitude between the weakest and the strongest event. The pre-event background is enhanced for large flares: this is due to the fact that active regions complex enough to produce large flares usually contain more hot plasma than simpler active regions producing small flares.

level is around B6 with a C1 flare (International Sunspot Number [ISN] 76), in panel (b) the GOES level is between B3 and B4 with several flares (ISN 57), in panel (c) the GOES level is around A5 with an A7 flare (ISN 22) and finally panel (d) shows a time interval with constant GOES flux around A1 without flares (ISN 0).

The spectrograms show the count rates in color scale from black (low rate) to blue, red, yellow, and white (high rate) as a function of time and energy. The instrumental background is due to cosmic rays and charged particles hitting the detectors. It can be seen in panel (d), where nearly all counts come from the background. Its sinusoidal modulation comes from the orbital motion of the satellite: near the equator the background reaches the minimum level and then slowly increases as the satellite moves to higher geomagnetic latitudes. In the spectrogram, horizontal background lines can also be seen. These are produced in the detectors and in the spacecraft. The strong feature around

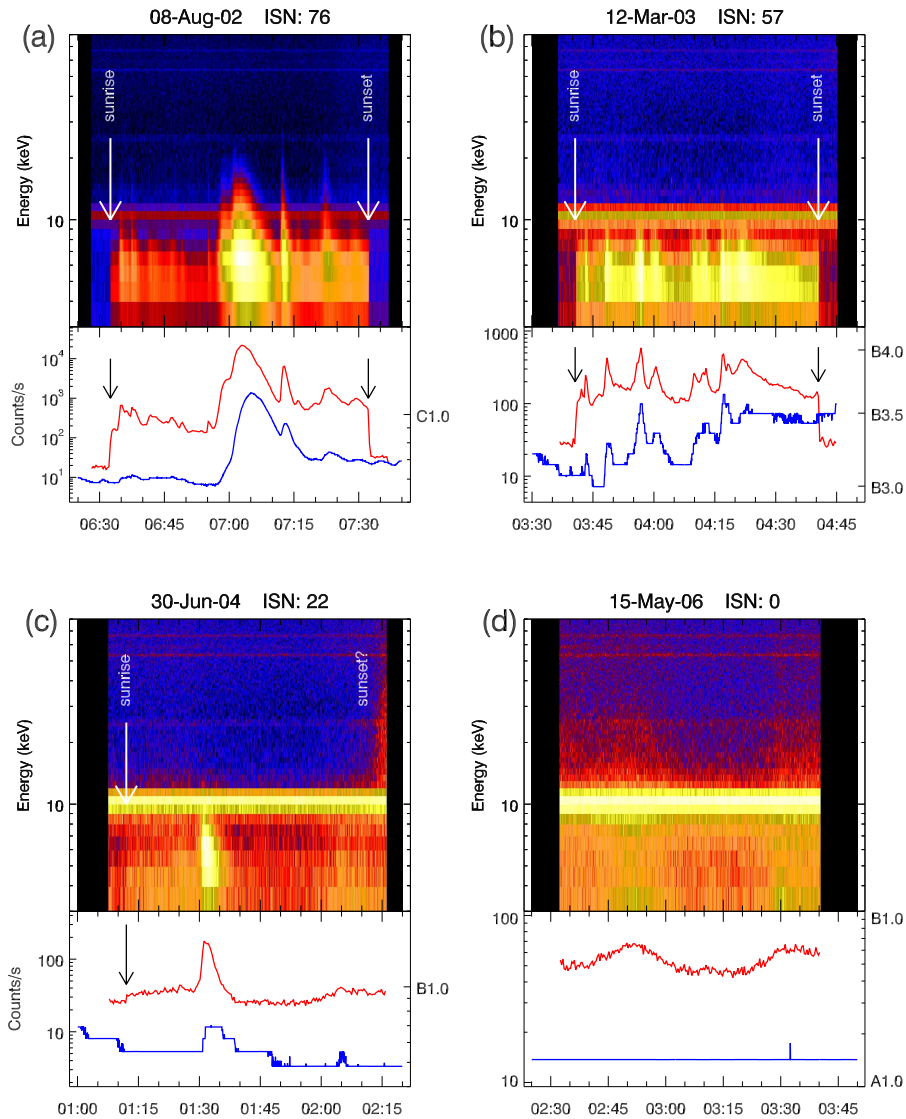


Figure 1.9: RHESSI spectrograms over RHESSI (red, top) and GOES (blue, bottom) lightcurves for 4 events with decreasing solar activity levels. The RHESSI lightcurves are the total counts per second in the 4-9 keV energy band. The background has not been subtracted, allowing a comparison with the strength of the solar signal. Note the sharp increases and decreases in flux due to sunrise and sunset on the spacecraft (indicated by the arrows). When activity drops to the lower parts of GOES class A, the solar signal is lost in the background, such that sunrise and sunset are no longer seen. The value of the International Sunspot Number (ISN; Van der Linden et al. 2006) is given on top of each plot.

11 keV is due to electrons knocked off from the K-shell of the germanium atoms in the detectors. Here it is clear that the main limitation of an instrument such as RHESSI in exploring weak events is given by the level of the background flux more than by the sensitivity of the detectors.

Active regions are hotter than the quiet-Sun corona. Therefore, it comes to no surprise that near solar maximum RHESSI always sees a solar emission in its lower energy channels when observing in shutterless mode. When the solar emission drops below GOES level of about A5 (depending on the background strength), RHESSI loses the solar signal in the background (see panel (c) and (d) of Fig. 1.9). This invalidates the interpretation that the continuum emission is a result of the decay of exotic particles like axions: analysis such as the one of Zioutas et al. (2004) are flawed by the use of RHESSI data from 2002, a period too close to solar maximum, when the emission originates from active regions. Now that we are near solar minimum, the estimate of coupling constants limits should be revised by using more recent RHESSI data with a careful treatment of the background.

1.6 RHESSI Observation of Microflares

RHESSI is ideally suited to observe weak events when its attenuators are moved away from the detectors². In the first three full months³ of operation (March, April, May 2002) there were about 50 orbits with RHESSI observing without the attenuators. From these orbits, the ones with uninterrupted observations of the Sun (lasting about 50 minutes each), low solar activity and low background were selected for further analysis. The condition required were:

- *Low activity*: a maximum count rate less than 600 counts s⁻¹ per detector in the 3–12 keV range.
- *Low background*: a nearly constant background in the 100-300 keV range (ensuring that no particle event contaminates the data).

Seven orbital intervals fulfilled these requirements, all of them with GOES level below C. The lightcurves of 4 of these orbits are shown in Fig. 1.10 for different energies (1 keV bins from 3 to 15 keV).

²This section is based on Benz & Grigis (2002) and on Kundu, Schmahl, Grigis & Garaimov (2006).

³The research presented here was performed during the Summer of 2002, in order to be published in the special edition of Solar Physics on RHESSI's first results. Therefore, the level of solar activity is larger than what can be observed close to the minimum of the solar cycle.

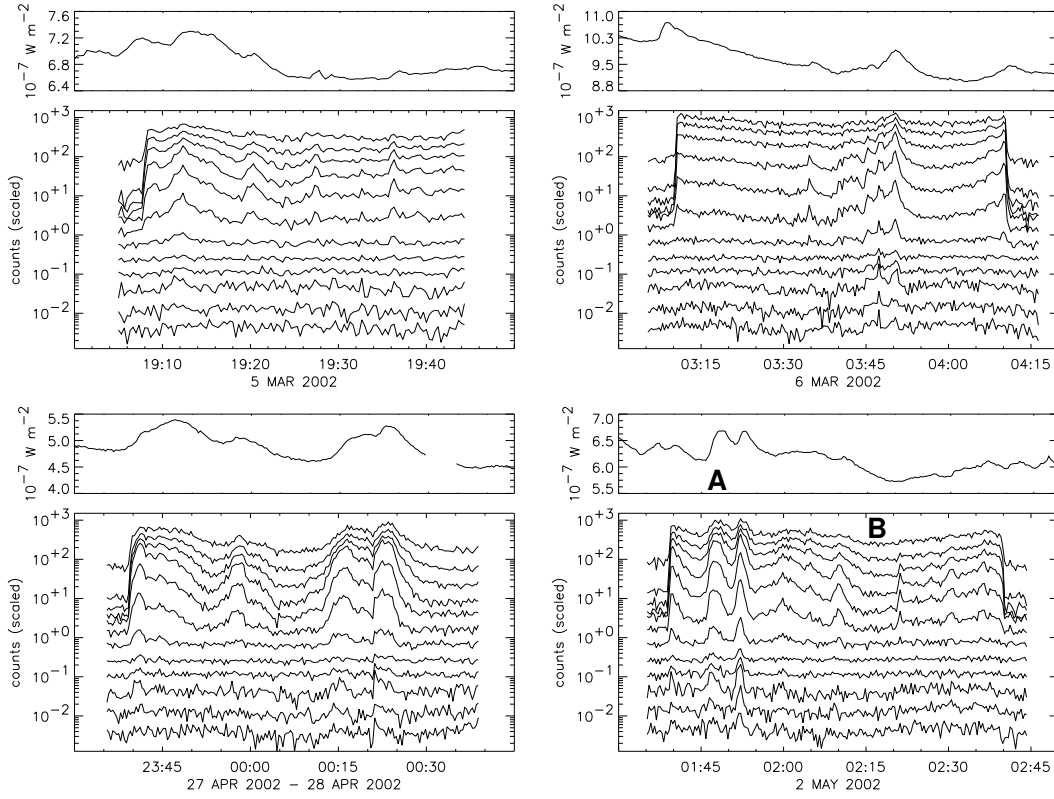


Figure 1.10: *Top of each panel:* GOES light curve in the 1–8 Å band. *Bottom of each panel:* RHESSI lightcurves in 1 keV wide channels from 3–4 keV (*top*) to 14–15 keV (*bottom*). Each channel is shifted such that it does not overlap with others. The time resolution is 20 seconds.

We note the following properties of the emission that can be clearly seen in Fig. 1.10:

- The channels lying between 5 and 9 keV show the largest variability.
- The peak of the emission above about 9 keV happens earlier than the peak of the lower energy emission.
- The event duration increases from high to low energies.
- In most events, there is no emission above the background beyond about 12 keV.

The microflares can be studied spectroscopically. The main results are listed here:

- A soft, low energy component, seen in all microflares, dominates the emission below about 10 keV. It can be fitted by an isothermal component with a temperature around 10 MK. The measured photon flux is

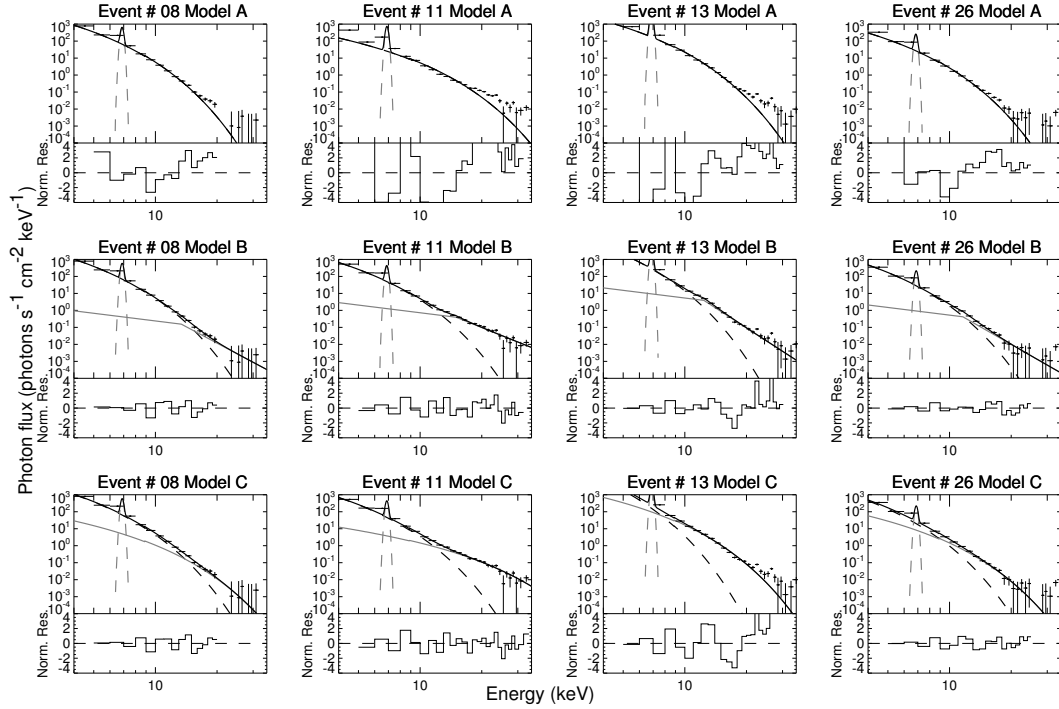


Figure 1.11: Spectra for 4 microflares. 3 different model were fitted: *A*: isothermal only; *B* isothermal and power-law; *C*: two isothermal at different temperatures.

enhanced around 7 keV, confirming the thermal interpretation: this is the signature of the iron line complex.

- A harder component can be seen in 24% of the events up to 15–20 keV. It can be fitted by either a power-law (with a spectral index of 5 or softer) or an hotter isothermal component (with temperature on the order of 25 MK).

Although the second component is weak and not much stronger than either the background or the thermal component, its reality is proven by the fact that it has a different time evolution than the first component, peaking early. An example of 4 events showing the different model components fitted is shown in Fig. 1.11. This high-energy component tends to be softer for microflares than for larger flare: this trend is confirmed by Battaglia et al. (2005).

Furthermore, it is possible to measure the spectrum of a quiet time, when no flare seems to be occurring, like the interval indicated as **B** in Fig. 1.10. A thermal component with a temperature of 6.4 MK fits the data. This can be interpreted as hot plasma trapped in the active region, having been heated by previous flares or by an ongoing activity of a superposition of large number of flares below the detection limit (see e.g. Arzner & Güdel 2004).

Conclusions relevant to the coronal heating problem that can be reached from these observations are:

- Microflares are just small flares: they behave similarly to large flares. The observation of both thermal and non-thermal components with physical parameters similar to larger flares, and acting on similar timescales, indicates that the same basic physical processes are acting: energy release by magnetic reconnection leading to electron acceleration.
- Microflares observed by RHESSI occur in active regions, like regular flares. They are thus different from the quiet Sun nanoflares. Therefore, they may contribute only to active-region coronal heating.
- The energy input by the microflares is difficult to estimate, because of the large uncertainties in the best-fit parameters of the thermal and non-thermal components. Also, it is more difficult to estimate the amount of energy going into waves, shocks, jets, energetic particle escaping from the sun.

To understand the importance of small flares, we first need a deeper understanding on the flare mechanism in general. Therefore, this thesis proceeds with the study of larger flares, where it should be easier to identify and understand the key physical processes acting.

Chapter 2

The spectral evolution of impulsive solar X-ray flares

*They sicken of the calm,
who knew the storm*

Dorothy Parker (1893–1967)

ABSTRACT: The time evolution of the spectral index and the non-thermal flux in 24 impulsive solar hard X-ray flares of GOES class M was studied in RHESSI observations. The high spectral resolution allows for a clean separation of thermal and non-thermal components in the 10–30 keV range, where most of the non-thermal photons are emitted. Spectral index and flux can thus be determined with much better accuracy than before. The spectral soft-hard-soft behavior in rise-peak-decay phases is discovered not only in the general flare development, but even more pronounced in subpeaks. An empirically found power-law dependence between the spectral index and the normalization of the non-thermal flux holds during the rise and decay phases of the emission peaks. It is still present in the combined set of all flares. We find an asymmetry in this dependence between rise and decay phases of the non-thermal emission. There is no delay between flux peak and spectral index minimum. The soft-hard-soft behavior appears to be an intrinsic signature of the elementary electron acceleration process.

2.1 Introduction

Non-thermal hard X-ray emission during impulsive solar flares is highly variable, often showing activity peaks and dips with durations ranging from seconds up to several minutes. This behavior can be observed in the largest X class flares as well as in smaller B and C class flares. It was early recognized (Parks & Winckler 1969; Kane & Anderson 1970) that the hardness of the photon spectrum can also change with time, and, furthermore, that there is a direct correlation between the hard X-ray flux and the spectral hardness. Since this implies that the flare spectrum starts soft, gets harder as the flux rises and softer again after the peak time, the term *soft-hard-soft* (SHS) was coined to describe this behavior. Later observations of major flares (Benz 1977; Brown & Loran 1985; Lin & Schwartz 1986; Fletcher & Hudson 2002; Hudson & Fárník 2002) confirmed the SHS pattern. However, flares were also observed that systematically hardened with time (Frost and Dennis 1971; Cliver et al. 1986; Kiplinger 1995), thus showing a *soft-hard-harder* (SHH) pattern. Current wisdom suggests that SHH flares represent gradual, long duration events. These are much less frequent than impulsive events.

The non-thermal photons usually follow a power-law distribution in energy. The power-law index, γ , can be directly related to the energy distribution of the electron flux impinging on the target (assuming a model for the bremsstrahlung emission), and implicitly to the acceleration process. The evolution of spectral index and flux reflects a development in the accelerator. Thus, the relation between index and flux is an observational constraint for acceleration theories.

While it seems to be well established that impulsive flares have an SHS spectral dynamic, much less is known about the *quantitative* relation, if any, between the photon spectral index and the non-thermal X-ray flux during the burst. The Reuven Ramaty High-Energy Solar Spectroscopic Imager (RHESSI) spacecraft (Lin et al. 2002), which observes hard X-rays and γ -rays from the Sun, is ideally suited to explore this relation. Its key features of high spectral resolution (1 keV in the X-ray range) and coverage of the low-energy range (down to 3 keV) allow us to separate the thermal continuum from the non-thermal component of the spectrum, to study also the 10-30 keV region where most of the non-thermal photons are emitted, to identify and account for peculiar spectral features (like breaks in the power-law etc.), and to follow the evolution of the non-thermal part right from the onset of the flare. Therefore, the spectral index and flux of RHESSI non-thermal photons can be studied with much higher precision than previously.

This Chapter presents a large set of measurements of the non-thermal component from 24 different solar flares and investigates quantitatively the relation between the non-thermal flux and the spectral index. The flares were selected in such a way as to represent the class of impulsive flares with strong non-

thermal emission. In Section 2.2 we give a detailed description of the selection and data reduction process that yields the dataset which is then analyzed in Section 2.3 and discussed in Section 2.4.

2.2 Observations and Data Reduction

Our main observational goal is the accurate study of the time evolution of the spectral index γ and the non-thermal X-ray flux in a representative sample of solar flares, using data from RHESSI. In this section we give a detailed account of the different steps that were undertaken in the data analysis process, starting from the event selection.

2.2.1 Event Selection

The event selection has to be very careful in order to pick a representative collection of flares. Ideally, one would analyze all the observed events or a randomly chosen subset thereof. In practice, however, instrumental issues reduce the freedom of choice, since not all the events are equally suitable for the different tasks of high precision spectral analysis. A detailed discussion about the RHESSI onboard detectors and their use for spectroscopy can be found in Smith et. al. (2002). We limited our analysis to flares having a peak soft X-ray flux larger than GOES class M1 and smaller than X1. These have fairly large count rates, but are not too heavily affected by pulse pileup. 176 M-class flares were reported in the RHESSI flare list in the period from 13 February 2002 to 31 November 2002. From this collection we restricted our analysis to the 79 flares observed with a constant attenuator state of 1 (thin attenuator in) and no front-segment decimation. Therefore we do not need to deal with attenuator motions and decimation state changes during the flare, and we have the best conditions for spectroscopy of M-class flares.

From this selection of 79 flares we dropped the ones which had no emission above the background in the 25–50 keV band, as determined by visual inspection of the observing summary light curves. Since we expect the bulk of the thermal radiation from M-class flares to be emitted mostly below 25 keV, this condition introduces a bias toward flares with substantial non-thermal emission. This is not a severe restriction, since we want to study specifically the non-thermal emission, and it would be very hard to ascertain the properties of any weak non-thermal emission anyway. In order to have enough data for meaningful time series, we additionally required the peak in the 25–50 keV band being more than 3 minutes away from any interruption in the data, as caused by the spacecraft entering or leaving the shadow of the Earth, the South Atlantic Anomaly (SAA), etc. We also dropped the events in which charged particle precipitation significantly increased the background counts during the

time of enhanced emission in the 25–50 keV band. These additional criteria dropped the number of events to 32.

2.2.2 Data Reduction and Analysis

For each event in the list, we determined:

- A contiguous time interval of sunlight containing the event without data gaps.
- The peak time of the observing summary count light curve in the energy band 25–50 keV.
- The RHESSI rotation period at peak time.
- The location of the source on the Sun.

The flare locations were taken from the automatically computed positions given by the RHESSI Experimental Data Center (HEDC) (Saint-Hilaire et al. 2002). Visual inspection of the corresponding images confirmed that in all cases correct and accurate positions were given, with the exception of 3 flares for which the RHESSI aspect solution (Fivian et al. 2002; Hurford & Curtis 2002b) quality was insufficient to permit reconstruction of meaningful images. We then proceeded to generate RHESSI count spectrograms for each flare in the uninterrupted sunlight time interval, with a time binning equal to the spin period at peak time (which in all cases is very close to 4 s) and an energy binning of 1 keV from 3 to 6 keV, 0.33 keV from 6 to 13 keV, 1 keV from 13 to 36 keV, 2 keV from 36 to 60 keV, 5 keV from 60 to 120 keV, 10 keV from 120 to 200 keV, 20 keV from 200 to 300 keV. Pileup correction was enabled with a deadtime threshold of 5%. We only used the front segments of the detectors, and systematically excluded the detectors 2 and 7, which have lower energy resolution. For some flares we also excluded detector 8 (which does not deliver good data when the onboard transmitter is active). The full spectral response matrix (SRM) was computed for each spectrogram, using the HEDC flare positions to enable position dependent corrections for the flares whose position was known. We discarded 2 events for which we were unable to generate the SRM.

To derive the spectral indices for the spectra, we use the forward fitting method implemented by the SPEX code (Smith et al. 2002; Schwartz et al. 2002). The procedure requires the user to choose a model photon spectrum, which is folded with the instrument response matrix and then fitted to the observed count spectrum. The best-fit parameters are given as output. To obtain the time evolution of the parameters, the fitting procedure is performed for each time bin in the spectrogram of the time interval of interest. We

have chosen to use a photon spectral model featuring a power-law with a low-energy turnover in addition to a thermal bremsstrahlung emission. The negative power-law index below the low-energy turnover was fixed at 1.5. Hence there are 5 free parameters in the model: the temperature T of the assumed isothermal emission and its emission measure \mathcal{M} ; for the non-thermal component the power-law index γ , the normalization of the power-law F_{E_0} at the (fixed) normalization energy E_0 and the low-energy turnover E_{turn} . The non-thermal part of the spectrum is thus given by

$$F(E) = \begin{cases} F_{E_0} \left(\frac{E}{E_0}\right)^{-\gamma} & E > E_{\text{turn}} \\ F_{E_0} \left(\frac{E_{\text{turn}}}{E_0}\right)^{-\gamma} \left(\frac{E}{E_{\text{turn}}}\right)^{-1.5} & E < E_{\text{turn}} \end{cases} \quad (2.1)$$

An example photon spectrum with an overlay of the best-fit model is shown in Fig. 2.1.

For all the events we selected background time intervals (preferentially before and after the flare) in each of the following 4 energy bands: 3–12, 12–30, 30–60, 60–300 keV. The counts in the different background intervals were then fitted to a polynomial of degree varying from 0 to 3, which was used to interpolate the background intensity during the event. We defined then the *fitting time interval* as the time when the emission in the band 30–60 keV was significantly above the background level.

2.2.3 Automatic Spectral Fitting

A time dependent determination of the model's best-fit parameters for 30 flares lasting a few minutes with 4 s data bins requires more than thousand fittings. To reduce the burden of the work involved in the data analysis, we implemented an automatic fitting procedure. However, automatic procedures have their own drawbacks, in particular if the fitting happens to converge towards a wrong local minimum of χ^2 , sometimes giving as a result spectacularly wrong fittings. We decided to settle for the following compromise: we let the fittings be computed automatically, but we visually inspected the results afterwards, and eliminated then the obviously wrong ones without making any attempt to recompute them. As a matter of fact, we iterated the procedure described above for a few rounds, each time improving the automatic fitting routine. After the last run we had to discard only a few fittings at the beginning and at the end of some fitting time intervals. Here follows a basic description of the algorithm used by the automatic fitting routine:

1. A fitting of T and \mathcal{M} for an isothermal emission is made in the low-energy range A shown in Fig. 2.1, where one can safely assume that the thermal emission is dominant.

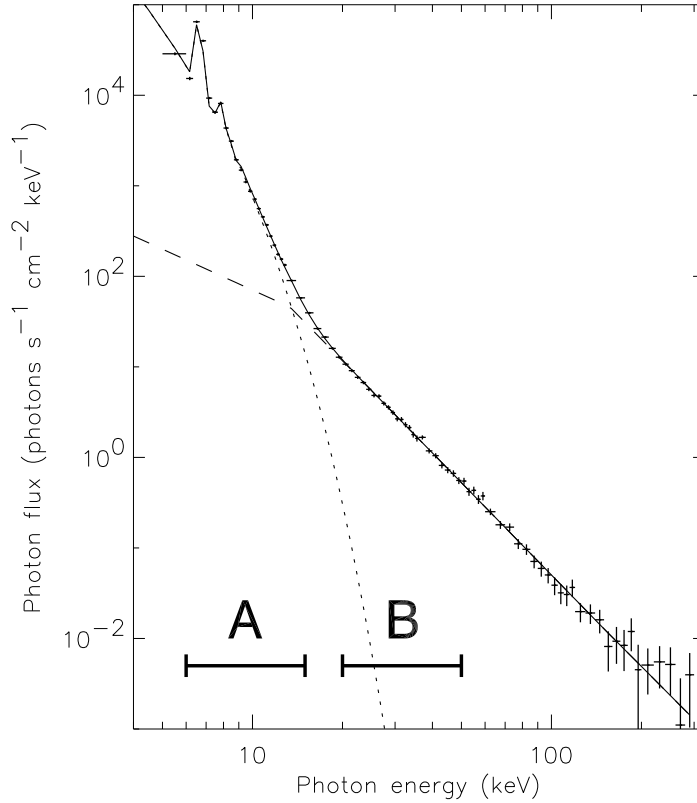


Figure 2.1: A RHESSI photon spectrum for 9 November 2002 at 13:14:16 UT, integrated over one rotation period of approximately 4 s. Overlaid on it, an isothermal bremsstrahlung emission (dotted line) with temperature $T = 16.7$ MK and emission measure $\mathcal{M} = 7.54 \cdot 10^{48} \text{ cm}^{-3}$, a power-law (dashed line) with spectral index $\gamma = 3.39$ and normalization $F_{50} = 0.525$, and a low-energy turnover $E_{\text{turn}} = 13.4$ keV. The continuous line represents the sum of these two components.

2. The range for the initial fit of the non-thermal part is defined as B in Fig. 2.1. If the emission does not exceed $0.1 \text{ photons s}^{-1} \text{ cm}^{-2} \text{ keV}^{-1}$ or five times the thermal emission as found in step 1, the range of the fit is reduced to the interval where it does satisfy these conditions.
3. A photon spectral model with a fixed thermal emission with T and \mathcal{M} as found in step 1 and a (not broken) power-law is fitted in the non-thermal range defined in step 2.
4. The parameters resulting from step 1 and 3 are used as initial estimates for the final fitting of all the 5 free parameters of the model to the spectrum in the energy range 6–150 keV. The low-energy turnover initial

estimate is taken as either the fitted E_{turn} from the previous spectrum in the time sequence, or a default value.

We emphasize that the first steps described above only provide the initial estimates for the parameters, which are then let *totally free* in the last fitting over the whole energy range. Steps 1–3 simply attempt to give reasonable initial guesses for the parameters. The energy ranges A and B and the default values used by the routine are fixed and were determined empirically to achieve the largest possible number of good fittings. We have experimented with alternative spectral models. They included for example models with a slightly hotter isothermal component, or two components of thermal emission, but no non-thermal emission. Such models fit the observed spectra with similar values of χ^2 , when the power-law index γ is greater than about 8.

2.2.4 Best-fit Parameters Selection and Results

The automatic fitting routine failed to provide results for 4 events. Its output consists of the best-fit parameters for a total of 1 566 spectral fittings from 26 events. The visual inspection of all the fittings allowed us to eliminate the spectra which were badly fitted because they would have required a broken power-law model. We also chose to discard all the spectra whose power-law component had an index similar to the logarithmic derivative of the thermal emission around the energy at which it was only about as strong as the background, because in such a case it is very difficult to ascertain the reality of any non-thermal emission.

After the selection process explained above, we were left with a total of 911 fittings for 24 events, spanning a total time of 3 722 s. The number of fittings for each event ranges from 5 to 212, with an average of 38. The 24 events with at least 5 good fittings are our final selection. They are listed in Table 2.1. Each fit consists of the 5 parameters T , \mathcal{M} , γ , F_0 and E_{turn} . All events are relatively short, have often many peaks and comply with the definition of impulsive flares.

Fitting free parameters to data may introduce hidden dependencies between them. It is important for the study of the index-flux relation to assess the effect of the fitting procedure. For this purpose we have compared the index-flux relation before and after fitting. For the flare of 9 November 2002 (the one with the longest time series) we computed two supplementary time series for the flux and spectral index from the uncalibrated count-rates total flux in the energy bands 26–35 keV and 35–44 keV and from their ratio. This is a much simpler and cruder way of determining the values of the two parameters that does not require fitting. Although the absolute values of the parameters will differ, they preserve the temporal variations.

Figure 2.2 shows an extremely close similarity between the uncalibrated

Table 2.1: List of the selected 24 events. Peak flux means the fitted non-thermal flux at 35 keV at peak time in photons $\text{s}^{-1} \text{cm}^{-2} \text{keV}^{-1}$. The peak time given reflects the time of maximum flux *after* the fitting selection, and may therefore not coincide with the peak of a light curve at 35 keV.

Event Nr.	Event date	Peak time	Peak flux	Peak γ	Number of fittings
1	20 Feb 2002	09:54:04	0.315	6.8	54
2	20 Feb 2002	16:22:58	0.168	3.8	11
3	20 Feb 2002	21:06:05	2.388	4.1	23
4	25 Feb 2002	02:56:42	0.390	5.5	29
5	26 Feb 2002	10:26:52	4.915	3.2	20
6	15 Mar 2002	22:23:06	0.243	4.9	125
7	04 Apr 2002	10:43:55	0.261	5.2	49
8	04 Apr 2002	15:29:16	2.124	4.7	32
9	09 Apr 2002	12:59:51	0.403	4.9	41
10	14 Apr 2002	03:24:44	0.715	4.6	13
11	17 Apr 2002	00:38:34	0.253	4.4	8
12	24 Apr 2002	21:50:23	0.712	4.0	16
13	01 Jun 2002	03:53:41	2.473	3.0	25
14	16 Aug 2002	22:10:30	1.629	4.9	18
15	17 Aug 2002	01:02:04	0.076	4.3	5
16	23 Aug 2002	11:59:05	0.220	6.4	14
17	24 Aug 2002	05:43:23	0.216	5.7	84
18	27 Aug 2002	12:28:38	1.617	3.1	8
19	29 Sep 2002	06:36:18	4.261	3.8	30
20	29 Sep 2002	14:46:43	0.405	3.9	40
21	30 Sep 2002	01:48:25	0.107	7.3	18
22	04 Oct 2002	00:41:13	1.109	4.6	20
23	09 Nov 2002	13:16:36	5.776	3.2	212
24	14 Nov 2002	22:24:40	1.978	3.8	16

count rates in the 26–44 keV energy range and the fitted flux. It proves that the fitting preserves the time evolution of the observed counts with high precision. The spectral ratio derived from uncalibrated counts in the two energy bands is normalized to the energy ranges, but differs from the fitted γ due to the lack of calibration. It is significantly noisier than γ because of the broader energy range used for the fitting, which includes non-thermal photons down to the thermal cross-over near 15 keV. Yet the two spectral parameters follow each other extremely well in time. This confirms that the dependence introduced by fitting is negligible.

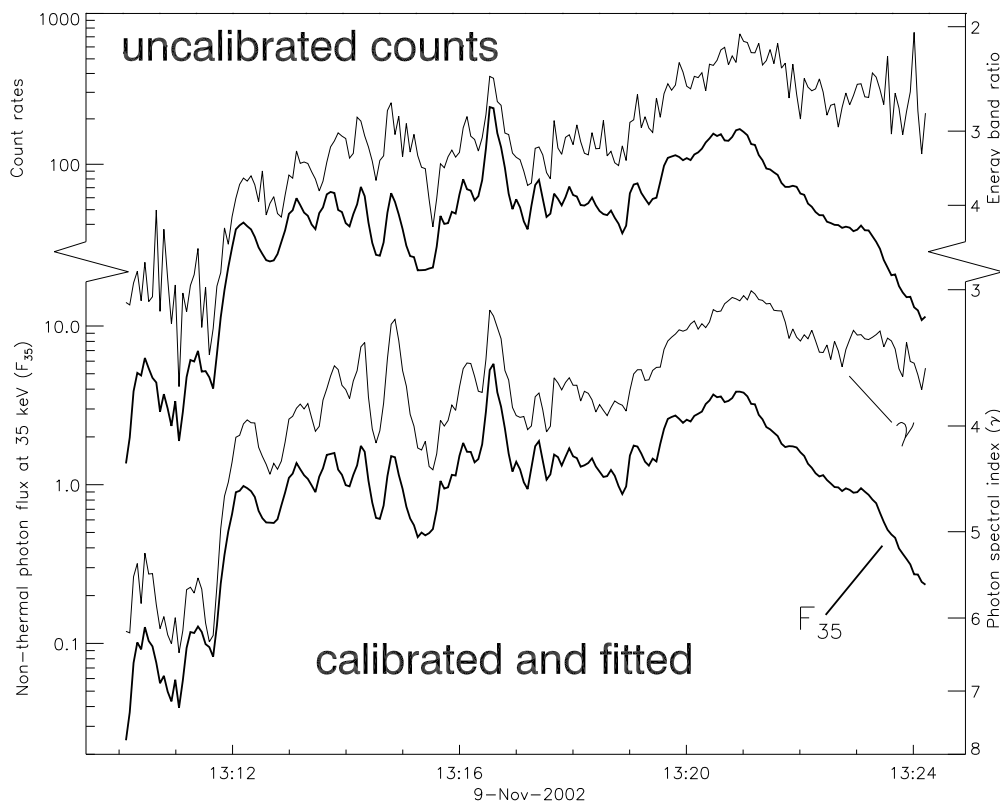


Figure 2.2: *Top*: Spectral index (thin line) and flux (thick line) obtained from the uncalibrated total count rates flux in the energy bands 26–35 keV and 35–44 keV and their ratio. *Bottom*: Spectral index γ (thin line) and non-thermal flux F_{35} at 35 keV in photons $\text{s}^{-1}\text{cm}^{-2}\text{keV}^{-1}$ (thick line) for the event of 9 November 2002, obtained by spectral fitting.

To further check that no cross-talk between thermal and non-thermal parameters is introduced by the fitting procedure, we smoothed the curve representing the temperature T as a function of time for flare 23 using a smoothing filter with a time window of 180 s, and recomputed all the fittings forcing the temperature to follow the smoothed curve. No significant differences were found between the new values obtained for the spectral indices and non-thermal fluxes and the old ones. This shows that any short-term variation of the fitted temperature during an emission peak do not significantly influence the behavior of γ and F_{35} .

2.3 Relation between Flux and Spectral Index

In this section we will investigate the relation between the spectral index and the non-thermal flux in a quantitative way. For the non-thermal flux there are

two options: the strength of the non-thermal flux F_{E_0} at a chosen, fixed normalization energy E_0 or the total non-thermal flux $F_{\text{tot}} = \int F(E) dE$. The first option has the disadvantage of requiring a supplementary arbitrary parameter E_0 . Therefore, it would be conceptually preferable to choose the second. However, the non-thermal flux is only observed in the energy range where it is larger than both the background and the thermal emission. Hence it is not straightforward to compute F_{tot} , because we do not know the non-thermal emission outside the observed range. The main uncertainty in F_{tot} comes from errors in the estimates of the low-energy turnover E_{turn} , especially for steep spectra, where small errors in E_{turn} can produce large changes in F_{tot} . Since spectral fittings are poorly suited to accurately determine E_{turn} and hence F_{tot} (for a detailed discussion, see Saint-Hilaire and Benz, 2005), the large uncertainties in F_{tot} rule out its use as a main parameter for our study. We are left with the first option, but we have to choose E_0 . It should lie in an energy range where the non-thermal emission is actually observed and fitted, to compare observable quantities. The non-thermal emission is best observed and identified in the energy range 20–50 keV, and hence we choose the center $E_0 = 35$ keV, and investigate the γ - F_{35} relation. In Section 2.4 we will consider the implications of changes in E_0 from the chosen 35 keV.

Fig. 2.3 presents a logarithmic plot of γ versus F_{35} for all of the 911 data points.

The plot clearly shows the overall SHS trend. The cross-correlation coefficient of $\ln \gamma$ versus $\ln F_{35}$ is $r = -0.80 \pm 0.03$, where the uncertainties given represent the 99% confidence range. The cross correlation coefficient r is significantly lower than 1 because of the scatter in the data, which is real and not due to measurement errors. The γ vs. F_{35} relation can be approximated by a power-law model

$$\gamma = AF_{35}^{-\alpha} \quad \text{or, equivalently,} \quad (2.2)$$

$$\ln \gamma = \ln(A) - \alpha \ln F_{35}. \quad (2.3)$$

In Eq. (2.2) and in the following, F_{35} is used as a dimensionless number given by the normalization factor at 35 keV divided by the unit flux ($1 \text{ photon s}^{-1} \text{ cm}^{-2} \text{ keV}^{-1}$). The constants A and α can be obtained by means of a linear least-squares (LS) regression of the quantities $\ln \gamma$ vs. $\ln F_{35}$. However we note that:

1. The γ - F_{35} data have a fairly large scatter.
2. We have to treat the variables γ and F_{35} symmetrically, since it is not *a priori* clear that one of them is a function of the other, and thus there is no reason to take either one as a *dependent* variable.

In such a case, Isobe et. al. (1990) suggest that the best fitting parameters are obtained by the LS bisector method. The method consists of taking the

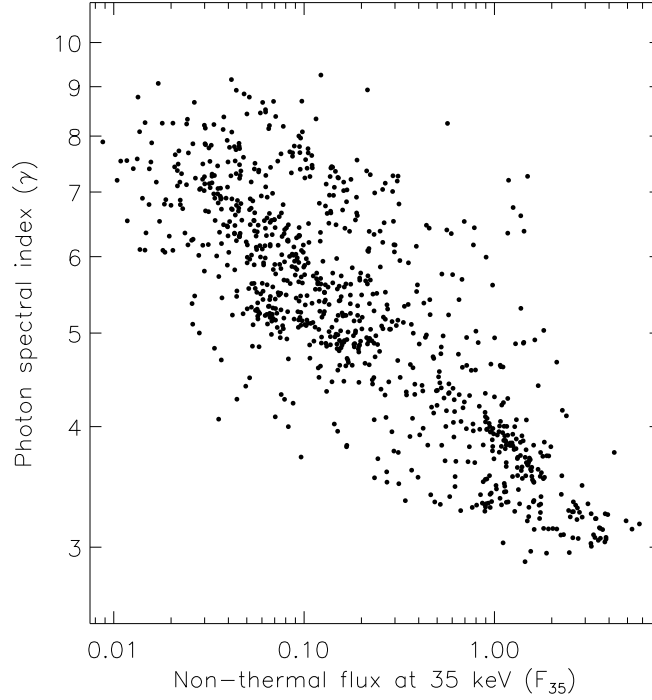


Figure 2.3: Plot of γ versus the fitted non-thermal flux at 35 keV (given in photons $\text{s}^{-1} \text{cm}^{-2} \text{keV}^{-1}$). All the 911 data points from the 24 events are shown.

line that bisects the $\text{LS}(\ln \gamma | \ln F_{35})$ and $\text{LS}(\ln F_{35} | \ln \gamma)$ regression lines, where $\text{LS}(y | x)$ means the least-square regression of the dependent variable y against the independent variable x . The LS bisector gives for our model parameters: $A = 4.043 \pm 0.032$ and $\alpha = 0.197 \pm 0.003$. Computing α by $\text{LS}(\ln \gamma | \ln F_{35})$ we get $\alpha = 0.154 \pm 0.003$, and using $\text{LS}(\ln F_{35} | \ln \gamma)$ $\alpha = 0.241 \pm 0.006$. The latter two values define a confidence range for α , such that $\alpha = 0.20 \pm 0.05$. These values will be refined in the following. They may be used for a future comparison, e.g. with a peak-flux analysis.

The overall behavior of the plot in Fig. 2.3 results from the superposition of points from different flares. We now want to look in some more detail at the behavior of single flares. Fig. 2.4 gives the time evolution of γ and F_{35} for 4 flares.

Anti-correlation of F_{35} and γ can clearly be seen in all of them. However, it is evident from a close inspection of the light curves that a model of a strict functional dependence like the one of Eq. (2.2) will not work well for an entire flare, since there are consecutive peaks in F_{35} with about the same height, but having different minimum values of γ . Nevertheless each peak shows an unmistakable SHS pattern. It seems likely that the proposed power-law model

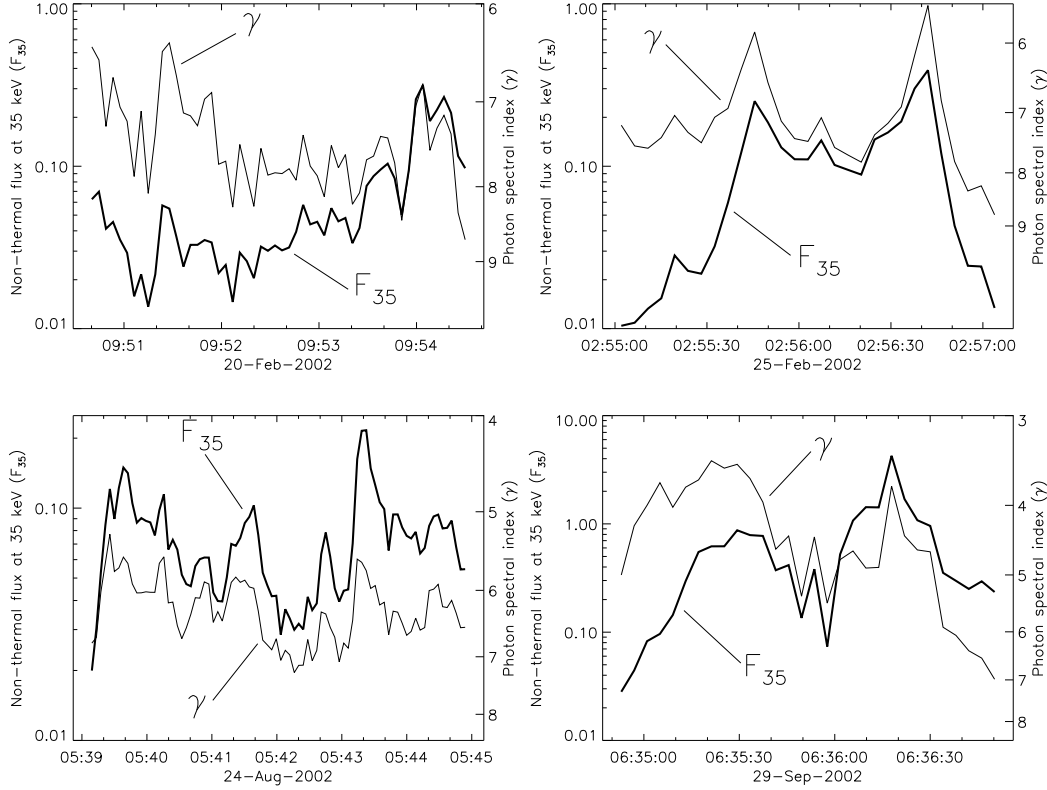


Figure 2.4: Time evolution of the photon spectral index γ (thin line) and the non-thermal flux at 35 keV F_{35} (thick line) for 4 flares.

suits better the behavior of single peaks than whole flares. To check this, we computed the vertical scatter of the data points around their $\text{LS}(\ln \gamma | \ln F_{35})$ regression line for the set of all the data points, for the 24 subsets of points belonging to each flare, and for 141 subsets of points belonging to 70 rise and 71 decay phases of peaks during the flares. The rise and decay phases were selected with the requirement that each phase consists of at least 3 consecutive data points. The vertical scatter σ_I of a subset I of n points $(\ln F_{35}^i, \ln \gamma^i)$, $i \in I$ around the straight line defined by Eq. (2.3) with $\text{LS}(\ln \gamma | \ln F_{35})$ parameters slope α_I and intercept $\ln A_I$ can be computed by

$$\sigma_I^2 = \frac{1}{n-2} \sum_{i=1}^n \left(\ln \gamma^i - \ln A_I + \alpha_I \ln F_{35}^i \right)^2, \quad (2.4)$$

where $n-2$ are the degrees of freedom of the subset with the fitted straight line. For the set of all 911 points $\sigma = 0.165$. The average of σ computed for each single flare is 0.094. The average of σ for each rise and decay phase is 0.020 and, respectively, 0.017. The improvement in sigma going from the total dataset to the flares and then to the rise/decay phases shows that indeed single

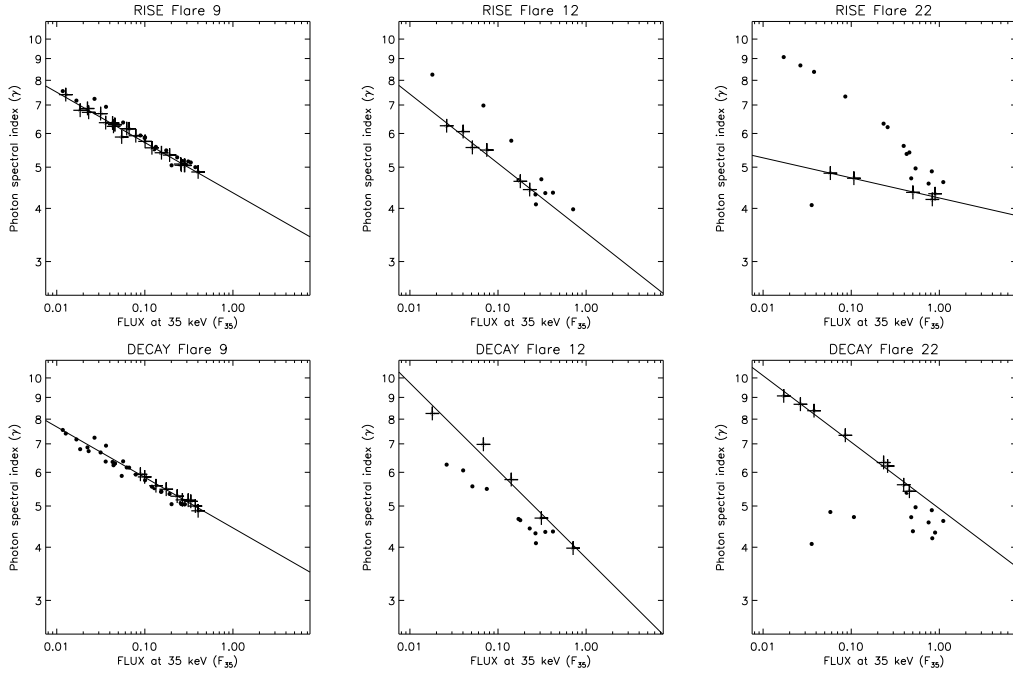


Figure 2.5: Spectral index γ versus flux at 35 keV F_{35} for 3 flares. The plus signs in the top and bottom row of plots mark the points forming the longest uninterrupted rise and decay phase in the flare. The regression line of the selected data points is shown.

peaks are better represented by the model, in the sense that they have much less vertical scatter around the regression line.

Fig. 2.5 shows the γ vs. F_{35} plot for three events. For each flare, the points belonging to the longest rise (top row) and decay (bottom row) phase are represented by plusses and their $\text{LS}(\ln \gamma | \ln F_{35})$ regression line is drawn. Since here we have much less scatter, there is little difference between the different LS regression schemes. It can be seen that the scatter around the fitted line is low during the rise/decay phases. Interestingly, in some flares the fitted line is steeper in the decay phases.

We show the distribution of the slope of the fitted lines in Fig. 2.6.

The bin width is 0.5 standard deviations of the measured slopes. The average value for the rise phase is

$$\alpha_r = 0.121 \pm 0.009 \quad (2.5)$$

and the one for the decay phase is

$$\alpha_d = 0.172 \pm 0.012. \quad (2.6)$$

The standard deviations are $\sigma_r = 0.073$ and $\sigma_d = 0.103$, respectively.

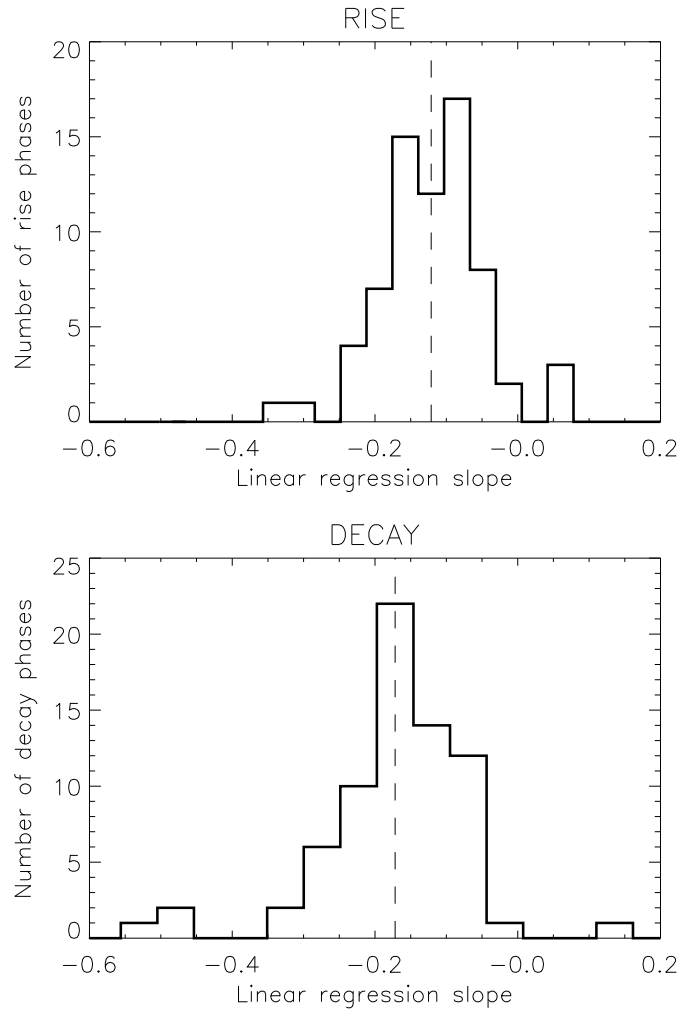


Figure 2.6: Distribution of the linear regression slopes for the rise and decay phases. The average value is marked by the dashed line.

The difference in averages is about 5 times the standard errors of the mean, and therefore the difference between the two cases is statistically significant. We see that for most of the rise phases there is a soft-hard trend (negative slope) and for most of the decay phases there is a hard-soft trend (also described by a negative slope). The number of rise phases with slope smaller than 0.04 are 5 out of 70, and the number of decay phases with slope smaller than 0.04 are 2 out of 71. Therefore the SHS behavior is a nearly universal trend in peaks of non-thermal emission.

We also investigated whether there is a significant delay in the correlation of F_{35} and γ . We defined the delay as the time of the minimum of the quadratic interpolation curve going through the 3 cross-correlation coefficients

corresponding to a lag of -1 , 0 and 1 time bins of about 4 seconds. The interpolation enhances considerably the time resolution, as the noise is small. The distribution of the delays is relatively broad, centered at -0.32 s, with a standard deviation of 1.1 s and with extreme delays up to ± 3 s. The average of the delays does not significantly differ from 0 since the standard error of the mean is ± 0.23 s.

Furthermore, we tried to see if there is any evidence in the data for the presence of a *pivot point*, i.e. a fixed point with coordinates (E^*, F^*) common to all the spectra in a rise/decay phase. We note that such a concept corresponds to a model that does not yield a power-law dependence of F_{35} and γ , but instead

$$\gamma = -\frac{\ln(F^*/F_{35})}{\ln(35\text{keV}/E^*)}, \quad (2.7)$$

contrary to Eq. (2.2). We computed the intersections of the power-law fits to the non-thermal component of the photon spectrum of all 4 s time bins in each rise phase of every flare with all other non-thermal components in the same phase. While this procedure is quite sensitive to errors for nearly parallel lines, the total distribution yields a clue whether there is any virtue in the idea of a pivot point. The energy distribution of the intersections peaks around 9 keV, and was larger than half of the maximum in the energy range 6.5–12.5 keV, but it had comparatively large tails to very low and very high energies. There seems to be no real pivot point, but the region of intersection is relatively narrow. Therefore, when trying to visualize the time evolution of the non-thermal spectrum during the rise phase, one does not too badly by imaging the spectrum as fixed at an energy around 10 keV. In the course of the flare the non-thermal spectrum rises its high-energy tail until peak time, and it lowers it again afterwards.

2.4 Discussion

The power-law model for the γ - F_{35} relation is admittedly very simple, yet it provides a good empirical description of the observed quantities. The range of validity of the model is limited at very high flux values, since γ has a theoretical lower limit at roughly 1.4, given by the bremsstrahlung of a monoenergetic beam. Its major disadvantage is the arbitrary assumption of a normalization energy, here 35 keV. How do the results shown in Section 2.3 depend on the choice $E_0 = 35$ keV?

Let E_1 and $E_2 = E_1 + \Delta E$ be two normalization energies. The normalization coefficients F_{E_0} and F_{E_1} satisfy

$$F_2 = F_1 \left(\frac{E_2}{E_1} \right)^{-\gamma}. \quad (2.8)$$

Now let us assume that the relation $\gamma = A_1 F_1^{-\alpha_1}$ holds. Using Eq. (2.8), this can be written as

$$\ln \gamma = \ln A_1 - \alpha_1 \ln F_2 - \alpha_1 \gamma \ln \frac{E_2}{E_1}. \quad (2.9)$$

If $\Delta E/E_1 \ll 1$, we can expand the logarithm and get

$$\ln \gamma = \ln A_1 - \alpha_1 \ln F_2 - \alpha_1 \gamma \frac{\Delta E}{E_1}. \quad (2.10)$$

The logarithmic derivative of the this expression yields

$$\frac{d \ln \gamma}{d \ln F_2} = \frac{-\alpha_1}{1 + \alpha_1 \gamma \frac{\Delta E}{E_1}} \approx -\alpha_1 \left(1 - \alpha_1 \gamma \frac{\Delta E}{E_1} \right). \quad (2.11)$$

The $\ln \gamma$ - $\ln F_{E_2}$ relation is not linear, as γ appears on the right hand side of Eq. (2.11). If a new exponent α_2 were fitted to the $\ln \gamma$ - $\ln F_{E_2}$ data points, we would get according to Eq. (2.11),

$$\alpha_2 \simeq \alpha_1 \left(1 - \alpha_1 \gamma \frac{\Delta E}{E_1} \right). \quad (2.12)$$

For $\Delta E \ll E_1$ the relation between $\ln \gamma_2$ and $\ln F_{E_2}$ is still approximately linear but flatter than for $\ln F_{E_1}$ if $\Delta E > 0$. This is confirmed in Fig. 2.7, where the γ vs. F_{E_0} relation is shown for different normalization energies E_0 . In Fig. 2.7 the γ - F_E relation is presented according to Eq. (2.9). In the course of a subpeak the spectral index and flux move approximately on one of the lines according to the given normalization energy, assuming the relation (2.2). The relation steepens with decreasing normalization energy E_0 and finally turns over. In a model with a pivot point at energy E^* the γ - F_{E_0} relation would be a vertical line for $E = E^*$.

The final goal of this thesis is the comparison of these results with the prediction of theoretical models for the energy distribution of accelerated electrons (see Chapters 3 and 4). For this purpose the electron distribution needs to be reconstructed from the observed photon spectrum. As an example, the analytically solvable thick target impact model using the nonrelativistic Bethe-Heitler cross section (Brown 1971, Tandberg-Hanssen and Emslie 1988) predicts that an electron power-law distribution $\Phi(\epsilon) = \Phi_{\epsilon_0} (\epsilon/\epsilon_0)^{-\delta}$ [electrons $\text{s}^{-1} \text{keV}^{-1}$] generates a photon spectrum $F(E) = F_{E_0} (E/E_0)^{-\gamma}$ [photons $\text{s}^{-1} \text{cm}^{-2} \text{keV}^{-1}$] with

$$\delta = \gamma + 1 \quad (2.13)$$

and

$$\Phi_{\epsilon_0} = K F_{E_0} E_0^\gamma \epsilon_0^{-\delta} \frac{(\delta - 1)(\delta - 2)}{\beta(\delta - 2, 1/2)}, \quad (2.14)$$

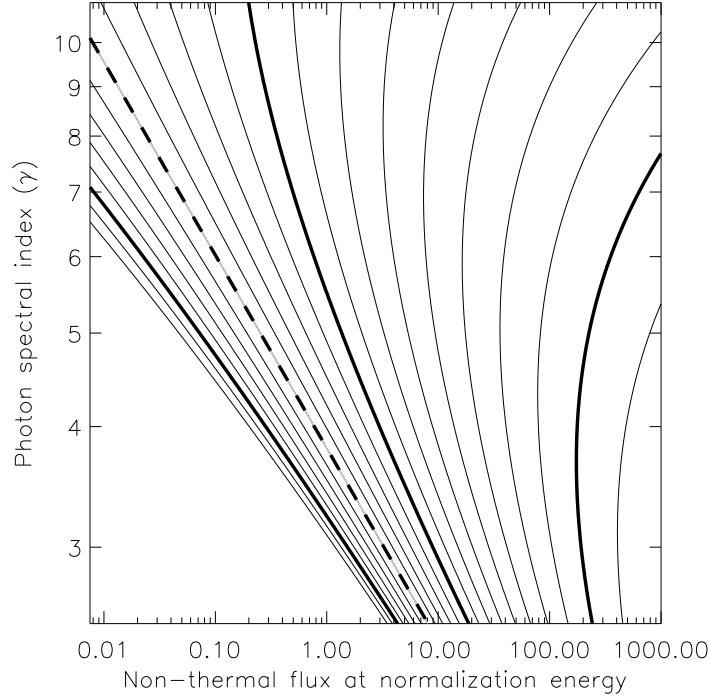


Figure 2.7: The lines shown here models the relation between the spectral index γ and the non-thermal flux F_{E_0} at different energies E_0 , assuming that $\gamma = AF_{35}^{-\alpha}$ holds at $E_0 = 35$ keV with $\alpha = 0.2$ and $A = 3.8$. The dashed line correspond to $E_0 = 35$ keV, the lower thick line to $E_0 = 45$ keV, the upper thick lines to, respectively, $E_0 = 25$ keV and $E_0 = 9$ keV. The separation between thin lines is 2 keV.

where $\beta(x, y)$ is the beta function and the constant K is given by

$$K = \frac{3\pi^2 e^4 \ln \Lambda D^2}{Z^2 \alpha r_e^2 m_e c^2} \simeq 6.6 \cdot 10^{33} \text{ keV cm}^2, \quad (2.15)$$

where $\ln \Lambda$ is the Coulomb logarithm, D the distance from the target (here 1 AU), Z the average atomic number, α the fine structure constant and r_e the classical electron radius. Eq. (2.14) indicates that the relation between electron flux and gamma will not conserve linearity in the log-log representation. In other words, the assumed linear relation for fitting photons must be considered as a convenient but rather arbitrary approximation.

2.5 Conclusion

This study of the γ - F relation in the evolution of the non-thermal component of impulsive solar flare hard X-ray emissions exploits the high spectral resolution

of the RHESSI germanium detectors. Contrary to earlier investigations, the spectral index is not derived from the ratio of a few channels, but from fitting the spectrum at relatively low non-thermal energies where most of the photons are emitted. This method eliminates the influence of the thermal component and improves considerably the noise on the derived spectral index (Fig. 2.1).

The most surprising result of the improved accuracy is the appearance of the soft-hard-soft behavior on short time scales. The SHS behavior is a feature seen in nearly all of the non-thermal emission peaks of M-class solar flares. Whereas SHS was previously considered to be a global property of flares, Figs. 2.2 and 2.4 demonstrate that SHS is a predominantly short-scale phenomenon. This is the reason why the scatter in the γ - F_{35} plot diminishes when rise and decay phases of individual subpeaks are analyzed separately.

The novel quantitative analysis of the γ - F_{35} relation has also revealed remarkable properties. The relation appears linear in double-logarithmic representation (Fig. 2.3). Thus it follows an approximate power law, $\gamma = AF_{35}^{-\alpha}$. Its average index α is 0.197 ± 0.003 . The scatter is greatly reduced if individual subpeaks are studied (Fig. 2.5). In the rise phase of individual flare elements, the average index $\alpha_r = 0.12 \pm 0.01$ is significantly smaller than the index of the decay phase $\alpha_d = 0.17 \pm 0.01$ (Fig. 2.6). The path of a subpeak in the γ - F_{35} plot (Fig. 2.5) follows tendentially a slanted V, with the rise phase forming the flatter leg. This amounts to a secondary trend, superimposed on the SHS behavior, of a general spectral softening of the non-thermal component in the course of a subpeak.

The SHS behavior supports the idea that each non-thermal emission peak represents a distinct acceleration event of the electrons in the flare. The individual peaks mainly differ by their value for A in the $\gamma = AF_{35}^{-\alpha}$ relation, presumably due to different physical parameters in the acceleration region.

It is possible to visualize the γ - F_{35} relation by a pivot point in the non-thermal spectrum. This point is relatively stable in energy and flux. The pivot energy was determined as 9 keV in the average with a half-power distribution of 6.5–12.5 keV. In the course of a peak, the non-thermal spectrum rises by turning around the pivot point, decreasing γ and increasing the flux beyond the energy of the pivot point. In the decay phase the spectrum decreases and turns the opposite way. The picture is supported by the observations of no delay (in the average). We note, however, that the pivot-point model is only an approximation and needs to be further investigated.

The SHS phenomenon of flares, and in particular of subpeaks, contradicts the idea of the statistical flare in avalanche models (Lu & Hamilton 1991), assuming that each flare and subpeak is composed of many identical elements that are far below resolution. The superposition of such subresolution structures in a straightforward avalanche process would not yield the observed SHS time behavior.

The subpeaks defined by the SHS behavior thus may be considered as

irreducible flare elements. They have durations of one minute (Fig. 2.2) to shorter than 8 seconds, the lower limit given by the time resolution (Fig. 4). The close correlation suggests that there is an intrinsic dependence between the flux and energy distribution of electrons for any given elementary acceleration event. If this is the case, it implies that individual SHS structures cannot be further resolved, thus form the elementary structures of flares.

Chapter 3

Comparison of Observation with Models

Everything is vague to a degree you do not realize till you have tried to make it precise.

Bertrand Russell (1872–1970)

ABSTRACT: We study the evolution of the spectral index and the normalization (flux) of the non-thermal component of the electron spectra observed by RHESSI during 24 solar hard X-ray flares. The quantitative evolution is confronted with the predictions of simple electron acceleration models featuring the soft-hard-soft behavior. The comparison is general in scope and can be applied to different acceleration models, provided that they make predictions for the behavior of the spectral index as a function of the normalization. A simple stochastic acceleration model yields plausible best-fit model parameters for about 77% of the 141 events consisting of rise and decay phases of individual hard X-ray peaks. However, it implies unphysically high electron acceleration rates and total energies for the others. Other simple acceleration models such as constant rate of accelerated electrons or constant input power have a similar failure rate. The peaks inconsistent with the simple acceleration models have smaller variations in the spectral index. The cases compatible with a simple stochastic model require typically a few times 10^{36} electrons accelerated per second beyond a threshold energy of 18 keV in the rise phases and 24 keV in the decay phases of the flare peaks.

3.1 Introduction

The intense hard X-ray emission observed during solar flares is the direct signature of the presence of highly energetic supra-thermal electrons. The quest for a viable particle acceleration mechanism drives both theoretical and observational investigations. In his review on particle acceleration in impulsive solar flares Miller (1998) presents “the major observationally-derived requirements” for particle acceleration. The two main observational facts cited by Miller and used to put constraints on the electron acceleration mechanisms are the time scales of the acceleration (1 s for acceleration from thermal energies to 100 keV) and the acceleration rates (10^{36} to 10^{37} electrons s^{-1} accelerated above 20 keV, to be sustained for several tens of seconds). Interestingly, the shape of the accelerated electron spectrum and its evolution in time are barely mentioned.

In Chapter 2 we have analyzed X-ray observations looking for systematic trends in the spectral evolution of 24 impulsive solar flares and confirmed the predominant *soft-hard-soft* (SHS) behavior of the observed photon spectra, first noted by Parks & Winckler (1969). This not only applies to the global evolution, but is even more pronounced in individual peaks. We also give a simple quantitative description of the SHS pattern, deriving an empirical relation between the normalization of the non-thermal component of the photon spectrum and its spectral index. Can this systematic trend in the evolution of the hard X-ray photon spectrum be used to put constraints on acceleration mechanisms? As pointed out already in Chapter 2, the SHS behavior contradicts the idea that the flux evolves by a varying rate of identical, unresolved events, termed ‘statistical flare’ in avalanche models (Lu & Hamilton 1991).

Here we study the constraints the new quantitative information on the SHS behavior puts also on other acceleration models. Some conventional simple acceleration scenarios (presented in Section 3.3) are tested whether they can reproduce the observed spectral behavior and what constraints on their parameters can be obtained. Our goal is to demonstrate the method, to stimulate further comparisons between observation and theory and to call attention to the fact that the spectral evolution cannot be neglected by a successful acceleration theory. While the scenarios presented here are admittedly simple, we think that this first step will be extended in the near future to encompass more sophisticated models.

The main piece of information that we use for this comparison is the relation between the normalization of the non-thermal component of the spectrum (assumed to be a power-law) and its spectral index. Chapter 2 studied this relation for photon spectra. Here, we go a step further, and recover the electron spectra assuming an emission from a thick target, which also yields a power-law spectrum for the electrons. Therefore we can use the data from Chapter 2

and convert the photon spectral index and normalization to the corresponding values for the electron spectra. This yields discrete time series of the spectral index $\delta(t)$ and the power-law normalization $\Phi_{\epsilon_0}(t)$ at energy ϵ_0 . The acceleration models described in Section 3.3 provide theoretical functions $\Phi_{\epsilon_0}(\delta)$ depending on the model parameters, which can be fitted to the observed pairs $(\delta(t), \Phi_{\epsilon_0}(t))$. Applying this repeatedly for different flares and different emission peaks during flares, the distributions of the best-fit model parameters can be derived.

We summarize in Section 3.2 the data reduction process yielding the dataset. It is used in Section 3.4 for the comparison with the models described in Section 3.3.

3.2 Observations and Data Reduction

We give here a brief summary of the data reduction process, described in full detail in Chapter 2. The photon spectral data used for this work is exactly the same as the dataset used in Chapter 2, where hard X-ray observations from the Reuven Ramaty High Energy Solar Spectroscopic Imager (RHESSI) of 24 solar flares of GOES class between M1 and X1 have been analyzed. For each event count spectra were generated with a cadence of one RHESSI rotation (amounting to about 4 seconds). Each spectrum was fitted with a model consisting of an isothermal emission (bremsstrahlung continuum and atomic emission lines) characterized by a temperature T and an emission measure \mathcal{M} , and a non-thermal component characterized by a power-law with index $-\gamma$, normalization F_{E_0} at energy E_0 , and low-energy turnover at energy E_{turn} . The full detector response matrix was used to calibrate the spectra.

The fittings were done by means of an automatic routine, but were checked one by one, excluding cases where the thermal and non-thermal emissions could not be reliably separated, or the non-thermal part was not well represented by a single power-law. After this selection we had a total of 911 good fittings for 24 events. For this work, we just use the time series of the spectral index γ and the normalization of the power law F_{E_0} for all the 24 events. The non-thermal component of the spectrum is thus approximated by

$$F(E) = F_{E_0} \left(\frac{E}{E_0} \right)^{-\gamma}, \quad (3.1)$$

where $F(E)$ is the photon flux at 1 AU in photons $\text{s}^{-1} \text{cm}^{-2} \text{keV}^{-1}$.

We now go one step further than Chapter 2 and transform the photon spectra into electron spectra. We choose the well-known analytically solvable thick target impact model (using the nonrelativistic Bethe-Heitler cross section and collisional energy losses) to recover the injected electron spectrum. It is

still a power-law

$$\Phi(\epsilon) = \Phi_{\epsilon_0} \left(\frac{\epsilon}{\epsilon_0} \right)^{-\delta}, \quad (3.2)$$

where $\Phi(\epsilon)$ is the total number of electrons $\text{s}^{-1} \text{keV}^{-1}$ over the whole target. The electron spectral index is given by

$$\delta = \gamma + 1 \quad (3.3)$$

and the electron spectrum normalization is

$$\Phi_{\epsilon_0} = K F_{E_0} E_0^\gamma \epsilon_0^{-\delta} \frac{(\delta - 1)(\delta - 2)}{\beta(\delta - 2, 1/2)}, \quad (3.4)$$

where $\beta(x, y)$ is the beta function, and the constant K is given by

$$K = \frac{3\pi^2 e^4 \ln \Lambda D^2}{Z^2 \alpha r_e^2 m_e c^2} \simeq 6.4 \cdot 10^{33} \text{ keV cm}^2 \quad (3.5)$$

(Brown 1971). This transformation yields the time series $\Phi_{\epsilon_0}(t)$ and $\delta(t)$, which will be used for the comparison with the acceleration models.

The transformation of the observed photon spectrum into an electron spectrum can potentially alter the results of the comparison between observations and models, since it requires a knowledge of the physical conditions in the emission region, of their evolution in time and of the importance of the energy loss processes. However, this is a necessary step for the comparison with acceleration models. For simplicity we have neglected the effects of photon reflection in the photosphere (albedo) and nonuniform target ionization.

The assumption of a thick target leaves open the origin of temporal variations. In the following, we will assume that they are due to the acceleration rather than to a variable release of trapped particle.

3.3 Acceleration Scenarios

We present here the frameworks of two acceleration scenarios, the *constant productivity scenario* and the *stochastic acceleration scenario*, which we will compare with the data on spectral flare evolution. A scenario can comprise different models. All models are required to yield a power-law distribution Φ in electron energy ϵ (Eq. 3.2). A specific model is defined by a unique functional relation between the spectral index δ and the spectrum normalization Φ_{ϵ_0} . The relation depends on some model parameters, which are assumed to be constant during a flare or a subpeak. This enables us to compare the model function with the observed dataset $(\delta(t), \Phi_{\epsilon_0}(t))$. The first scenario is based on *ad hoc* assumptions, while the second is derived from a stochastic electron acceleration

model considered e.g. by Benz (1977). Newer models along the stochastic acceleration line, like the transit-time damping model proposed by Miller et al. (1996), do not imply a simple functional relationship, and therefore cannot be included at this stage. The spectral evolution of transit-time acceleration must be calculated numerically and is not yet available. Petrosian & Liu (2004) also give plots of electron spectra calculated from their model of stochastic acceleration by parallel waves, but do not predict the time evolution of the spectra either. For a quantitative comparison between observations and theory, we are limited to models making concrete and usable predictions on the relation between spectral index and power-law normalization.

3.3.1 The Constant Productivity Scenario

A class of models may be defined assuming that the *productivity* of the accelerator is constant above a threshold energy ϵ_* . Either the electron acceleration rate N (electrons s^{-1}) to energies above ϵ_* or the total power P input to electrons above ϵ_* are held constant, but the acceleration process evolves in such a way that flux and index vary. Although such processes have never been proposed, they may fit some of the data. Upon integrating Eq. (3.2), the models give the following relations between the electron spectral index δ and the electron spectrum normalization Φ_{ϵ_0} :

$$\Phi_{\epsilon_0} = \frac{N(\delta - 1)}{\epsilon_*} \left(\frac{\epsilon_*}{\epsilon_0}\right)^\delta \quad (\text{constant rate model}) \quad (3.6)$$

$$\Phi_{\epsilon_0} = \frac{P(\delta - 2)}{\epsilon_*^2} \left(\frac{\epsilon_*}{\epsilon_0}\right)^\delta \quad (\text{constant power model}) \quad (3.7)$$

The total power in Eq. (3.7) is expressed in the somewhat unusual unit of keV s^{-1} . The power in erg s^{-1} can be easily obtained multiplying P by the conversion factor $1.602 \cdot 10^{-9} \text{ erg keV}^{-1}$.

3.3.2 The Stochastic Acceleration Scenario

The index-flux relation in stochastic acceleration was explored by Benz (1977) and further elaborated by Brown & Loran (1985). In this model plasma waves accelerate stochastically the electrons in a plasma slab. From the diffusion equation for the electron distribution function Benz gets the approximate relation (corresponding to Eq. 20 in Benz, 1977, with the spectral index transformed from the electron *number* distribution into the corresponding value for the electron *flux* distribution)

$$\delta = -\frac{1}{2} + \frac{8e^2 \ln \Lambda n}{\pi W_0} + \frac{\sqrt{2}\epsilon_*}{\pi e \sqrt{W_0 L}} =: -\frac{1}{2} + \mathbf{d} + \mathbf{e}, \quad (3.8)$$

where e is the electron charge, $\ln \Lambda$ the Coulomb logarithm, n the ambient plasma electron density, L the length of the plasma sheet and W_0 the time-dependant spectral energy density in the waves causing the acceleration. Following Brown & Loran (1985), we recognize that the term \mathbf{d} can be written as $\mathbf{d} = \alpha e^2$ with

$$\alpha = \frac{4\pi e^4 \ln \Lambda n L}{\epsilon_*^2} = \frac{L}{L_{\text{MFP}}}, \quad (3.9)$$

where L_{MFP} is the Coulomb collisional mean free path of the electrons in the plasma sheet. The acceleration process needs $L_{\text{MFP}} \gg L$ to be effective, and therefore $\alpha \ll 1$. Benz argues that the total electron flux Φ_{TOT} above ϵ_* is proportional to $W_0 L$, that is

$$\Phi_{\text{TOT}} = K W_0 L. \quad (3.10)$$

Using Eqs. (3.8) and (3.10) we get the following relation $\Phi_{\epsilon_0} \leftrightarrow \delta$

$$\Phi_{\epsilon_0} = \left(\frac{\epsilon_*}{\epsilon_0}\right)^\delta \frac{C(\delta-1)}{\epsilon_*} \left(\frac{1 + \sqrt{1 + 4\alpha\left(\delta + \frac{1}{2}\right)}}{2\left(\delta + \frac{1}{2}\right)}\right)^2, \quad (3.11)$$

where $C = 2K\epsilon_*^2/(\pi^2 e^2)$. In the collisionless case $\alpha = 0$ it simplifies to

$$\Phi_{\epsilon_0} = \left(\frac{\epsilon_*}{\epsilon_0}\right)^\delta \frac{C}{\epsilon_*} \frac{\delta-1}{\left(\delta + \frac{1}{2}\right)^2}. \quad (\text{stochastic acceleration model}) \quad (3.12)$$

Figure 3.1 shows the spectra for different values of δ and their $\Phi_{\epsilon_0}(\delta)$ according to Eqs. (3.6), (3.7) and (3.12). Interestingly, the model described by Eq. (3.12) has the special property that all the spectra cross each other in a very narrow region of the plot, therefore exhibiting a behavior very similar to the one given by the *pivot-point model*¹ described in the following.

The pivot-point model assumes that all the non-thermal power-law spectra in the time series cross each other in an unique point. This pivot point is characterized by its energy ϵ_* and its flux Φ_* . The following relation holds between the spectral index δ and the power-law normalization Φ_{ϵ_0} at energy ϵ_0

$$\Phi_{\epsilon_0} = \Phi_* \left(\frac{\epsilon_*}{\epsilon_0}\right)^\delta \quad (\text{pivot-point model}) \quad (3.13)$$

The relation between δ and Φ_{ϵ_0} is given by Eqs. (3.6), (3.7), (3.11), (3.13) for, respectively, the constant rate model, the constant power model,

¹Throughout the text we use this orthographic convention: pivot point is written without a hyphen when it is used as a noun, but with a hyphen when it is used adjectivally, e.g. pivot-point energy.

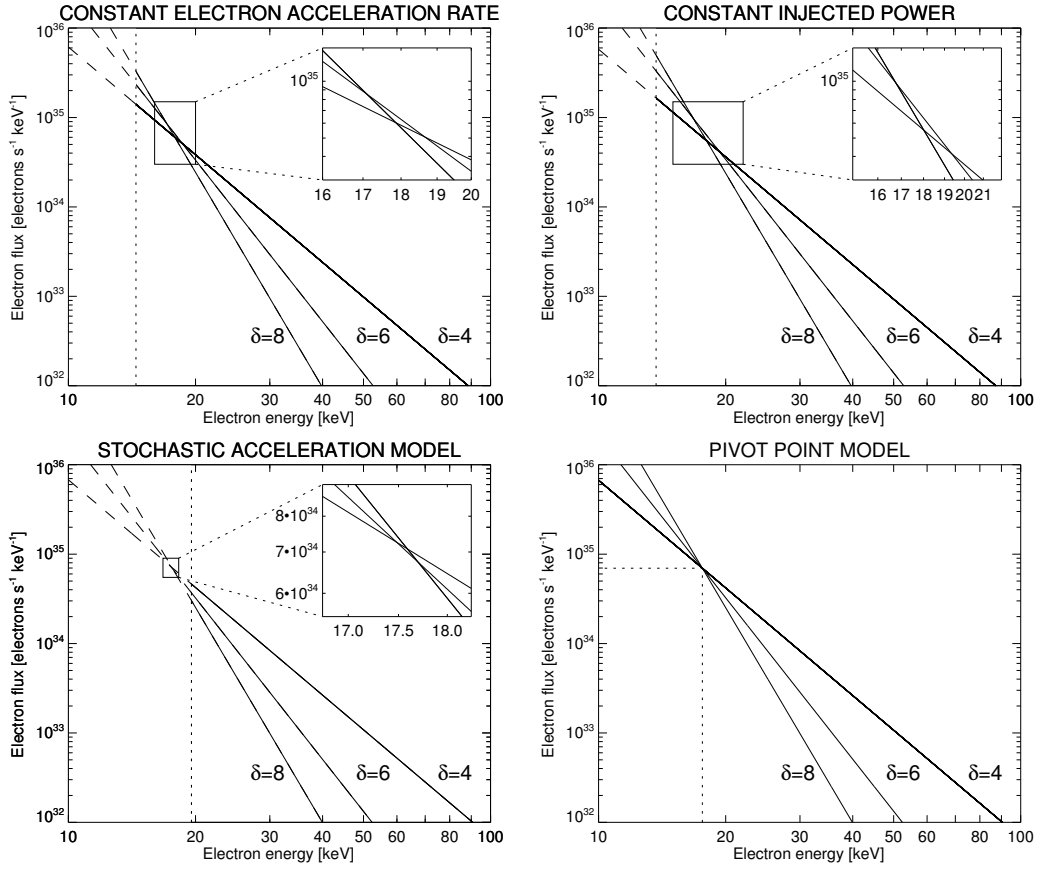


Figure 3.1: Electron energy spectra with spectral indices of $\delta = 4, 6, 8$ for each of the four models indicated on top and presented in Section 3.3. The vertical dashed line represents the lower energy threshold ϵ_* for the first 3 models, and the pivot-point energy in the last plot.

the stochastic acceleration model and the pivot-point model. All models depend on two free parameters assumed to be constant during a flare or an emission peak. The threshold energy for the first 3 models and the energy of the pivot point in the last model have been all represented by the same symbol ϵ_* , such that it is easier to compare the different equations. When more distinction is needed we will refer to them as ϵ_*^{RATE} , $\epsilon_*^{\text{POWER}}$, ϵ_*^{STOC} and ϵ_*^{PIV} for the different models. The second parameter, denoted N , P , C , Φ_* , respectively, characterizes the flux normalization in the 4 models.

3.3.3 Relations with the Pivot-Point Model

We now compute the energy of the approximate pivot point ϵ^{PIV} which results from a stochastic acceleration model given by the parameters $(C, \epsilon_*^{\text{STOC}})$ with $\alpha = 0$. To compute the position of the pivot point, we find first the position

of the intersection point of two spectra given by $\delta_1, \Phi_1 = \Phi_{\epsilon_0}(\delta_1)$ and $\delta_2, \Phi_2 = \Phi_{\epsilon_0}(\delta_2)$ in the stochastic acceleration model. Since the spectra are straight lines in logarithmic representation, using Eqs. (3.2) and (3.12) it is straightforward to find for the intersection ϵ_{INT}

$$\ln \frac{\epsilon_{\text{INT}}}{\epsilon_*^{\text{STOC}}} = \frac{\ln \Phi_2 - \ln \Phi_1}{\delta_2 - \delta_1} = \frac{\ln \frac{\delta_2-1}{\delta_1-1} - 2 \ln \frac{\delta_2+\frac{1}{2}}{\delta_1+\frac{1}{2}}}{\delta_2 - \delta_1} \quad (3.14)$$

To find the approximate pivot point, we take the limit of the previous expression for $\delta_2 \rightarrow \delta_1$. Putting $\delta_1 = \delta$ and $\delta_2 = \delta + \Delta$ with the condition that $\Delta/\delta \ll 1$, we get to the first order in Δ/δ

$$\ln \frac{\epsilon_{\text{INT}}}{\epsilon_*^{\text{STOC}}} = -\frac{\delta - \frac{5}{2}}{(\delta - 1)(\delta + \frac{1}{2})}. \quad (3.15)$$

Therefore two spectra with spectral index around δ will have a common point at

$$\epsilon_{\text{INT}} = \epsilon_*^{\text{STOC}} \cdot \exp\left(-\frac{\delta - \frac{5}{2}}{(\delta - 1)(\delta + \frac{1}{2})}\right) =: \epsilon_*^{\text{STOC}} \cdot f(\delta). \quad (3.16)$$

The function $f(\delta)$ depends weakly on delta for $\delta > 3$, and therefore all the spectra will cross each other in a narrow energy and flux range. The energy of the corresponding pivot point is approximately $\epsilon^{\text{PIV}} = \epsilon_{\text{INT}} \simeq \epsilon_*^{\text{STOC}} \cdot f(6) = 0.90 \epsilon_*^{\text{STOC}}$. Similar relations holds approximatively also for the other models:

$$\epsilon^{\text{PIV}} \simeq \epsilon_*^{\text{RATE}} \cdot \exp\left(\frac{1}{\delta - 1}\right) \quad (3.17)$$

$$\epsilon^{\text{PIV}} \simeq \epsilon_*^{\text{POWER}} \cdot \exp\left(\frac{1}{\delta - 2}\right) \quad (3.18)$$

In the constant productivity models, the pivot point has an energy which is slightly larger than ϵ_* , and in the stochastic acceleration model the pivot-point energy is slightly lower than ϵ_* . Therefore in these models most accelerated electrons have energies comparable with the pivot-point energy. On the other hand, the purely phenomenological pivot-point model does not request the presence of electrons at energies close to the pivot-point energy: the pivot point may be *virtual* in the sense that the electron energy distribution may be a power-law at higher energies and turnover at an energy $\epsilon^{\text{TURN}} > \epsilon^{\text{PIV}}$.

3.4 Comparison with the Data

3.4.1 Fittings in δ - Φ_{ϵ_0} Plane

We proceed now to compare the observed evolution of the spectra with the models presented in the previous section. The dataset described in Section 3.2

consists of discrete time series of the electron spectral index $\delta(t_i)$ and of the power-law normalization $\Phi_{\epsilon_0}(t_i)$ at energy ϵ_0 at the times t_1, t_2, \dots, t_n for the 24 different flares. For each model described in Section 3.3 we have a relation between Φ_{ϵ_0} and δ , and the comparison of the data is done by a least-square fitting of the inverse function $\delta(\Phi_{\epsilon_0}, \mathbf{P})$ to the observed pairs $(\Phi_{\epsilon_0}(t_i), \delta(t_i))$, where \mathbf{P} is the model parameter vector. Since the spectral index δ varies over a smaller factor than the flux normalization Φ_{ϵ_0} , it is better to use the latter as independent variable for the fitting, and therefore we use the inverse function $\delta(\Phi_{\epsilon_0})$ instead of $\Phi_{\epsilon_0}(\delta)$. The choice of ϵ_0 is arbitrary, but we settled for $\epsilon_0 = 60$ keV, consistent with the observed range of electron energies. Chapter 2 remarked that the scatter of the data is smaller on average for time series belonging to rise or decay phases of the non-thermal emission peaks. A given rise or decay phase is defined as a series of at least three consecutive points showing an increase or a decrease of the flux. Therefore we independently fit the model parameters to each rise and decay phase.

Figure 3.2 shows (Φ_{60}, δ) points consequent in time measured for three flares. The constant rate and stochastic acceleration models corresponding to the best fit to the rise and decay phases are both shown in all graphs. In each fit the model parameters are constant in time. The curves corresponding to the two different models are nearly identical because Eqs. (3.6) and (3.12) are functionally similar. The two other models (constant power and pivot point) yield curves (not shown in Fig. 3.2) which also are much alike the ones shown.

3.4.2 Comparing Model Parameters

As a next step we compare the best-fit parameters between the different models. Is one of the models preferable, yielding more plausible values? Note that there is an evident correlation between the two parameters of each model. It is due to the fact that the points (δ, Φ_{60}) of each phase lie approximately on straight lines with different slopes, but all of them passing near the point $(\Phi_{60} = 10^{31} \text{ electrons s}^{-1} \text{ keV}^{-1}, \delta = 6.5)$. This geometrical constraint in the δ - Φ_{60} plane is the cause of the correlation between the two model parameters: if ϵ_* is small, N , P , C , or Φ_* , respectively, must be large. The distributions of the best-fit model parameters for the constant rate and the stochastic acceleration model are presented in Fig. 3.3 separately for the rise and decay phases. Since the parameters vary over several orders of magnitude, we chose a logarithmic representation.

Table 3.1: Results of model fitting to the observed evolution of the spectral index and non-thermal flux in the rise and decay phases of the non-thermal emission peaks.

Model	Equation for $\Phi_{\epsilon_0} \leftrightarrow \delta$	Phase	Nr. of phases	Nr. of phases in fit region	Nr. of phases in $3\text{-}\sigma$ region	Fitted variable	Centroid of the distribution ^a	Half width of the distribution ^b
Constant rate	(3.6)	Rise	70	64	52	N	$5.70 \cdot 10^{35}$ el. s ⁻¹	15
		Decay	71	68	56	ϵ_*	13.9 keV	1.6
						N	$2.05 \cdot 10^{35}$ el. s ⁻¹	8.4
						ϵ_*	18.6 keV	1.5
Constant power	(3.7)	Rise	70	64	51	P	$1.18 \cdot 10^{37}$ keV s ⁻¹	8.3
		Decay	71	67	55	ϵ_*	13.6 keV	1.6
						P	$5.85 \cdot 10^{36}$ keV s ⁻¹	4.5
						ϵ_*	17.6 keV	1.4
Stochastic acceleration	(3.12)	Rise	70	64	55	C	$8.09 \cdot 10^{36}$ s ⁻¹	16
		Decay	71	69	56	ϵ_*	18.1 keV	1.7
						C	$2.23 \cdot 10^{36}$ s ⁻¹	7.8
						ϵ_*	24.2 keV	1.4
Pivot point	(3.13)	Rise	70	63	53	Φ_*	$9.39 \cdot 10^{34}$ el. s ⁻¹ keV ⁻¹	18
		Decay	71	67	56	ϵ_*	17.5 keV	1.6
						Φ_*	$1.28 \cdot 10^{34}$ el. s ⁻¹ keV ⁻¹	11
						ϵ_*	22.3 keV	1.4

(a) centroid of the best fit 2-dimensional Gaussian distribution

(b) expressed as a multiplicative factor

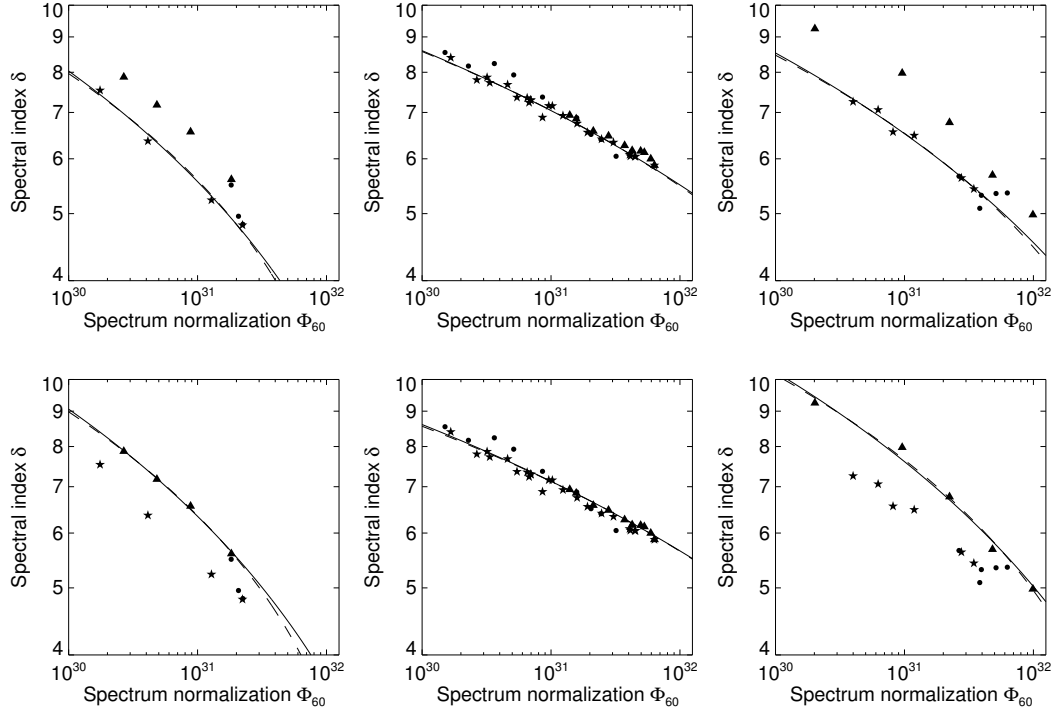


Figure 3.2: Plot of the spectral index δ vs. the spectrum normalization Φ_{60} for different times in three flares (first column: 20 Feb. 2002 09:54, second column: 04 Apr. 2002 15:29, third column 17 Apr. 2002 00:39). The points belonging to a certain rise phase are represented by stars, the points belonging to a decay phase are represented by triangles and the other points are marked by dots. The evolution of the constant rate and the stochastic acceleration model are represented by the dashed and full lines, respectively. In the upper row they were fitted to the rise phase points, in the lower row to the decay phase points.

In all the four models, we found that most of the parameters are concentrated in a relatively narrow region, except for about 20–30% of the points lying far away from the peak of the distribution. The average value and standard deviation of the distribution are poor estimators of the position and width of the central peak in such a case. Instead, we characterized the distributions by fitting two-dimensional Gaussian functions to the data. This procedure yields a reasonable estimate for the position and width of the distribution's peak. To further ensure that outliers do not have strong influence, we restricted the fit to the region where $\epsilon_* > 0.1$ keV and the second fit parameter is smaller than 10^{45} (in each parameter's units). The number of cases in the region to be fitted is given in Table 3.1, and its range is displayed in Fig. 3.3. The model parameter distribution must be binned for the fitting procedure. We chose

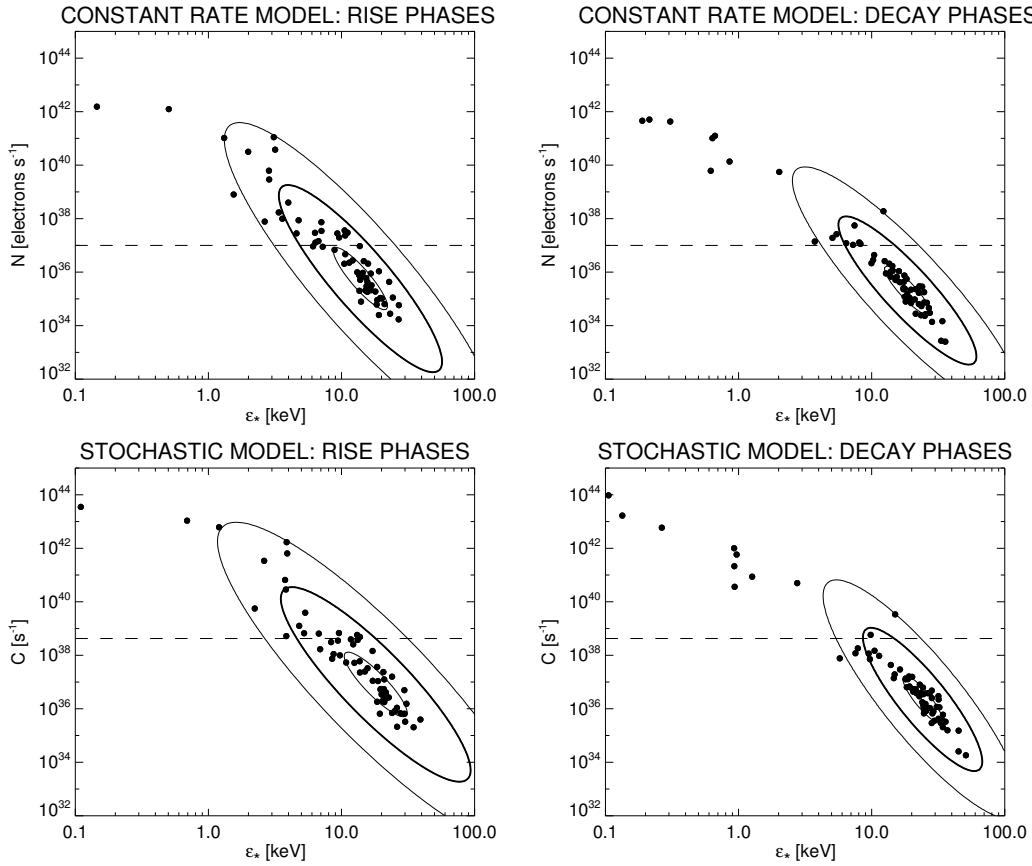


Figure 3.3: Best-fit model parameters for the stochastic acceleration and the constant rate model, separately for the rise and decay phases. Contour lines corresponding to 1σ , 3σ (thick line) and 5σ levels for a Gaussian peak fitted to the data are also shown. The region under the dashed line has an electron acceleration rate lower than 10^{37} electrons s^{-1} for events with spectral index $\delta = 6$.

bins centered on the median values of the two parameters and with a width of 0.5 times the average deviation from the median.

In Fig. 3.3 the contour lines corresponding to the 1σ , 3σ (thick line) and 5σ levels of the two-dimensional Gaussian distribution are superimposed on the data. We define the *outliers* as being the points outside the 3σ contour line. The number of outliers is about 23 % and does not vary significantly in the different models and phases (Table 3.1).

The outliers correspond to rise or decay phases where the spectral index changes little as the flux increases or decreases. In the framework of the pivot-point model: if the pivot point for the spectrum lies at very low energy and high flux, it is possible to have large variations at high energies with small changes in the spectral index. The other 3 models behave in a fashion similar

to the pivot-point model (as shown in Fig. 3.1), so this explication also applies for them.

With the exception of the pivot-point model, the parameters of the other models have a direct physical meaning. We can check if they lie in an acceptable range when compared with other observations and generally accepted values on solar flares. For the sake of simplicity and uniformity, we derive first the total power injected in the accelerated electrons (in erg s⁻¹) and the acceleration rate of electrons (in electrons s⁻¹) for the different models. The following equations express the electron acceleration rate $N = \int_{\epsilon_*}^{\infty} \Phi(\epsilon) d\epsilon$ as a function of the model parameters:

$$N^{\text{RATE}} = N, \quad (3.19)$$

$$N^{\text{POWER}} = \frac{P(\delta - 2)}{\epsilon_*(\delta - 1)}, \quad (3.20)$$

$$N^{\text{STOC}} = \frac{C}{(\delta + \frac{1}{2})^2}. \quad (3.21)$$

The following equations express the power $P = \kappa \int_{\epsilon_*}^{\infty} \epsilon \Phi(\epsilon) d\epsilon$ as a function of the model parameters:

$$P^{\text{RATE}} = \kappa N \epsilon_* \frac{\delta - 1}{\delta - 2}, \quad (3.22)$$

$$P^{\text{POWER}} = \kappa P, \quad (3.23)$$

$$P^{\text{STOC}} = \kappa C \epsilon_* \frac{\delta - 1}{(\delta - 2)(\delta + \frac{1}{2})^2}, \quad (3.24)$$

where $\kappa = 1.602 \cdot 10^{-9}$ erg keV⁻¹.

Figure 3.4 shows the distribution of the acceleration rate and the electron power for the constant rate model and the stochastic model, for both the rise phases (gray) and the decay phases (black). The distributions show a central peak and an extended tail to the right. Rise and decay phases in the tail represent about the same subset in all models, requiring extremely high values for both acceleration rate and power. This is due to the fact that these phases fit models having a very low threshold energy ϵ_* , and the integral of the spectrum diverges in the limit $\epsilon_* \rightarrow 0$. The low value of ϵ_* is necessary to account for the events where the spectral index varies slowly during the phase.

What are the maximum values acceptable in reality? The interpretation of hard X-ray observations of solar flares requires a large number of accelerated electrons. In his review on the flare mechanism, Sweet (1969) already requires 10^{36} electrons s⁻¹ to account for the observed hard X-ray emission. Brown & Melrose (1977) derive a requirement of $5 \cdot 10^{36}$ electrons s⁻¹ accelerated above 25 keV. Miller (1998) cites 10^{36} – 10^{37} electron s⁻¹ above 20 keV. Recent RHESSI observations of X class solar flares yield similar values (e.g. Holman et al. 2003,

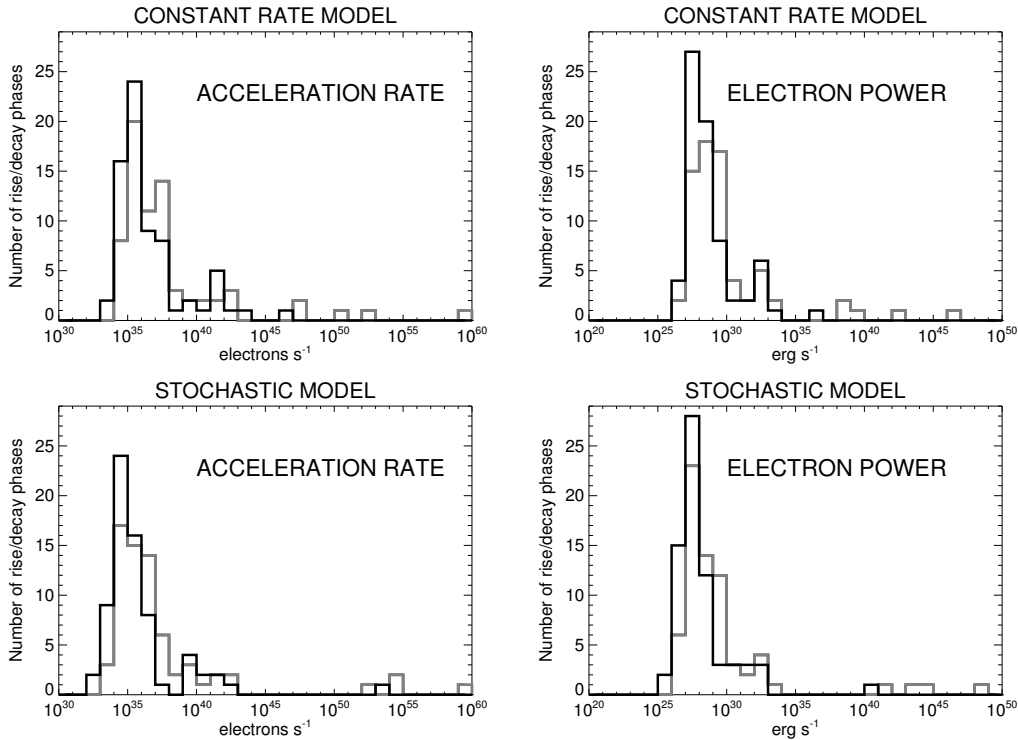


Figure 3.4: Distribution of the electron acceleration rate (left column) and the total power in the accelerated electrons (right column) for the constant rate model (upper row) and the stochastic model (lower row). The distributions are shown in gray for the rise phases and black for the decay phases. The tail of the distribution to the right of the main peak contains events with unphysically high values for the rates and powers.

Saint-Hilaire & Benz 2005). If the non-thermal electron spectrum extends to energies lower than 20 keV, this number could be higher. This usually does not contradict the observations, since during a large flare, the photon flux at energies lower than 20 keV is typically dominated by thermal emission. From a theoretical point of view the number of flare electrons and energy available in the active region environment is limited. Some mechanism for electron replenishment needs to be operative but is often left unspecified. Therefore it is not clear how the sustainable electron acceleration rate is limited. As an upper limit for comparison with our results, we take as the highest reported electron acceleration rate $N^{\text{MAX}} = 10^{37}$ electron s⁻¹. There is also a physical limit on the power that can be injected into the accelerated electrons. As a generally acceptable maximum power P^{MAX} , we will assume 10^{29} erg s⁻¹ in agreement with the above cited authors.

Some of the derived model parameters are highly implausible, requiring acceleration rates and power input far exceeding the above limits. In Fig. 3.3

the limit for $\delta = 6$ is indicated in the N - ϵ_* and C - ϵ_* planes. Table 3.1 gives the number of cases in total, as well as in Fig. 3.3 and in the region used for fitting a Gaussian distribution. Figure 3.3 indicates that most rise and decay phases below the limit of plausibility are within the $3\text{-}\sigma$ limit of the distribution, and thus corroborate the Gaussian fit. Its centroid and half-widths (in log presentation) are given in Table 3.1.

Since we follow the time evolution of the spectra from the onset of the non-thermal emission, there is a large difference of more than 2 order of magnitude between the value of the minimum and maximum normalization Φ_{60} . Surprisingly, the clustering of phases in the N - ϵ_* and C - ϵ_* planes (Fig. 3.3) indicate that most flare peaks can be interpreted by models within a relatively small range of threshold energies ϵ_* . The second model parameters N , P , C , Φ_* are spread upon a larger range. They include the effect of the different sizes of the non-thermal emission peaks of our sample. Note that ϵ_* is smaller in the rise phase than in the decay of a flare peak on average. On the other hand, the normalization is larger in the rise phase on average.

Gan (1999) reported the presence of a pivot point in the SMM/GRS spectra of two X-class flares. His results of 41 keV and 77 keV for the energy of the pivot point of the electron spectra are larger than ours. This may be due to the fact that he analyzed larger events, or that he fitted energies mostly above our energy range, thus possibly above an high-energy break in the spectrum.

The value of the spectral wave energy density W_0 in the stochastic acceleration model can be computed. From Eqs. (3.10), (3.21) and $C = 2K\epsilon_*^2/(\pi^2 e^2)$ we get:

$$W_0 L = \frac{2\epsilon_*^2}{\pi^2 e^2 (\delta + \frac{1}{2})^2} \quad (3.25)$$

Using the average values of $\epsilon_* = 20$ keV and $\delta = 6.4$, this amounts to

$$W_0 \simeq 2 \times 10^{-6} \left(\frac{10^7 \text{cm}}{L} \right) \text{ erg cm}^{-2}. \quad (3.26)$$

This value is somewhat lower than the ones cited in Benz (1977) and Brown & Loran (1985), because we have used a lower value of ϵ_* and a larger value of δ . In the stochastic model, the total energy density $U_T = \int W(k) dk$ in the turbulent waves can be computed by

$$U_T \simeq \frac{W_0}{\lambda_D} \simeq 3 \times 10^{-5} \sqrt{\frac{n_e}{10^{10} \text{cm}^{-3}}} \text{ erg cm}^{-3}, \quad (3.27)$$

where λ_D is the Debye length. It is well below the magnetic energy density, which is larger than unity.

3.5 Discussion

The four models presented in Section 3.3 are based on different assumptions, but have similar functional relationships between the electron spectral index δ and the non-thermal spectrum normalization Φ_{e_0} , as required by observations. As a consequence, it is possible to visualize the spectral evolution of all these models by the presence of a common *pivot point* in the non-thermal electron spectra during the rise or decay phase of each hard X-ray peak. This general property however, inhibits selecting the best model from spectral fits.

The comparison of the observed evolution of the non-thermal spectrum during rise and decay phases of a non-thermal emission peak with the models yields best-fit model parameters. Considering the simplicity of the assumed models it is surprising that the distribution of the model parameters is reasonable for about 77% of the 141 observed rise/decay phases, but yields an unphysically high electron acceleration rate for the rest of the observed events. The numbers of outliers is not statistically different between the models.

The events in the unphysical region of parameter space manifest themselves as the enhanced tail of the two-dimensional distribution shown in Fig. 3.3. The simple models do not succeed in describing these events, which all exhibit a slowly varying spectral index. These models would totally fail to reproduce events with constant spectral index. The mathematical reason of the failure is that these models just assume power-law behavior of the observed electron distribution above a fixed threshold energy ϵ_* . To account for the events with slowly varying spectral index, the fit converges toward very low values of ϵ_* , whereas the models can be justified only in the case where ϵ_* is larger than about a few keV. More sophisticated models, like the one proposed by Miller et al. (1996) or Petrosian & Liu (2004), explicitly accelerate non-thermal electrons *out of a thermal distribution*. They do not show a power-law behavior at low energy and therefore should be less susceptible to such low-energy divergencies.

The best-fit model parameters show an asymmetry between the rise and decay phases of the emission peaks. Such an asymmetry was already reported in Chapter 2. In the constant productivity scenario, this would correspond to a reduced productivity of the accelerator in the decay phase. Similarly, the fitting to the stochastic acceleration model suggests a lower electron acceleration rate on average for the decay phase.

3.6 Conclusion

We compared observations (described in Chapter 2) from RHESSI on the evolution of the normalization and spectral index of the non-thermal component during emission peaks of solar flares with model predictions by fitting the

model parameters to the observed values for the electron spectral index δ and the spectrum normalization Φ_{60} at 60 keV (as shown in Fig. 3.2). All the models selected for this study, described in Section 3.3, feature the soft-hard-soft behavior for a single flare peak and fit well the observed spectral evolution of flare peaks. We have shown in Section 3.3 that they have a functional dependence between δ and Φ_{60} which closely resembles the one given by the pivot-point model (Eq. 3.13). For this reason the data cannot discriminate between models.

While it is possible to fit reasonably well the models to the observed data, the resulting model parameters imply unphysically high electron acceleration rates and energies for the 20–30 % events where the spectral index changes slowly as the flux rises, thus showing less prominent soft-hard-soft behavior (Fig. 3.4). This is due to the fact that the models need a very low threshold energy ϵ_* (that is, the energy above which electrons are accelerated, corresponding approximately to the energy of the pivot point) to account for low rates of change of the spectral index. A low value for ϵ_* enables the model to provide reasonably good fits to the data, but will often lie outside the range of validity of the models studied. For instance, the stochastic acceleration model will break down for electron energies comparable to the thermal energy of the medium in which the electrons are accelerated, since the interaction of the accelerating waves with the thermal component was not considered for this simple model. The assumption of a fixed ϵ_* during a peak may also be challenged. Allowing ϵ_* to change during the observed events could reduce the excess acceleration rate values.

The quantitative relation between the observed spectral index and the normalization of the spectrum exploited here has the advantage that it does not depend explicitly on the time evolution of the two variables. Therefore it is comparatively easier to compare with model predictions than the full-fledged time evolution of the spectrum. The $\delta \leftrightarrow \Phi$ relation puts an additional requirement on the acceleration mechanism.

The comparison between observations and models proposed here can be done with real data in a straightforward way, and it does provide interesting results for relatively simple theoretical models: a majority of flare peaks (about 77 % of the rise and decay phases) can be well fitted by these simple models within a compact region of parameter space. Nevertheless, the rest (outliers with unphysical model parameters) point to the fact that more degrees of freedom are necessary for interpretation. While there is a wealth of data available thanks to the RHESSI mission, we lack concrete predictions by more complex acceleration models on the behavior of the spectral index during flares. Therefore, Chapter 4 presents predictions for the spectral evolution from a more modern stochastic acceleration model, finding a soft-hard-soft behavior with the presence of a pivot point.

Chapter 4

Stochastic Acceleration Modeling

*Theories should be as simple
as possible, but not simpler*

Albert Einstein (1879 - 1955)

ABSTRACT:

Context. Stochastic acceleration is thought to be a key mechanism in the energization of solar flare electrons.

Aims. We study whether stochastic acceleration can reproduce the observed soft-hard-soft evolution of the spectral features of the hard X-ray emitted by suprathermal electrons. We pay special attention to the effects of particle trapping and escape.

Methods. The Fokker-Planck equation for the electron distribution is integrated numerically using the coefficients derived by Miller et al. for transit-time damping acceleration. The electron spectra are then converted to photon spectra for comparison with RHESSI observations of looptop sources.

Results. The presence of particle escape softens the model spectra computed in the stochastic acceleration framework. The ratio between the efficiency of trapping and acceleration controls the spectral evolution which follows a soft-hard-soft pattern. Furthermore, a *pivot point* (that is, a common crossing point of the accelerated particle spectra at different times) is found at around 10 keV. It can be brought into agreement with the observed value of 20 keV by enhanced trapping through an electric potential.

Conclusions. The model proposed here accounts for the key features observed in the spectral evolution of hard X-ray emission from looptop sources.

4.1 Introduction

Solar flares emit large amounts of continuum hard X-ray bremsstrahlung from energetic electrons up to several hundreds of keV. The thermal energy of the ambient electrons in the corona is substantially lower, with electron temperatures observed up to 6 MK in nonflaring active regions (Brosius et al. 1996, Benz & Grigis 2002). Clearly, a mechanism is needed to accelerate the electrons out of the thermal distribution up to relativistic energies. More than 10^{31} erg (Lin et al. 2003, Emslie et al. 2004, Kane et al. 2005) of energy can be transferred into non-thermal electrons during a major solar flare over a period of a few hundred seconds.

These numbers set stringent requirements to acceleration models, and it is by no means a simple task to identify the physical processes involved. Most of the proposed models fall into three broad classes: electric DC field acceleration, stochastic acceleration and shock acceleration (see e.g. the review by Aschwanden 2002).

Miller et al. (1996, hereafter MLM) proposed a stochastic acceleration mechanism where electrons are energized by small amplitude turbulent fast-mode waves, the transit-time damping model. MLM showed that their model could successfully account for the observed number and energy of electrons accelerated above 20 keV in subsecond spikes or energy release fragments in impulsive solar flares. However, they made no attempt to explain the observed hard X-ray spectra (which are softer than predicted by the transit-time damping model) and did not consider spectral evolution. The MLM approach does not account for escape and transport processes.

What is the effect of escape on the electron spectrum in the accelerator? In stochastic acceleration, each electron describes a random walk in energy space. The effect of escape is to shorten the dwell time of the particles in the accelerator, and therefore it limits the average energy of the electrons. This results in a softer spectrum. Therefore, we need to take in account escape to compare quantitatively the model predictions with hard X-ray observations. Furthermore, transport effects account for the modification of the electron spectrum from the time they leave the accelerator until they reach the hard X-ray emitting regions. The usual interpretation is that the particles are accelerated near the top of magnetic loops, but most of the X-rays are emitted in the loop footpoints, where the density is much larger. Nevertheless, looptop sources are also observed (Masuda et al. 1994).

Observations from the Reuven Ramaty High Energy Imaging Spectrometer (RHESSI, Lin et al. 2002) deliver hard X-ray spectra of both footpoint and looptop sources (Emslie et al. 2003, Liu et al. 2004). Looptop sources are better suited for comparison with accelerator models than footpoint sources, since one does not need to take into account the spatial transport from the ac-

Table 4.1: Observational constraints for looptop sources (taken from Battaglia & Benz 2006).

Parameter	Description	Average	Range
Pivot-point energy	ε_*	20 keV	16–24 keV
Pivot-point flux ^a	J_*	2	1–4
Mean temperature		22	18–25 MK
Nonthermal fitting range:			
Lower energy	ε_{\min}	25 keV	20–30 keV
Upper energy	ε_{\max}	60 keV	40–80 keV

^a In units of photons $\text{cm}^{-2} \text{s}^{-1} \text{keV}^{-1}$.

celerator. The emission from the modeled electron distribution can be directly compared with the observed spectra of the looptop source.

Battaglia & Benz (2006) present a careful and comprehensive study of the spectral evolution of looptop and footpoint sources for 5 well observed RHESSI flares. They find that looptop sources systematically show the soft-hard-soft (SHS) behavior observed spectroscopically for the total flare emission (Chapter 2 and references therein). On the other hand, some footpoint sources do not follow the SHS pattern. These observations suggest that the SHS behavior is a property of the acceleration process.

The observed SHS behavior manifests itself as a tight correlation between the curves describing the time evolution of the negative spectral index γ and the normalization J_{E_0} of the non-thermal power-law component of the photon spectra, measured at a fixed reference energy E_0 . RHESSI observations show a linear relation between γ and $\log J_{E_0}$ (Chapter 2). This is equivalent (Chapter 3) to the presence of a *pivot point*, that is, a common point where the power-law component of the photon spectra observed at different times intersect. Therefore, the position of the pivot point can be found observationally by fitting the regression line to γ and $\log J_{E_0}$. Since the observations show that during the impulsive phase of most flares the scatter around such a model is relatively small, such fittings provide us with two new meaningful observational parameters which can be used for comparison with theories. The best-fit pivot-point energy can be measured by RHESSI with an accuracy of 10–20% (Battaglia & Benz 2006).

The measured energies of the pivot points lie in the range of 18–24 keV for looptop sources and 13–15 keV for footpoint sources. In Table 4.1 we summarize the observational results from Battaglia & Benz (2006) which we will use to constrain the transit-time damping acceleration model.

In this Chapter we study how well the transit-time damping model endowed with an escape mechanism can account for the hard X-ray spectra of

the looptop sources seen by RHESSI and, in particular, for their spectral evolution. We investigate whether the spectrum of the photons emitted by the modeled electrons in the accelerator shows SHS behavior and how well this quantitatively agrees with the observations.

We proceed as follows: a modified version of the MLM model with a better characterization of electron trapping is presented in Sect. 4.3. The evolution of the electron energy distribution function is given by a diffusion equation which is integrated numerically and transformed into photon spectra. In Sect. 4.4 we present the resulting photon spectra and compare their behavior with the observations. The results are discussed in Sect. 4.5 and conclusions are drawn in Sect. 4.6.

4.2 Pivot-Point Theory

In this section the mathematical foundations needed for the comparison of the model results with the observations are presented. In particular we explain what are the consequences of the correlation in time between flux and spectral index. By the introduction of a new parameter, the pivot point, the time dependence can be eliminated, thus simplifying the analysis.

The theory is presented in a general context, and can be applied to any kind of spectra (for example, photons or electrons) described by a power-law in some energy range. The starting point of this analysis is the presence of a correlation between the logarithm of the flux, $\log F_{E_0}$, measured at energy E_0 and the spectral index δ , where the time dependent spectrum is given by

$$F(E, t) = F_{E_0}(t) \left(\frac{E}{E_0} \right)^{-\delta(t)}, \quad (4.1)$$

for t in a time interval T_{INT} (for instance, the duration of a flare emission peak). Panel (a) of Fig. 4.1 shows the ideal case where the correlation in time between δ (lower curve) and $\log F_{E_0}$ (upper curve) is perfect: the two curves are parallel. In such a case, a plot of δ vs. $\log F_{E_0}$ is linear. This is shown in panel (c). The relation between these two parameters can be expressed as

$$\delta(t) = a \cdot \log F_{E_0}(t) + b, \quad (4.2)$$

where $a \neq 0$, and the parameters a and b do not depend on time.

Some points with selected values of δ are marked by special symbols in Fig. 4.1: circles for $\delta = 2$, triangles for $\delta = 4$, squares for $\delta = 6$ and stars for $\delta = 8$. In panel (b) the spectra corresponding to these values of the spectral index are plotted together. It is evident that all these spectra intersect in a common point, the *pivot point*. The coordinates of the pivot point are defined as (E_*, F_*) . The presence of a linear relation between $\delta(t)$ and $\log F_{E_0}(t)$ is equivalent to the presence of a pivot point. This means that panel (a) in Fig. 4.1 implies both (b) and (c). A detailed proof follows.

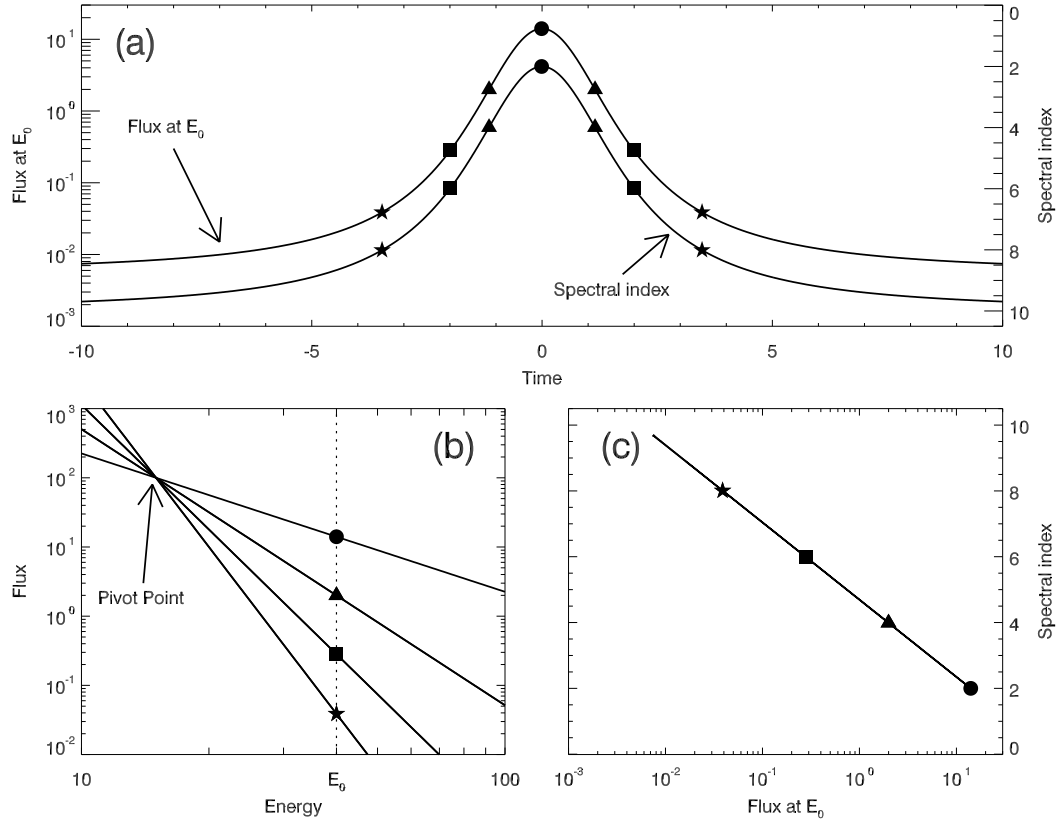


Figure 4.1: Schematic illustration of the basic properties of a spectral evolution. *Panel (a)*: time evolution of the logarithm of the flux measured at reference energy E_0 (upper curve) and of the spectral index (lower curve) in the case where they are perfectly correlated. *Panel (b)*: Spectra for different values of the spectral index, crossing at the pivot point. *Panel (c)*: Linear dependence of the spectral index on the logarithm of the flux. In all panels, the stars, squares, triangles and circles mark points with spectral indices of, respectively, 8, 6, 4 and 2.

4.2.1 Proof of the Equivalence between Pivot Point and Correlation of δ with $\log F$

The following statements are equivalent:

- (i) There is an $E_* \neq E_0$ such that $F(E_*, t_1) = F(E_*, t_2) =: F_*$ for all $t_1, t_2 \in T_{\text{INT}}$.
- (ii) There exist constants $a \neq 0$ and b such that

$$\delta(t) = a \log F_{E_0}(t) + b \quad (4.3)$$

for all $t \in T_{\text{INT}}$.

The parameters a and b are given by

$$a = \frac{1}{\log(E_*/E_0)}, \quad (4.4)$$

$$b = \frac{-\log F_*}{\log(E_*/E_0)}. \quad (4.5)$$

We give first the proof that (i) \implies (ii).

Because $F(E_*, t) = F_*$ for all $t \in T_{\text{INT}}$, Eq. (4.1) yields

$$\log F_* = \log \left[F_{E_0} \left(\frac{E_*}{E_0} \right)^{-\delta} \right] = \log F_{E_0} - \delta \log(E_*/E_0) \quad (4.6)$$

which can be solved for δ , yielding

$$\delta = \frac{\log F_{E_0}}{\log(E_*/E_0)} - \frac{\log F_*}{\log(E_*/E_0)} \quad (4.7)$$

$$= a \log F_{E_0} + b, \quad (4.8)$$

where $a \neq 0$ for finite values of E_*, E_0 .

Now we prove (ii) \implies (i).

Let us define $E_* = E_0 \exp(1/a) \neq E_0$. Then using Eqs. (4.1), (4.4) and (4.3) we get

$$\log F(E_*) = \log F_{E_0} - \delta \cdot \log \left(\frac{E_*}{E_0} \right) \quad (4.9)$$

$$= \log F_{E_0} - \frac{\delta}{a} \quad (4.10)$$

$$= -\frac{b}{a}, \quad (4.11)$$

which does not depend on δ or F_{E_0} . Therefore, (E_*, F_*) are the coordinates of the pivot point. Q.E.D.

4.2.2 Implications

We have established above formally the equivalence between the presence of a pivot point and the linear relation between the spectral index and the logarithm of the flux measured at some fixed energy. We note that the shape of the curves describing the time evolution of δ and F_{E_0} does not influence the results described above. The time dependence can be eliminated: this simplifies the analysis and allows the new parameter, the pivot-point position, to be used in the comparison of observations with theoretical models. Conversely, if the observation show that δ and $\log F_{E_0}$ do not correlate well in time, we will not find any pivot-point like behavior in the spectral evolution.

Our derivation assumes that the spectra are represented by power-laws at all energies. In this case, at energies lower than the pivot-point energy, the linear relation between flux and spectral index changes sign and higher fluxes would correspond to steeper spectra instead of harder ones. However, the observed spectra are not given by power-laws at low energies, because steep spectra are not integrable and therefore would imply an infinite number of particles, which is not physically possible. Therefore a deviation from the power-law form is expected in the form of a turnover at low energies (Saint-Hilaire & Benz 2005, Sui et al. 2005). This means that it is well possible that the spectra do not extend all the way to the pivot-point energy, even if a correlation between the spectral index and the flux is observed at higher energies. In such a situation the pivot point is *virtual*, in the sense that its flux is higher than the spectral flux at the same energy. In this case the analysis given above retain its validity, but the spectra used should be understood as the power-law extensions of the physical spectra. Such a situation is represented in Fig. 4.2.

We emphasize that the presence of a pivot point is a *local* property of a family of curves at energy E_0 , in the sense that it can be seen as a convergence point for the tangents in E_0 to the family of curves (in logarithmic space). For power-law functions, the coordinates of the pivot point are independent of the energy E_0 , because their logarithmic derivative is constant as a function of energy. Other functions exist for which there is a different pivot point for each value of E_0 .

For the sake of completeness, we report here the differential equation whose general solution is the family of curves yielding a pivot point (in the sense of a convergence point for the tangents in linear space) in $x^*(x), y^*(x)$:

$$\frac{dy}{dx} + \frac{y}{x^*(x) - x} = \frac{y^*(x)}{x^*(x) - x}, \quad (4.12)$$

where in our case, $x = \log E$, $x^* = \log E^*$, $y = \log F$ and $y^* = \log F^*$.

In the special case $x^* = \text{const.}$ and $y^* = \text{const.}$ (that is, a unique pivot point for all energies), the general solution of Eq. (4.12) is given by the equation $y - y^* = m \cdot (x - x^*)$, which describes the family of all straight lines intersecting at x^* and y^* .

4.3 The Model

The transit-time damping model is described in great detail by MLM. Here we first summarize the important features of the model presented by MLM, and then describe our modification of the model.

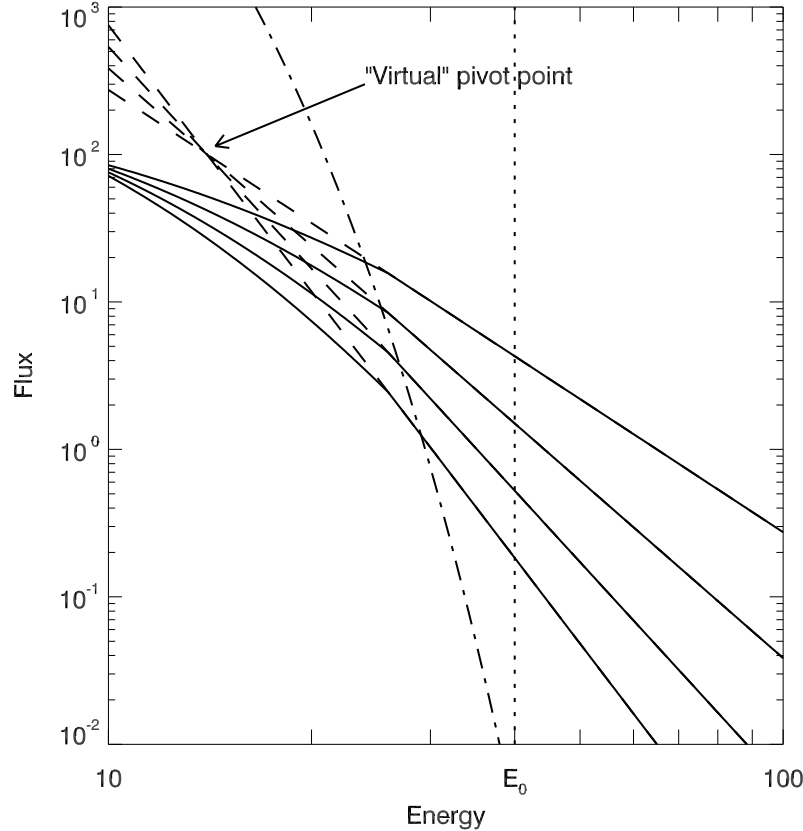


Figure 4.2: Spectra (mock data, continuous lines) turning over at low energy. The power-law extensions of the spectra (dashed lines) intersect in a *virtual* pivot point, with larger flux than the one from the spectra. The dashed-dotted line represent an additional thermal component, effectively hiding the spectral behavior at low energies.

4.3.1 The Transit-Time Damping Model

The source of the flare energy is an event of magnetic reconnection, where magnetic field energy is transferred, by an unspecified mechanism, into small-amplitude magnetoacoustic fast mode waves. These waves have very large wavelengths, comparable with the length scale of the global magnetic field restructuring induced by the reconnection process.

A cascading process then takes place, producing waves with larger wave vector k and isotropic distribution. This process transfers wave energy density from the low k into the large k waves. The electrons interact with the parallel component of the magnetic field of the large k waves. An electron of velocity v can efficiently exchange energy with the waves if the resonance condition

$k_{\parallel}v_{\parallel} = \omega = kv_A$ is satisfied, where the subscript \parallel denotes the component parallel to the ambient magnetic field, ω is the wave frequency and v_A is the Alfvén speed. The same condition can also be expressed as $\mu\eta v = v_A$, where μ and η are the cosines of the angle between the ambient magnetic field and the direction of propagation of the electrons and the waves, respectively. From this form of the equation it is clear that only electrons faster than v_A can be accelerated by this mechanism. The perpendicular velocity v_{\perp} is not affected by these interactions.

Since the acceleration only occurs in the direction of the ambient magnetic field, the electron distribution becomes strongly elongated in parallel direction in the absence of pitch-angle scattering. This reduces considerably the efficiency of transit-time damping acceleration, because for fast particle with $v \gg v_A$ and $|\mu| \approx 1$ the resonance condition can only be satisfied by waves with $|\eta| < v_A/v$, which represent only a small fraction of all the available phase space. The acceleration efficiency can therefore be increased by the presence of a mechanism which isotropizes the electron distribution, allowing particles with small $|\mu|$ to interact with waves with $|\eta| > v_A/v$. MLM assume that an isotropization mechanism is present, but do not address the details of the process.

The model described by MLM is self consistent in the sense that it describes the evolution in time of both the electrons (which are accelerated) and the waves (which are damped). The efficiency of the electron acceleration by the waves is determined by the total energy density of the waves U_T and by the shape of the wave spectrum: large k waves exchange energy with the electrons faster because the transit time between the magnetic perturbations gets shorter. The coefficients describing the diffusion of the electrons in energy space depend on the product of U_T and $\langle k \rangle$, where the latter represents the average wave-vector of the waves.

The evolution of the electrons is described by the Fokker-Planck equation for the electron distribution in energy space. MLM consider the effects of the acceleration by the waves and of collisions with the ambient plasma.

4.3.2 Transit-Time Damping and Escape

In this Chapter, we study the electron and photon spectra produced by a simplified transit-time damping acceleration model. We do not address here the problem of the time it takes for the accelerated electron distribution to reach equilibrium, considering that MLM have established this time to be sufficiently short. Therefore we need not to account explicitly for the MHD cascading process, but we will instead keep $U_T \cdot \langle k \rangle$ as a free parameter of our model. This means that only one partial differential equation describes the time-evolution of the system instead of a set of two coupled equations.

Table 4.2: Description of the parameters used in the model.

Param.	Description	Default value
B	Ambient magnetic field strength	500 G
n	electron density	10^{10} cm^{-3}
T	Ambient plasma temperature	10 MK
$\log \Lambda$	Coulomb logarithm	18
Ω_{H}	Proton gyrofrequency	4.78 MHz
T_{H}	Time unit Ω_{H}^{-1}	$2.09 \cdot 10^{-7} \text{ s}$
v_{A}	Alfvén speed	$0.034c$
U_{T}	Energy density of the accelerating waves	2 erg cm^{-3}
U_{B}	Energy density of the ambient field ($\frac{1}{8}B^2/\pi$)	10^4 erg cm^{-3}
$\langle k \rangle$	Average wavenumber of the turbulence	$4.8 \cdot 10^{-4} \text{ cm}^{-1}$
I_{ACC}	Acceleration parameter: $I_{\text{ACC}} = \frac{U_{\text{T}}}{U_{\text{B}}} \cdot \frac{c\langle k \rangle}{\Omega_{\text{H}}}$	(free)
τ	Escape time	(free)

A short description of the physical parameters upon which the model depends is given in Table 4.2, where a default reference value for each parameter is listed. In the following these default values will be implied if different values are not explicitly mentioned.

The transit-time damping acceleration model describes the evolution of the electron population in energy and time. We denote by $N(E) dE$ the number of electrons per cubic centimeter with energy in the interval dE around E , where E is the dimensionless particle energy in units of $m_e c^2$. The total electron density is $n = \int_0^\infty N(E) dE$. The evolution in time of the distribution function $N(E, t)$ is given by the convective-diffusive equation

$$\frac{\partial N}{\partial t} = \frac{1}{2} \frac{\partial^2}{\partial E^2} [(D_{\text{COLL}} + D_{\text{T}}) N] - \frac{\partial}{\partial E} [(A_{\text{COLL}} + A_{\text{T}}) N] - S(E) \cdot N + Q(E). \quad (4.13)$$

It is shown in Appendix A how this form is computed from the diffusion equation in momentum space.

The coefficients D_{T} and A_{T} describe the diffusion and convection in energy space due to the interaction of the electrons with the waves. The coefficients D_{COLL} and A_{COLL} represent the effect that collisions against the ambient plasma have on the distribution function. We include the effects of the escape

by a sink term $S(E)$ and a source term $Q(E)$ described below.

The acceleration coefficients are given by MLM, and we report them here written in dimensionless form:

$$A_{\text{T}}(E) = \frac{\pi}{4} \beta_{\text{A}}^2 I_{\text{ACC}} \gamma \beta g(\beta) \quad (4.14)$$

$$D_{\text{T}}(E) = \frac{\pi}{8} \beta_{\text{A}}^2 I_{\text{ACC}} \gamma^2 \beta^3 f(\beta) \quad (4.15)$$

where

$$\gamma = 1 + E, \quad \beta = \sqrt{1 - \gamma^{-2}}, \quad \xi = \frac{\beta_{\text{A}}}{\beta} \quad (4.16)$$

$$f(\beta) = -1.25 - (1 + 2\xi^2) \log \xi + \xi^2 + 0.25\xi^4 \quad (4.17)$$

$$g(\beta) = \frac{1}{4\gamma^2} (4\xi^2 \log \xi - \xi^4 + 1) + f(\beta) \quad (4.18)$$

The acceleration coefficients vanish for $E < E_{\text{A}}$, where E_{A} is the kinetic energy of a particle with speed $\beta_{\text{A}} = v_{\text{A}}/c$, because the resonance condition cannot be satisfied below the Alfvén speed.

The coefficients for Coulomb collisions of the accelerated particles with the thermal background population (Spitzer 1962, Trubnikov 1965) are given by :

$$A_{\text{COLL}} = -\nu n [\psi(x) - \psi'(x)] E^{-1/2} \quad (4.19)$$

$$D_{\text{COLL}} = 2\nu n \frac{\psi(x)}{x} E^{1/2} \quad (4.20)$$

with

$$x = \frac{m_e c^2 E}{k_{\text{B}} T}, \quad \nu = \frac{\sqrt{8} \pi e^4 \log \Lambda T_{\text{H}}}{m_e^2 c^3} \quad (4.21)$$

$$\psi(x) = 2\pi^{-1/2} \int_0^x \sqrt{t} e^{-t} dt. \quad (4.22)$$

The energy dependence of the acceleration and collisional coefficients is shown in Fig. 4.3.

The sink term is given by:

$$S(E) = \frac{T_{\text{H}} \beta}{\tau}, \quad (4.23)$$

where τ is the escape time. This represents a purely kinematic escape for a spatially homogeneous electron distribution (leaky-box escape). We can understand this term in the following way: let's assume that the plasma is contained in a cylinder with length L and cross section A , having a spatially homogeneous electron density n with a total number of particles $N_{\text{TOT}} = \int n dV = n \cdot L \cdot A$ all having the same speed v . After a time interval dt , the

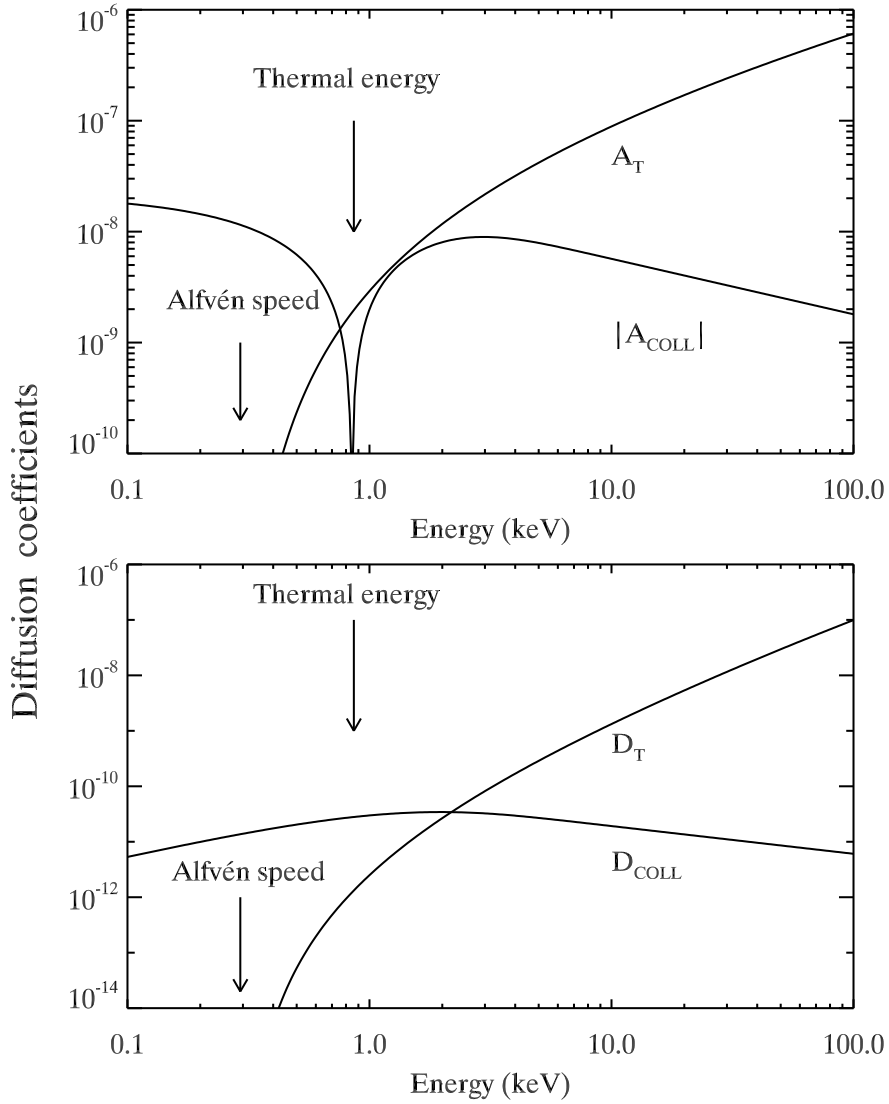


Figure 4.3: Upper panel: the absolute value of the dimensionless Coulomb (subscript COLL) and transit-time damping (subscript T) convection coefficients. Lower panel: the dimensionless Coulomb and transit-time damping diffusion coefficients. The arrows mark the thermal energy of the electrons in the plasma and the kinetic energy of electrons moving with the Alfvén speed v_A .

number of particles which have escaped the cylinder (assuming free streaming without collisions) is $dN_{\text{TOT}} = n \cdot v \cdot A \cdot dt$. The rate of change of the density is $dn/dt = n \cdot v/L$. Defining the escape time $\tau = L/c$ yields Eq. (4.23), where the factor $T_{\text{H}} = \Omega_{\text{H}}^{-1}$ comes from the transformation of the equation into dimensionless form.

In a more general case, where collisions have an effect, the particles can-

not stream freely out of the accelerator, and they will need a longer time to escape. In this case, the escape time τ can be larger than L/c and the energy dependence on the collision frequencies will cause τ to vary with the energy. Since we do not address here the physical details of the escape we will assume for now that $\tau(E)$ is constant for all energies.

Under the influence of collisions, we are not allowed to use L as the length of the path traversed by a particle before it can leave the accelerator: $L(E) = c\tau(E)$ denotes the effective length for particle escape. It is best to think of the escape time τ as a general parameter describing the strength of the particle trapping in the accelerator: the trapping becomes the more efficient, the larger τ .

The source term $Q(E)$ is needed to keep the number of particles in the accelerator constant. Physically, these are electrons supplied by a return current, needed to keep electrically neutral the region where the electrons are accelerated. We assume that the electrons supplied by the return current mechanism are “cool” in the sense that their distribution is comparable with a thermal spectrum and with the temperature of the ambient plasma. Therefore we have

$$Q = \dot{n}_0 \cdot N_{\text{MB}}(E), \quad (4.24)$$

where

$$N_{\text{MB}}(E) = 2\pi^{-1/2}(k_{\text{B}}T)^{-3/2}\sqrt{E}e^{-E/(k_{\text{B}}T)} \quad (4.25)$$

is the Maxwell-Boltzmann distribution normalized to unity, and $\dot{n}_0 = \int SN dE$ is the rate of escaping particles.

4.3.3 Method of Solution

Equation (4.13) is solved numerically using the Crank-Nicolson finite differences scheme in logarithmic energy space, which is well suited for diffusion problems. This method is the same as used in MLM and gives accurate results with fixed steps in time and $\log E$.

4.3.4 From Electrons to Photons

The numerical solution described above yields electron spectra. For a meaningful comparison with the observations we need photon spectra. They are generated by bremsstrahlung from the electron distribution. Since the model spectra are in equilibrium (particle losses by escape and coulomb collisions are compensated by the acceleration) a *thin-target* emission is computed.

We convert the energy differential electron flux distribution $F(E)$ in electrons $\text{cm}^{-2} \text{s}^{-1} (mc^2)^{-1}$ into the photon spectrum $J(\varepsilon)$ observed at Earth

in photons $\text{cm}^{-2} \text{s}^{-1} (mc^2)^{-1}$ using the equation for the thin-target bremsstrahlung emission:

$$J(\varepsilon) d\varepsilon = \frac{nV}{4\pi R^2} \int_{\varepsilon}^{\infty} N(E) d\sigma(\varepsilon, E) dE, \quad (4.26)$$

where V is the source volume and R is the distance from the Sun. The cross section $d\sigma(\varepsilon, E)$ used is the fully relativistic, spatially integrated Bethe-Heitler formula (Bethe & Heitler 1934) without further approximations. This should adequately represent the emission process of the computed electron spectrum in a looptop source.

We will consistently use the notation δ , γ , F_{E_0} , J_{ε_0} , E_* , ε_* , F_* and J_* for, respectively, the electron spectral index, the photon spectral index, the electron density at energy E_0 , the photon flux at energy ε_0 , the electron pivot-point energy, the photon pivot-point energy, the electron density at E_* and the photon flux at ε_* .

4.4 Results

Section 4.4.1 presents the detailed properties of the numerical solution of Eq. (4.13) for the standard set of parameters (“default values” given in Table 4.2) and the energy independent escape model. In a second step (Sect. 4.4.2) we will proceed to study the dependence of the results on the values of the model parameter and, finally, examine an alternative escape model (Sect. 4.4.3).

4.4.1 Results for the Default Values of the Model Parameters

In this section the default values for the model parameters presented in Table 4.2 are used. In this case, τ and I_{ACC} are the only free parameters of the model, and the acceleration coefficients are much larger than the Coulomb collisional coefficients in the energy range above 10 keV (see Fig. 4.3). Therefore, we expect that the electron spectrum in this energy range depends only on the value of the product $I_{\tau} = I_{\text{ACC}} \cdot \tau$ (cf. Eq. 4.13), and we can basically work with one free parameter. For some choices of the model parameters, this approximation will not be valid anymore, so we will relax this assumption in Sect. 4.4.2.

Figure 4.4 presents the electron spectra resulting from the numerical solution of Eq. (4.13) for 4 different values of I_{τ} , which yield different values of the electron spectral index δ fitted in the energy range 30–80 keV. The harder spectra are the ones resulting from a higher value of I_{τ} . The dependence of the spectral index on I_{τ} is shown in the top panel of Fig. 4.5. Note that in

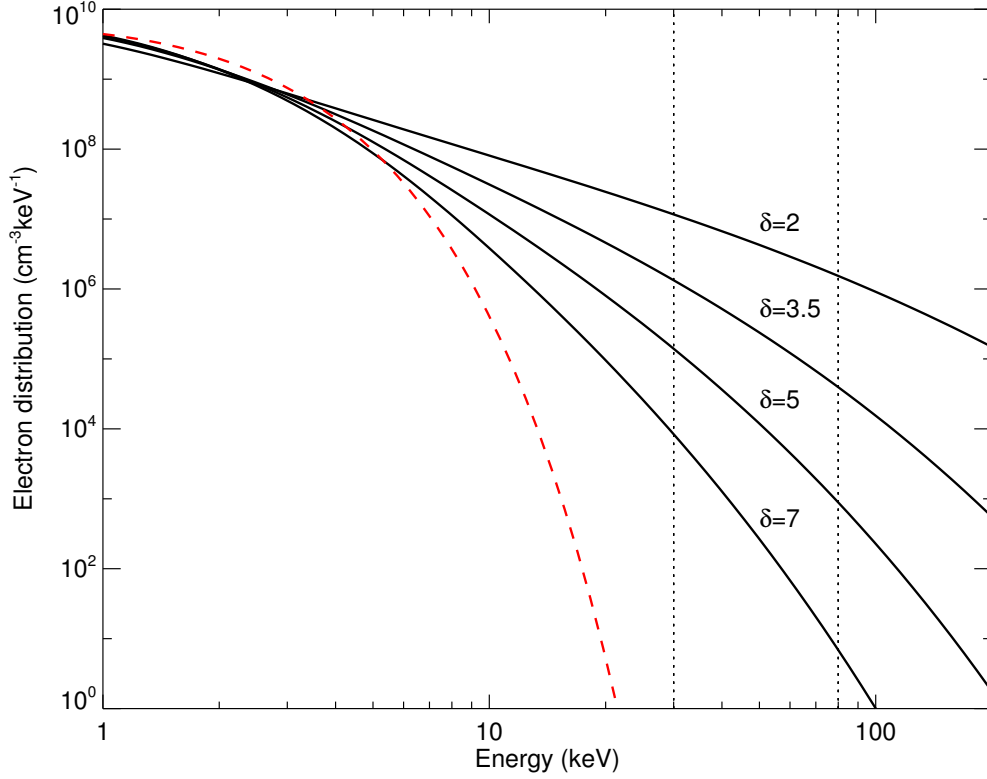


Figure 4.4: Accelerated electron distributions with different values of the power-law index resulting from changes in $I_\tau = I_{\text{ACC}} \cdot \tau$. The dashed curve represents the ambient Maxwellian distribution. The two dotted lines indicate the energy range used for the computation of the power-law index δ shown above each spectrum.

the case where acceleration is weak or escape strong (that is, I_τ is small) very soft spectra are produced. For increasing trapping and acceleration efficiency (I_τ larger) the spectra become harder. The middle panel of Fig. 4.5 shows the dependency of the electron flux at 50 keV, F_{50} , on I_τ . Here the flux is larger for larger I_τ . During a flare, I_τ will change as more energy is injected into turbulence waves, and therefore both δ and F_{50} will change. This explains qualitatively the soft-hard-soft effect: as I_τ increases, δ will decrease and F_{50} will increase. It is shown in the bottom panel of Fig. 4.5, where δ vs. F_{50} are plotted as a function of the parameter I_τ .

Since I_τ contains the physics of acceleration and escape, the time evolution of the spectral index and flux in our model is a direct consequence of the changes in I_τ . For example, if the energy density of the turbulent waves grows, reach a maximum value and then decreases, the electron spectrum will harden until peak time and soften again.

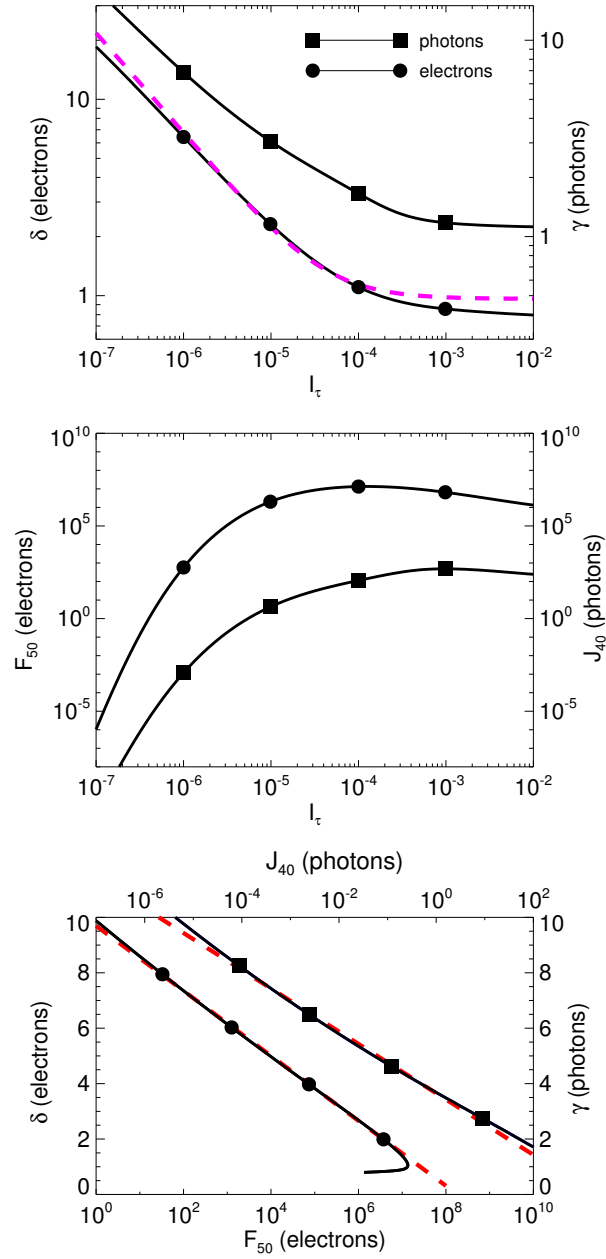


Figure 4.5: *Top:* The electron spectral index δ (measured in the energy range 30–80 keV) and the photon spectral index γ (measured in the energy range 30–50 keV) plotted against I_τ . The dashed line represent the approximated analytical solution computed in App. B. *Middle:* The electron density at 50 keV F_{50} and photon flux at 40 keV J_{40} plotted against I_τ . *Bottom:* δ vs. F_{50} and γ vs. J_{40} plotted parametrically as a function of I_τ . The dashed line are the best log-lin fit for δ in the range 2–8 and for γ in the range 3–9.

To check the quality of the numerical solution, we obtain an approximated analytical expression for the function $\delta(I_\tau)$, whose computation is explained in Appendix B. The approximate curve is plotted in the top panel of Fig. 4.5 as a dashed line and agrees well with the numerical solution. Because of the linear nature of Eq. (4.13), the method exploited in App. B cannot be used to get an approximate solution for $F_{50}(I_\tau)$.

The dashed line in the bottom panel of Fig. 4.5 represents the best fit of a logarithmic function (linear in log-lin space) to the data for δ in the range 2–8. Such a relation between the electron flux at a reference energy and the spectral index indicates the presence of a pivot point in the electron spectra, as shown in section 4.2. From the slope and normalization of the dashed line we can get values of the pivot-point energy E_* and flux F_* for the electron distributions.

More precisely, if

$$\delta = a \log F_{E_0} + b, \quad (4.27)$$

then

$$E_* = E_0 e^{1/a} \quad \text{and} \quad F_* = e^{-b/a} \quad (4.28)$$

as follows from Eq. (4.4). The dashed line in Fig. 4.5, bottom, corresponds to $E_* = 7.65$ keV and $F_* = 2 \cdot 10^8$ electrons $\text{cm}^{-3} \text{keV}^{-1}$.

For a meaningful comparison of these results with the observations, a value for the pivot point of the *photon spectra* is needed. J_* and ε_* can be computed by fitting the regression line of γ vs. $\log J_{\varepsilon_0}$, in the same way as E_* and F_* . Note that while J_* depends on the source volume, ε_* can be immediately compared with the observations. Using the photon spectral index computed in the energy range 30–50 keV, the regression (restricting γ to the range 3–9) yields the pivot-point coordinates $\varepsilon_* = 5.0$ keV and $J_* = 1.9 \cdot 10^3 \cdot V_{27}$ photons $\text{cm}^{-2} \text{s}^{-1} \text{keV}^{-1}$, where V_{27} is the volume of the source in units of 10^{27}cm^3 .

The above value of the pivot-point energy is too low compared to the looptop source observations by Battaglia & Benz (2006) summarized in Table 4.1, reporting $\varepsilon_* \approx 20$ keV. This means that if the photon spectral index of our model varies from, say, 3 to 6, the non-thermal flux is subjected to an excursion which is too large to account for the observed behavior of the spectrum in solar flares.

Two possible solutions of this problem exist: we can explore the parameter space to find out if there is some combination of the parameter values which indeed produces a higher pivot-point energy ε_* , or we can try to modify the escape term.

4.4.2 Exploration of the Parameter Space

The set of default parameters used in the previous section yields a pivot-point energy ε_* which is lower than the observed value. However, the pivot-

point energy depends on model parameters like T , n etc. Therefore a better coverage of parameter space than the example reported above is needed to assess the range of variability of ε_* . The pivot-point energy depends on the temperature of the ambient plasma T , its electron density n and its magnetic field strength B_0 (indirectly, through the Alfvén speed). We therefore compute the equilibrium solutions of Eq. (4.13) for a large number of combinations of different values of these parameters, each set yielding a value for ε_* . In this way we sample the function $\varepsilon_*(T, n, \dots)$.

There is however a complication: for some choices of the parameters, the approximation that the spectral index and flux depend only on $I_\tau = \tau \cdot I_{\text{ACC}}$ will not be valid anymore. This approximation becomes invalid if $A_{\text{COLL}}/A_{\text{T}}$ or $D_{\text{COLL}}/D_{\text{T}}$ approach unity. We note that both ratios are roughly proportional to n^2 at high energies, and therefore the approximation becomes bad for large values of the density. In this case, the escape time τ and the acceleration parameter I_{ACC} separately influence the spectral index and flux, and the pivot-point energy will depend on the τ vs. I_{ACC} relation. Since we have not modeled the physical mechanism responsible for the trapping of particles, the details of how τ depends on I_{ACC} are not known.

We estimate the range of pivot points by choosing several representative paths in the τ, I_{ACC} -plane (as shown in Fig. 4.6) and computing the pivot-point coordinates resulting from spectra computed along these paths.

Recalling that in first approximation the spectral index depends only on the product $I_\tau = I_{\text{ACC}} \cdot \tau$, the paths are required to start from a point on the line $\tau \cdot I_{\text{ACC}} = 10^{-7}$ and end in a point on the line $\tau \cdot I_{\text{ACC}} = 10^{-4}$. The region between these two delimitation lines is shown in gray in Fig. 4.6. These limits are chosen to ensure that the computed photon spectral indices fall into the observed range. For the standard values of the parameters, the region above the gray area yields spectral indices harder than about 1.5 and the region below yields γ softer than about 15.

There are however more constraints on the values of I_{ACC} . This parameter is the product of the dimensionless wave number and the energy density in the turbulent fast mode waves. In our simplified version of transit-time damping acceleration, the time evolution of the spectral energy distribution of the waves is not computed. Therefore we set the maximum value of I_{ACC} at $I_{\text{ACC}}^{\text{MAX}} = 6 \cdot 10^{-4}$. It is the maximum value that is obtained by MLM during the cascading process (read from the plot in Fig. 6b in MLM). Since I_{ACC} controls the acceleration efficiency, values which are much smaller than $I_{\text{ACC}}^{\text{MAX}}$ yield a weak and slow acceleration, contrary to the observations. Larger values of I_{ACC} could result from a higher energy density in the waves, but in that regime the wave amplitude becomes so large that nonlinear effects are likely to lead to a breakdown of the physical model used by MLM to compute the acceleration coefficients. Thus values of I_{ACC} much larger than $I_{\text{ACC}}^{\text{MAX}}$ do not necessarily improve the acceleration efficiency.

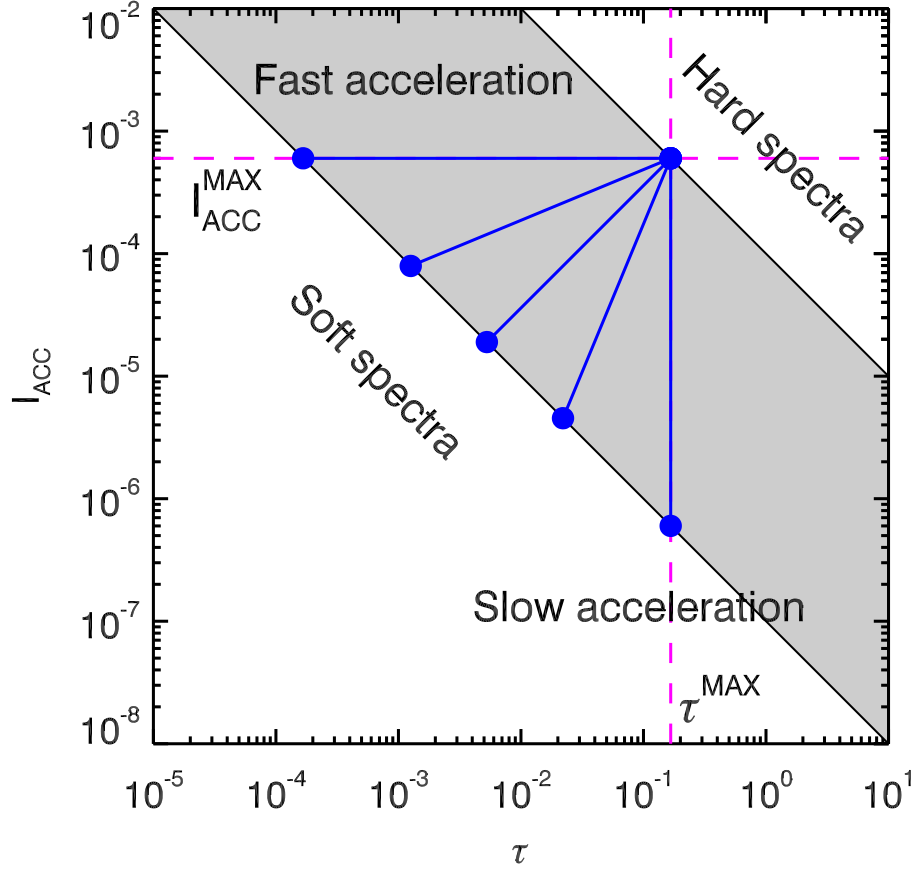


Figure 4.6: Five paths (between filled circles) in the τ, I_{ACC} -plane as described by Eq. (4.29), corresponding to $\arctan \alpha = 0, \pi/4, \pi/2, 3\pi/4, \pi/2$. The gray shaded region contains the points yielding photon spectra with a spectral index lying approximately in the 1.5–15 range. The two dashed lines have abscissa and ordinate of τ^{MAX} and $I_{\text{ACC}}^{\text{MAX}}$, respectively.

For these reasons we additionally require that all the paths end on the point $(\tau^{\text{MAX}}, I_{\text{ACC}}^{\text{MAX}})$, where τ^{MAX} is the point on the upper delimitation line with ordinate $I_{\text{ACC}}^{\text{MAX}}$. Furthermore, we also require the paths to be monotonically increasing functions of both coordinates (this guarantees that the product I_{τ} is also monotonically increasing). Our reference paths are thus given by

$$I_{\text{ACC}} = I_{\text{ACC}}^{\text{MAX}} \left(\frac{\tau}{\tau^{\text{MAX}}} \right)^{\alpha} \quad (4.29)$$

for different values of α between 0 and ∞ . They represent straight lines in the logarithmic I_{ACC} vs. τ plot shown in Fig. 4.6, intersecting in the point with coordinates $(\tau^{\text{MAX}}, I_{\text{ACC}}^{\text{MAX}})$.

The results are shown in Fig. 4.7, where the value of the pivot-point en-

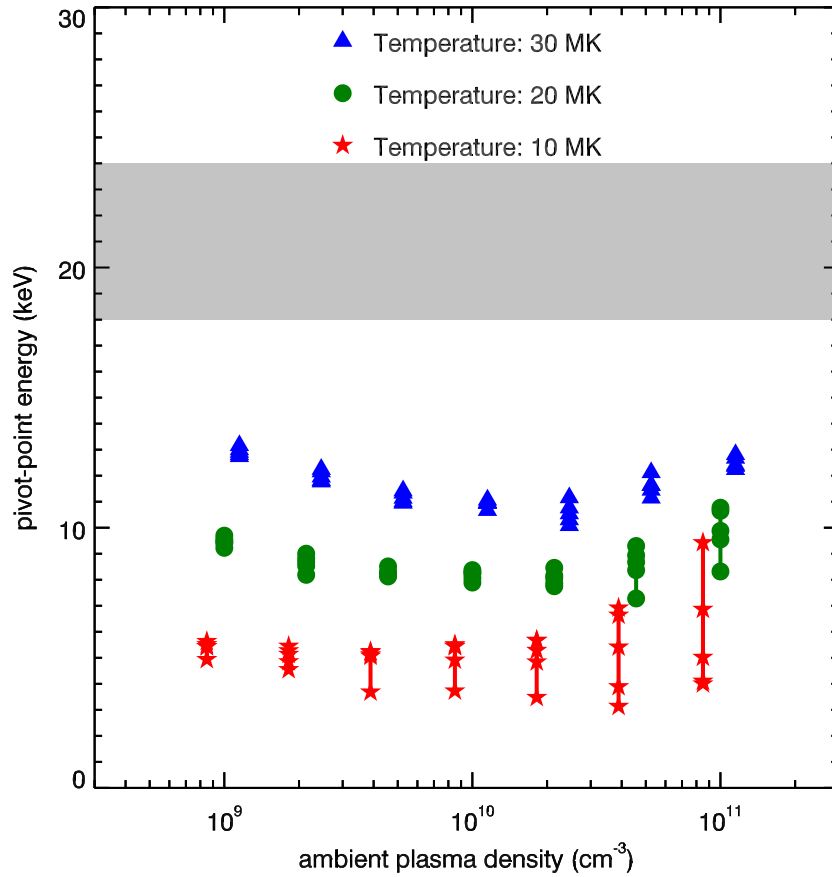


Figure 4.7: Dependence of the photon pivot-point energy ϵ_* on the electron density n for plasma temperatures T of 10 MK (stars), 20 MK (circles) and 30 MK (triangles). The density values of the 10 and 30 MK data points have been shifted by 15% to avoid overlap with the other points. The spread arise from computation of the spectra along different paths as explained in the text. The gray shaded region represents the observed range of values of ϵ_* reported in Table 4.1.

ergy ϵ_* is plotted for 3 different values of the plasma temperature ($T = 10, 20, 30$ MK) and several different values of the plasma density between $n = 10^9 \text{ cm}^{-3}$ and $n = 10^{11} \text{ cm}^{-3}$. The different points for each temperature and density represent the range of variation of ϵ_* for different values of α as explained above. We have used $\alpha = 0, \sqrt{2} - 1, 1, \sqrt{2} + 1, \infty$.

The pivot-point energy increases with temperature. The density dependence of the pivot-point energy is weak, while the pivot-point flux decreases at higher densities. The number of accelerated particles becomes very small at densities of 10^{12} cm^{-3} and higher, because the particles lose energy in the collisions faster than they gain energy from the waves. The spread of the

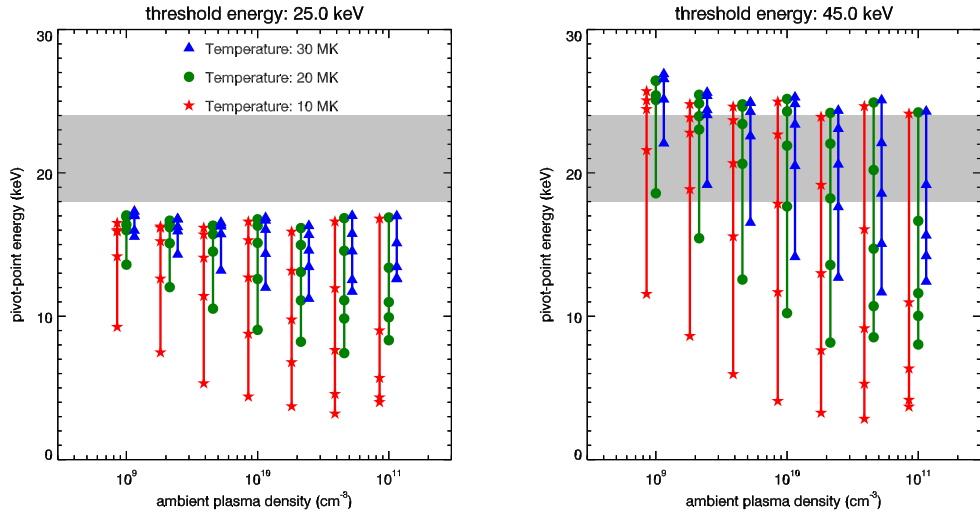


Figure 4.8: Same as in Fig. 4.7, but with a modified escape term featuring perfect trapping below 25 keV (left panel) and below 40 keV (right panel).

pivot-point energies shown in Fig. 4.7 increases at higher densities, as expected from the high-density breakdown of the approximation that the pivot point only depends on $I_{\text{ACC}} \cdot \tau$.

4.4.3 Alternative Escape Modeling

As an alternative way for explaining the high values of ε_* , we now modify the escape mechanism. For instance, if an electric potential V_E is present between the accelerator and the footpoints, electrons with kinetic energy lower than the threshold energy $E_T = eV_E$ will not be able to cross that barrier and will therefore not leave the accelerator. Such an electric field is expected to exist and drive the return current of electrons from the chromosphere. In this scenario the trapping is ideal below E_T , and τ becomes infinitely large.

This means that the escape time is given by:

$$\tau(E) = \begin{cases} \infty & \text{if } E \leq E_T \\ \tau & \text{if } E > E_T \end{cases} \quad (4.30)$$

The results are shown in Fig. 4.8 for two values of E_T , 25 keV and 45 keV. Note that the value of the pivot-point energy ε_* increases with increasing E_T . The pivot-point energies reach the observed values for $E_T \simeq 30$ keV, although even at 45 keV some paths in the τ, I_{ACC} -plane deliver lower pivot-point energies than observed.

The points in Figs. 4.7 and 4.8 with larger pivot-point energy correspond to the paths with the lowest values of α , where the escape time τ changes faster than the acceleration parameter I_{ACC} .

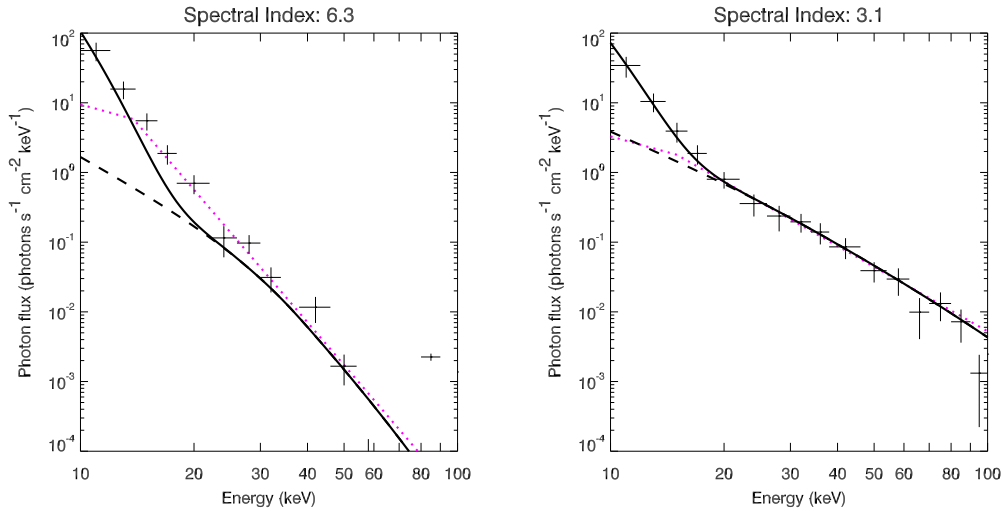


Figure 4.9: Looptop source spectra observed during the M3 flare of December 4, 2002, represented by crosses (bin width and error bar, data courtesy of M. Battaglia). The dotted line is a power-law fit to the data (a low-energy turnover at around 15 keV) with spectral index γ of 6.3 for the *left* panel and 3.1 for the *right* panel. In each panel, the dashed line is a stochastic acceleration model spectrum computed for model parameters: temperature $T = 20$ MK, density $n = 5 \cdot 10^{10} \text{ cm}^{-3}$, and threshold energy $E_T = 40$ keV (chosen such that the pivot-point energy ϵ_* matches the observed value of ~ 18 keV reported in Battaglia & Benz 2006). The continuous line is the sum of the model spectrum with an additional isothermal component, needed to fit the low-energy range of the spectra.

A comparison of observed spectra of a looptop source (for the M3 flare of December 4, 2002) and the spectra computed by the stochastic acceleration model with $E_T = 40$ keV is shown in Fig. 4.9. The model parameters used were temperature $T = 20$ MK and density $n = 5 \cdot 10^{10} \text{ cm}^{-3}$ and $\alpha = \sqrt{2} - 1$, yielding a pivot-point energy $\epsilon_* = 18.7$ keV, similar to observed value of 18.1 keV reported by Battaglia & Benz (2006). The model spectra are represented by the dashed lines, the power-law fit to the data by the dotted line, and the sum of the model spectra with an isothermal component by the continuous line.

In our model, the value of the total photon flux observed at earth depends linearly on the accelerator volume, which acts as a normalization factor for the model spectra. For the comparison with the observed data, the volume can be freely chosen, but is assumed not to change along the path in the τ, I_{ACC} -plane. In practice, that means that the volume can be chosen in order to match the data (or the power-law fittings) at, say, peak time, and automatically the spectra at all the times during the emission peak will match, provided that

the pivot-point energies of the observed and the model spectra are the same.

The low energy part of the observed spectrum shows a thermal emission much larger than the model spectra emission. This can be understood if particle acceleration takes place in a smaller volume than the one where the thermal emission takes place. For the events shown in Fig. 4.9, the filling factor of the accelerator amounts to around 10^{-3} .

The left panel of Fig. 4.9 shows a mismatch between the observed data and the model spectra below 30 keV. This is due to the effect of the escape model used: the suppression of electron escape results in a hardening of the electron spectra below $E_T = 40$ keV. Particles with energy lower than E_T are able to extract more energy out of the waves until they are accelerated beyond E_T . A turnover occurs at around $0.7E_T$ for photon spectra, due to the shape of the bremsstrahlung cross section $d\sigma(\varepsilon, E)$.

4.5 Discussion

The important results are the following:

- The transit-time damping mechanism with escape is able to provide photon spectra with spectral indices in the deka-keV energy range corresponding to the observed range for flares ($\gamma = 2$ to 10 , Dennis 1985, Battaglia et al. 2005) as the ratio between the trapping and accelerating efficiency is varied (Fig. 4.4). This confirms that escape indeed does soften the spectrum for different values of densities and temperatures of the accelerator.
- Assuming constant values of temperature and density in the accelerator (as may be the case during a hard X-ray peak with a duration of some tens of seconds) we are able to produce a correlation between the photon spectral index and flux yielding an approximate pivot point in photon flux vs. energy space (Figs. 4.5 and 4.7)
- The energy of the pivot point in the simplest model is around 10 keV and is lower than the reported observed value of 20 keV.
- An additional increase of the strength of trapping below 20-30 keV (as may be obtained from the presence of a potential barrier) increases the pivot-point energy to 20 keV (Fig. 4.8).
- The potential barrier hardens the spectrum below its threshold energy. For large γ , this flattens the spectrum more than observed in the range where the non-thermal emission still dominates the thermal emission (Fig. 4.9, left).

- The observational upper limit for the energy of a turnover in the photon spectra lies around 15 keV (Saint-Hilaire & Benz 2005). Model spectra computed for threshold energies below about 23 keV yield a turnover lower than 15 keV and pivot-point energies below 16 keV.

What is the physical significance of the pivot point? We would like to point out first that there is not necessarily any: it can be thought of as a useful parameter which describes the variation in flux and spectral index of the observed spectra, and one has to explain this variation first in the context of a model such as done in this work. However, the fact that it appears at an energy which is comparable to the estimated turnover energy of the non-thermal component, as well as the energy below which the thermal component dominates is a suggestive fact.

The model suggests that the main factor influencing the pivot-point energy is the number of electrons available at energy comparable with it. We propose that, in general, the presence of a large supply of electrons at some energy implies a similar energy for the pivot point, on the condition that the electron collisional energy losses are negligible above that energy range, such that the acceleration process can effectively energize that population. It is not important if such a population exist at the beginning of the acceleration, but it must be present in the later stages and be maintained until the equilibrium is reached.

4.6 Conclusions

The model studied assumes that turbulent fast-mode waves are present in the accelerator region. The equilibrium spectrum of electrons subjected to Coulomb collisions and transit-time damping interactions with the waves are computed allowing for trapping/escape and replenishment of “cold” particles. As such the model does not distinguish between the accelerator and the radiator and considers the photon spectra emitted by the electrons in the accelerator itself. The relatively dense looptop sources observed by RHESSI fit this scenario as accelerators/emitters, and the observed high densities support a scenario in which trapping plays an important role in acceleration. Therefore, spectral observations of these looptop sources may well deliver a snapshot of the electrons in the accelerator.

To match the low-energy part of the observed spectrum, we have to add an additional thermal component at the observed temperature. This component fills a much larger volume (factor of 1000). The heating may have occurred by earlier acceleration or may be the result of waves escaping from the accelerator region with energy density too low to yield significant energy gain per particle.

The goals of this work were to test whether a stochastic acceleration mechanism can account for the observed soft-hard-soft behavior and, in particular,

to find a minimal set of modifications to the transit-time damping mechanism yielding a pivot-point like behavior of the electron spectrum in the deka-keV range. Therefore we have not fully investigated the physics of escape, and in particular we leave open the question of the connection between the acceleration process and the trapping mechanism.

The results shown in Section 4.4 confirm that the hardness of the spectrum of accelerated particles in a stochastic acceleration model depends strongly on particle trapping. This can be understood by recalling that stochastic acceleration can be thought as a transport of particles in energy space due to a random walk process. While acceleration pushes particles toward higher energies, the escape acts against this flow, because fast particles are more likely to be lost, and replaced by particles at lower energies. Therefore, when the losses are stronger, the average time a particle spends random-walking in energy space is shorter, thus gaining less energy. This results in softer spectra.

We have used one specific kind of stochastic acceleration model and a simple escape scenario, but the physical mechanisms explored by the specific models are general enough that other stochastic models and escape terms are expected to follow the same general behavior leading to a soft-hard-soft effect, manifesting itself as a correlation of the time evolution of the spectral index and the non-thermal X-ray flux.

A simple escape model cannot account for the observed value of the photon pivot-point energy, which is about a factor 2 higher. The modification in the escape term featuring no escape below a threshold energy $E_T \simeq 40$ keV can increase the energy of the pivot point to the observed values, but at the price of introducing a spectral hardening below 30 keV, which is not observed for large γ .

One possible interpretation of the threshold energy used in the alternative escape model is the presence of an electric field driving the return current. It was treated as a free parameter, but physically the escape process and the return current are linked by the electric conductivity of the loop legs. In this sense the model is not self consistent. The issues of transport of the escaped particles to the footpoint and return currents are important (see for example Zharkova & Gordovsky 2005) and need to be addressed in future work to be able to derive footpoint spectra.

Thus the model is not able to account quantitatively for all the observed features of the intricate spectral behavior of the hard X-ray emission from looptop sources of solar flares. Nevertheless, the model qualitatively accounts for the key features of the spectral evolution, going one step further toward the solution of the acceleration problem. This allows to interpret the impressive RHESSI observations showing spectral variation in looptop sources.

The simplifications introduced by the model may well be responsible for its shortcoming in reproducing the observed spectra for large γ . Future improvements may include an isotropization process and magnetic trapping. This will

require the extension of the model including at least one spatial dimension and the pitch angle distribution of the particles.

Chapter 5

The Evolution of Reconnection along an Arcade of Magnetic Loops

*I'll tell you how the sun rose, —
A ribbon at a time.*

Emily Dickinson (1830–1886)

ABSTRACT: RHESSI observations of a solar flare showing continuous motions of double hard X-ray sources interpreted as footpoints of magnetic loops are presented. The temporal evolution shows many distinct emission peaks of duration of some tens of seconds ('elementary flare bursts'). Elementary flare bursts have been interpreted as instabilities or oscillations of the reconnection process leading to an unsteady release of magnetic energy. These interpretations based on two-dimensional concepts cannot explain these observations, showing that the flare elements are displaced in a third dimension along the arcade. Therefore, the observed flare elements are not a modulation of the reconnection process, but originate as this process progresses along an arcade of magnetic loops. Contrary to previous reports, we find no correlation between footpoint motion and hard X-ray flux. This flare apparently contradicts the predictions of the standard translation invariant 2.5D reconnection models.

5.1 Introduction

High-energetic electrons accelerated during solar flares emit bremsstrahlung hard X-rays (HXR), whose evolution in time can be followed in images, light curves, and spectra. This information is combined here to infer characteristics of the unknown acceleration process of these particles.

As for light curves, quasi-periodic modulations of the HXR flux on time scales of some tens of seconds (*Elementary Flare Bursts*; EFB) have long been known to observers (Parks & Winckler 1969, de Jager & de Jonge 1978). Spectral studies show that EFBs preferentially follow a characteristic *soft-hard-soft* spectral behavior (Chapter 2 and references therein). The modulations of the HXR and microwave flux have been interpreted in 2D models of reconnection as fluctuations in the reconnection process due to global oscillations of the loop (Roberts et al. 1984, Nakariakov et al. 2003, Stepanov et al. 2004).

On the imaging front, early observational evidence from the *Solar Maximum Mission* Hard X-Ray Imaging Spectrometer (Hoyng et al. 1981) showed that HXR sources are found at the location of footpoints (FP) of magnetic loops. Different types of HXR sources located higher in the solar atmosphere were detected on some occasions: the *Yohkoh* Hard X-ray Telescope registered fainter *loop-top* sources above the soft X-ray loops (Masuda et al. 1994) and the *Reuven Ramaty High Energy Solar Spectrometric Imager* (RHESSI, 2002) observed *coronal* sources (2003), as well as emission from collisionally thick coronal loops (Veronig & Brown 2004). However, the bulk of non-thermal HXR comes from loop FPs.

Two FPs on opposite sides of a magnetic neutral line are expected in the standard model of eruptive flares (reviewed e.g. by Priest & Forbes(2002)): The rapid eruption of a filament enables the magnetic field to reconnect, driving particle acceleration in lower loops. Electrons precipitating to a FP emit HXR. In this scenario, one expects the observed FP sources to drift apart as successive field lines are reconnected at higher altitudes. This explanation fits the long-known outward motion of H α ribbons parallel to the neutral line.

Reports on both the morphology and the time evolution of the FPs show a large range of behaviors: single (Takakura et al. 1983), double (Hoyng et al. 1981) and multiple sources are seen, and many authors observe FP motions of different kinds: decrease and increase in the FP separation across the neutral line; parallel and antiparallel movements along the arcade (for some recent observations see Fletcher & Hudson 2002, Liu et al. 2004, Qiu et al. 2004, Siarkowski & Falewicz 2004). This bewildering behavior demonstrates just how complex the flare phenomenon can be.

Krucker et al.(2003) presented high-resolution observations of a particularly interesting two-ribbon flare. One of the HXR FPs moved continuously along a ribbon, whereas the other two FPs showed no systematic motion. No motion

perpendicular to the ribbons are noticeable, but the parallel motion correlated with the HXR flux. The observed behavior allowed Krucker et al. to interpret the observations still in terms of the standard reconnection model, where the motion is due to receding FPs. This requires a strongly sheared arcade and a not-specified complex magnetic structure including the 2 other FPs without systematic motion.

Here HXR source motions observed with RHESSI during a flare are reported that do not allow for such interpretation by the standard 2D reconnection model. We study also the relation between the spatial motion and the spectral evolution of EFBs in time.

5.2 Observations

RHESSI observed the Sun on November 9, 2002 from 12:23 to 13:28 UT, when it entered the shadow of the Earth, and it registered the HXR evolution of a solar flare of soft X-ray (GOES) importance M4.9. RHESSI was in a configuration well suited to the derivation of high-resolution HXR spectra and images: No decimation of the data was active during the flare and attenuation (Smith et al. 2002) was constantly in state 1 (thin attenuator in), thus ensuring that the detector dead time was below about 5% during the flare. Auxiliary data suggest that this flare was an eruptive event, displaying a post-flare loop arcade in the SOHO/EIT 195 Å images (Fig. 5.1), a moving Type IV radio burst (Phoenix spectrometer), and an associated fast CME (listed in the catalog by Yashiro et al. 2004).

Spatially integrated HXR spectra for this event were obtained at a cadence of one RHESSI rotation period (~ 4 s) and used in Chapter 2 to analyze the time evolution of the non-thermal part. Here we additionally produce HXR images averaged over two rotation periods (~ 8 s) in the energy band 20–50 keV using the CLEAN (Hurford et al. 2002a) and the PIXON (Metcalf et al. 1996) reconstruction algorithms. The images resulting from the two different methods were inspected and compared. We discarded images of poor quality, obtaining 43 CLEAN and 69 PIXON images. Most images show two sources located at opposite sides of the magnetic neutral line, for some others only one source is clearly defined. We computed the source positions in each image by fitting a two-dimensional elliptical Gaussian to each visible source separately. For the CLEAN images we were able to estimate the statistical positional error by dividing the 1σ source width (provided by the Gaussian fit) by the signal to noise ratio (obtained dividing the peak flux by the standard deviation of the fluctuations in the image outside the sources). The average error estimated in this way amounts to $1.4''$. This method cannot be applied for the PIXON images, since the PIXON algorithm suppresses the noise in the image.

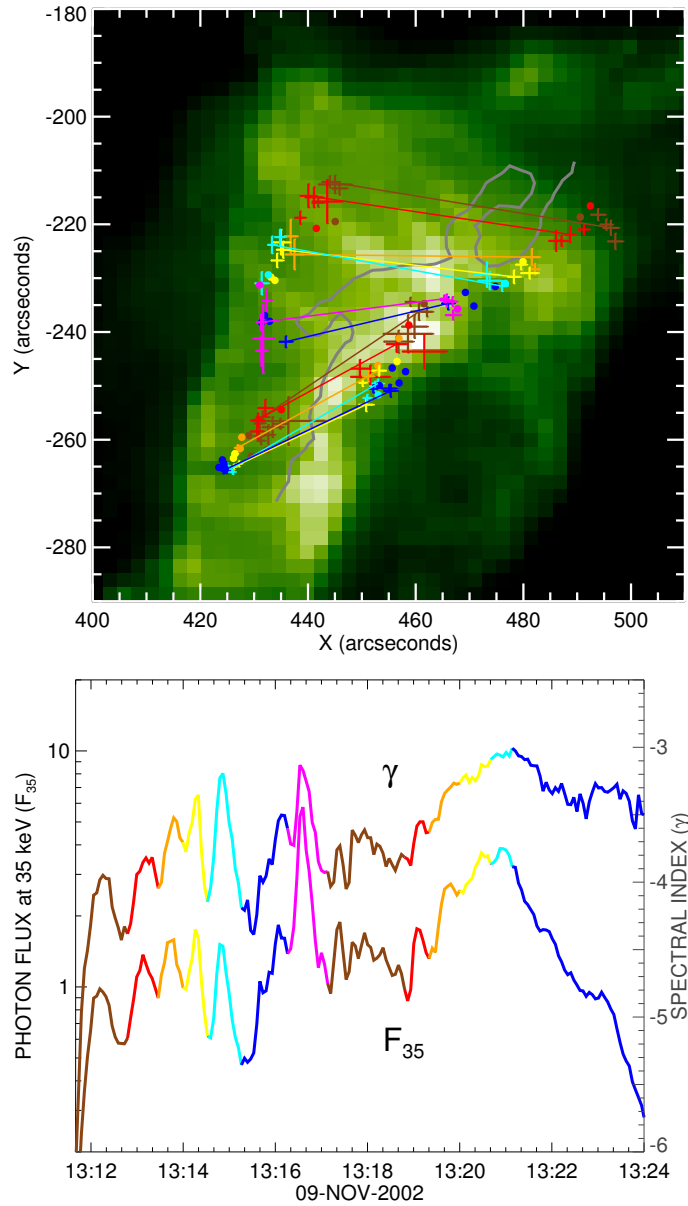


Figure 5.1: *Top*: SOHO/EIT 195 Å image of post-flare loops with the RHESSI HXR source positions superimposed. The positions of the 20 - 50 keV sources from the CLEAN images are represented by crosses with arm lengths equal to the errors, positions from the PIXON images are given by circles. Simultaneous footpoints are connected and color coded according to the time intervals defined in the bottom part. The neutral line is shown in gray. *Bottom*: Time evolution of the flux and spectral index.

The evolution of the positions of the eastern and western FPs are shown in the top panel of Fig. 5.1 superimposed on a SOHO/EIT (Delaboudinière

et al. 1995) image taken at 13:48 UT showing a post-flare loop arcade. The crosses represent the CLEAN positions with their error bars, and the circles the PIXON positions. We compensate for the effect of the solar rotation by rotating each source to the position it would assume at the time of the EIT image.

Both FPs start from the northern part of the image and move along the two ribbons visible to EIT in the south-east direction. The northern part of the arcade is wider than its southern end, and therefore the north-south movement along it effectively causes a convergence of the opposite FPs.

In the bottom panel of Fig. 5.1 the time evolution of the non-thermal HXR flux at 35 keV and the spectral index are presented. Emission peaks with a duration ranging from a few tens of seconds to the observational limit at 8 s can be noted, each showing soft-hard-soft behavior. The main peaks are drawn in a color different from their neighbors such that the source positions in the top panel, having the same code, can be followed in their temporal evolution.

To characterize the motion along the arcade, we define an eastern and a western regression line obtained by two independent least-squares fittings of all the positions of the eastern and western FPs. The two straight lines go from southeast to northwest and are not shown in Fig. 5.1. The lines are inclined by 74° (eastern) and 36° (western) to the east-west direction. From now on, every decomposition of a vector in its *parallel* and *perpendicular* components will refer to the directions given by the regression lines. The parallel coordinate increases from an arbitrary origin towards NW, whereas the perpendicular coordinate is positive in the direction that points away from the arcade.

The motions parallel and perpendicular to the two regression lines are presented in of Fig. 5.2. The FPs move predominantly along the lines, thus parallel to the ribbons. The parallel motion is quite smooth and continuous, especially for the western FP. For both FPs, the speed diminishes after about 13:17 UT. The only large discontinuity in the parallel motion is a possible $20''$ jump of the parallel eastern FP position after the strongest HXR peak when the eastern source is not detectable. Afterwards, the eastern FP moves slower and get stationary after 13:20 UT. Contrary to previous reports, we find no correlation between FP speed and HXR flux.

Do subpeaks show motions perpendicularly outward from the ribbons as expected from the standard reconnection model? In Fig. 5.2 (bottom) this is not obvious, although the two FPs are apparently moving relative to the regression line. Note however, that the lines are converging, thus the effective FP separation decreases. Moreover, the ribbons are not straight. To study the question in more detail, we additionally define two smooth trend curves following the FP motions more closely. A moving average of the PIXON positions of each FP branch was computed, using a boxcar smoothing window of 15 elements, interpolating the missing points. The interval corresponds to a

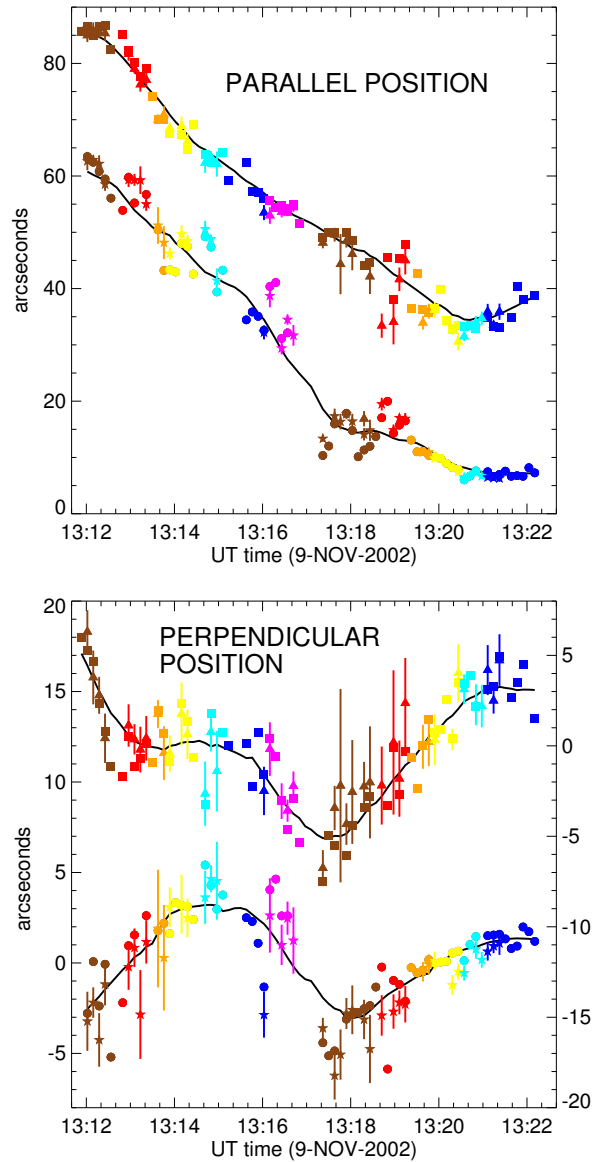


Figure 5.2: Time evolution of the source positions relative to the trend lines. The color code is the same as in Fig. 5.1, referring to the major subpeaks. Triangles and stars with error bars refer to values derived using CLEAN, squares and circles using PIXON, for the western and eastern FPs, respectively. *Top*: The upper curve displays the parallel coordinates of the western FPs, the lower curve the same of the eastern FPs. *Bottom*: Time evolution of the coordinate perpendicular to the regression lines. The upper curve refers to the western FP (scale on the right), the lower curve to the eastern FP (scale on the left). Both panels show in black the averaged smoothed motion for each FP (PIXON value), defining a new reference for detailed analysis.

duration of 120 seconds, longer than all impulsive subpeaks in the HXR light curve (Fig. 5.1, bottom). The smooth trends are shown in Fig. 5.2 as black continuous curves.

The standard reconnection model predicts outward FP motion at a given place in the arcade. In order to look for such systematic trends within HXR subpeaks, we took the parallel and perpendicular components of the difference vector from the smoothed source position to the observed PIXON positions. For each subpeak, we averaged the positions occurring during the first half and the second half, and calculated the difference second minus first half, Δ_{POS} , for both eastern and western sources.

For elementary flare bursts produced by standard reconnection, one would expect outward moving sources, thus $\Delta_{\text{POS}}^{\perp}$ being positive, at least on the average. Furthermore, the motion along the ribbons should be stepwise and discontinuous with $\Delta_{\text{POS}}^{\parallel}$ being positive if each Elementary Flare Burst were a localized event. Figure 5.3 demonstrates that these expectations are not satisfied during subpeaks of this flare. The distribution of the average perpendicular motion during each peak shown in Fig. 5.3 has a mean $\Delta_{\text{POS}}^{\perp}$ value of $0.0'' \pm 0.4''$ for the eastern FP and $0.2'' \pm 0.5''$ for the western FP (the error is the standard error of the average). The mean value of the relative parallel motion during the peaks is $-1.0'' \pm 1.0''$ for the eastern FP and $0.4 \pm 0.7''$ for the western FP.

The global motion along the arcade progresses with an average velocity in the parallel direction of 63 km s^{-1} for the eastern FP and 55 km s^{-1} for the western FP. The lower velocity of the western FP is due to the fact that the latest data points have negative parallel velocities since they move backwards (Fig. 5.2). Averaging the absolute values of the parallel component of the velocity, we get 65 km s^{-1} for the western FP. A speed of about 110 km s^{-1} is maintained for 2 minutes in the western FP at the beginning of the flare, while the data gap and possible jump around 13:17 in the eastern FP position requires 180 km s^{-1} .

The line connecting the two FPs is inclined with respect to the post-flare loops seen in the EIT image (Fig. 5.1). The angle is in the range of 25° to 70° , the post-flare loops being nearly perpendicular to the neutral line. This indicates that the HXR emitting loops are strongly sheared. RHESSI images at lower energy where thermal emission dominates the spectrum show sources or loops between the FPs. They appear to be coronal sources moving along the arcade with the FPs at higher energies.

5.3 Conclusion

We have analyzed RHESSI HXR observations of the time evolution of both images and spectra for a solar flare of GOES class M4.9. Surprisingly, the

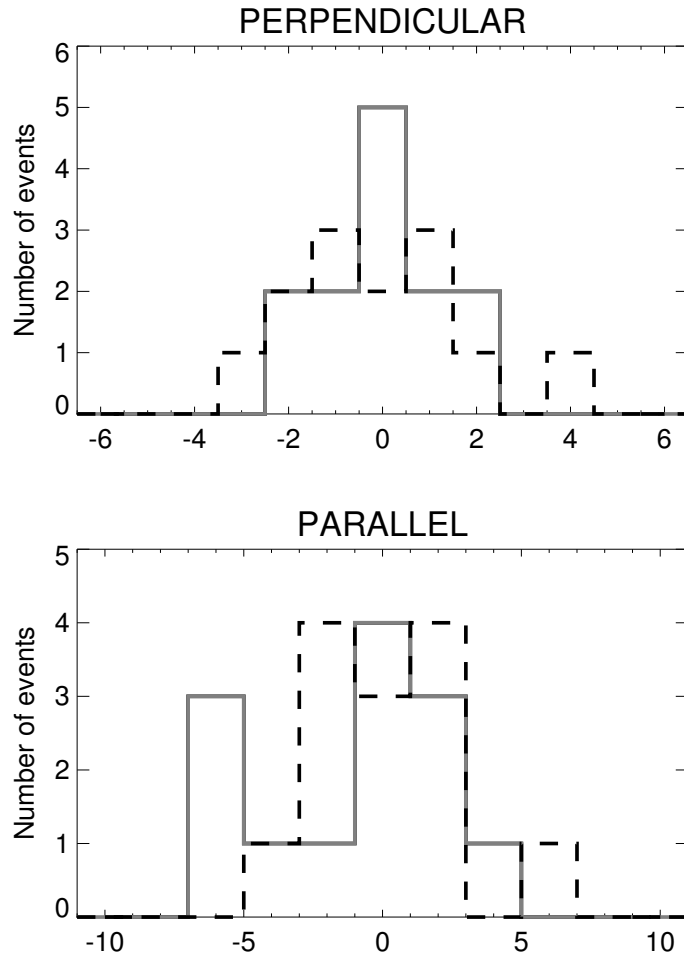


Figure 5.3: Distribution of the average motions during a peak in perpendicular and parallel directions relative to the time averaged trend curves. Eastern FPs are shown with continuous lines, western FPs with dashed lines.

footpoints move smoothly along the two ribbons in contrast to the bursty evolution of the HXR flux. The observed Elementary Flare Bursts have durations between 30 s and less than 8 s, and show pronounced spectral soft-hard-soft behavior. The parallel source motions exclude the generally held notion of Elementary Flare Bursts being the modulation of a global reconnection process. Instead, the temporal modulation of the HXR flux and spectral index appear to be caused by a spatial displacement along the arcade. This could be caused by some disturbance propagating smoothly along the arcade, sequentially triggering a reconnection process in successive loops of the arcade. The disturbance would have to propagate with a speed in the range $50\text{--}150\text{ km s}^{-1}$, much lower than the Alfvén velocity.

In the impulsive phase of this flare, magnetic energy release appears not in the form of a quasi-steady reconnection annihilating anti-parallel magnetic field and thus producing outward moving FPs. The main flare energy release at a given position in the arcade seems to last only a short time (order of a few seconds) and moves along the arcade in a systematic manner. The observed modulation of the HXR flux and the related anti-correlation of the spectral index in each Elementary Flare Burst appear to be caused by spatial variations of the acceleration efficiency. The temporal variations thus seem to be the result of a continuously moving trigger propagating through variable conditions in the arcade. The short lifetime of a FPs at a given position shows that particle trapping is not effective over timescales larger than several tens of seconds.

The observed simple and systematic motions set this event apart as a prototype for a type of HXR flare evolving *along the arcade*. The FP motions of this flare contradict clearly the expectations of the standard 2D reconnection model. The fact that we do not observe a systematic increase (up to the instrumental limits) of the separation of the FPs, does challenge the idea that the reconnection points move upwards and particles are accelerated in field lines successively farther out during the main HXR emitting phase of the flare. A possible interpretation is that the trigger releases the main energy stored in a two-dimensional loop structure within seconds, without noticeable FP motion, and moves on. Reconnection in the given structure may still continue, but with HXR emission below RHESSI sensitivity and at a much reduced energy release rate. Such secondary reconnection may be the cause of decimetric radio emissions continuing for 6 minutes after 13:22 UT, the end of HXR emission, and may produce the expansion of the two H α ribbons as observed in other flares.

We thus propose a scenario in which a disturbance, probably connected with the eruption of a filament, propagates along the arcade like a burning fuse, sequentially triggering reconnection and particle acceleration in the flare loops. The main HXR emission from the FP reflects the propagation of this disturbance, not the reconnection process at a given place in the arcade. If the dominating emission is strong and short-lived, the local conditions cause the observed temporal modulation.

The global evolution may be compatible with the standard model of an eruptive flare, if one allows the filament to erupt in such a way that one of its ends does not move while the other starts to rise. In this scenario the reconnection process spreads along the arcade until it reaches the end. The arcade erupts in a manner similar to the opening of a zipper, where the lower side runs across the arcade and the upper side is the filament. Future studies of HXR FPs in a large number of flares may establish such a scenario and stimulate the development of 3D reconnection models needed to understand these observations.

Chapter 6

Summary and Outlook

*On tyme y-passed, wel remembred me;
And present tyme eek coude I wel y-see.
But futur tyme, er I was in the snare,
Coude I not seen; that causeth now my care.*

Geoffrey Chaucer (c. 1343–1400)

The behavior of the hard X-ray emission during solar flares was studied in this thesis. We have concentrated on the spectral evolution, conspicuous in most flares. While the qualitative soft-hard-soft trend in impulsive flares has been known for a long time, we were able to give a quantitative description of the relationship between index and normalization of the power-law component. The behavior is consistent with the presence of a pivot point, a common crossing point of the different power-law components at different times. We can account for such a behavior in the spectra of the accelerated electrons using a stochastic acceleration model. The spectrum is harder when either the acceleration is stronger or the escape is weaker. The coordinates of the pivot point depend on the physical model parameters, therefore it is possible to constrain those by the observation of the pivot-point position in the hard X-ray data.

The model used to describe the acceleration process is strongly simplified. The spectral evolution is described by only one non-trivial parameter: the pivot-point energy. The model does not fit the whole evolution of the non-thermal component of the flare spectrum. We suggest that the model could be improved by the implementation of a more physical escape process and an explicit mechanism for particle isotropization. These are in fact closely related, because pitch angle scatterings (that is, changes in the *direction* of the particle relative to the magnetic field) can account for both processes. This requires

that the electron distribution function, now a function of the energy only, be extended into a function of both energy and pitch angle, and the specification of the physical mechanism responsible for the pitch angle scatterings.

Contrary to the emission from heated plasma, which rises and decays smoothly, the emission from the accelerated particles is much richer in features. Often several distinct emission spikes are seen. This means that acceleration or escape is fragmented. How far does the fragmentation go? The observations show that the different peaks of the emission share a common *soft-hard-soft* spectral pattern, and therefore some form of organization during the peak is needed. Indeed the stochastic model presented accounts for the main features observed in the spectral evolution if the energy input increases and decreases in the whole accelerator in a coherent manner. The hard X-ray images show that the emission region does not stay the same during the flare, but wanders along the arcade of magnetic loops. In this case the fragmentation is *spatial*, showing that different magnetic loops are involved at different times. Again, this must proceed in an orderly manner.

All this suggests that, while the acceleration process itself may well be fragmented, the geometry of the magnetic environment controls and drives the flare evolution in a coherent manner. The main observational difficulties in understanding the connection between the magnetic configuration and the acceleration is due to our poor knowledge of the conditions in the corona. Two new solar missions, to be started in autumn 2006, will provide data which can be profitably combined with RHESSI's observations of the high-energetic particles. NASA's Solar TERrestrial RELations Observatory (STEREO) will provide stereographic observations of the corona, making possible to reconstruct its 3-dimensional structure. The Japanese Solar-B mission will provide a coverage of the soft X-rays and extreme ultraviolet emission, enabling a better characterization of the hot plasma produced by the flare, pinpointing the location of heating. In a next step, solar observatories will go closer to the sun. Solar Orbiter from ESA and the Inner Heliospheric Sentinels from NASA will travel inside the orbit of Mercury, allowing an *in situ* exploration of the outer parts of the corona.

The interplay between these different observations should also help understanding the more global questions of the connection between flares and coronal mass ejections. Does one cause the other? Or rather are they just related manifestations of some basic underlying mechanism? Furthermore, how are solar energetic particles accelerated and injected into the heliosphere? All these questions have direct relevance to space-weather related issues, which affect technological artifacts both in Earth's orbit and on its surface. To answer such problems, knowledge on both the coronal configuration (such as provided by ultraviolet and soft X-ray imagers) and the properties of the flare accelerated particles (hard X-ray and gamma ray spectrometers, *in situ* detectors) is required.

Appendix A

Diffusion Equation in Energy Space

In this Appendix, the diffusion equation in energy space

$$\frac{\partial N}{\partial t} = \frac{1}{2} \frac{\partial^2}{\partial E^2} D(E) N - \frac{\partial}{\partial E} A(E) N, \quad (\text{A.1})$$

with diffusion coefficient $D(E)$ and convection coefficient $A(E)$ is shown to be equivalent to the momentum diffusion equation for the spherical symmetric, spatial homogeneous case:

$$\frac{\partial f}{\partial t} = \frac{1}{p^2} \frac{\partial}{\partial p} \left[p^2 D(p) \frac{\partial f}{\partial p} \right], \quad (\text{A.2})$$

where $D(p)$ is the momentum diffusion coefficient. The energy differential distribution function $N(E)$ is defined in term of the momentum distribution function $f(p)$ by the condition

$$N(E) dE = 4\pi p^2 f(p) dp, \quad (\text{A.3})$$

stating that the number of particle with a given energy is the same in both representations.

We list the following useful relations between energy and momentum in the relativistic case:

$$\begin{aligned} E = mc^2\gamma & \quad p = mc\beta\gamma & \quad E^2 = p^2c^2 + m^2c^4 & \quad \beta = \frac{p/mc}{\sqrt{1 + (p/mc)^2}} \\ dE = c\beta dp & \quad N(E) = \frac{4\pi p^2}{c\beta} f(p) & \quad \frac{\partial}{\partial E} = \frac{1}{c\beta} \frac{\partial}{\partial p} \end{aligned}$$

With the following definition for the coefficients in energy space

$$D(E) = 2c^2\beta^2 D(p) \quad \text{and} \quad A(E) = \frac{1}{p^2} \frac{\partial}{\partial p} [c\beta p^2 D(p)] , \quad (\text{A.4})$$

Equation A.1 can be transformed into

$$\begin{aligned} \frac{4\pi p^2}{c\beta} \frac{\partial f(p)}{\partial t} &= \frac{1}{2c\beta} \frac{\partial}{\partial p} \left\{ \frac{1}{c\beta} \frac{\partial}{\partial p} \left[2c^2\beta^2 D(p) \frac{4\pi p^2}{c\beta} f(p) \right] \right\} - \\ &\quad \frac{1}{c\beta} \frac{\partial}{\partial p} \left\{ \frac{1}{p^2} \frac{\partial}{\partial p} [c\beta p^2 D(p)] \frac{4\pi p^2}{c\beta} f(p) \right\} , \end{aligned}$$

which simplifies into

$$\begin{aligned} \frac{\partial f(p)}{\partial t} &= \frac{1}{p^2} \frac{\partial}{\partial p} \left\{ \frac{1}{c\beta} \frac{\partial}{\partial p} [c\beta p^2 D(p) f(p)] - \frac{1}{c\beta} \frac{\partial}{\partial p} [c\beta p^2 D(p)] f(p) \right\} \\ &= \frac{1}{p^2} \frac{\partial}{\partial p} \left\{ p^2 D(p) \frac{\partial f(p)}{\partial p} \right\} , \end{aligned}$$

thus proving the equivalence.

Appendix B

Approximate Analytical Solution

We compute here an approximate analytical solution in the energy range $kT/(mc^2) \ll E \ll 1$. In this range, we can neglect the influence of the Coulomb collisional coefficients A_C and D_C as well as the source term Q . In equilibrium Eq. (4.13) becomes:

$$\frac{D_0}{2} \frac{\partial^2 N}{\partial E^2} + (D_1 - A_0) \frac{\partial N}{\partial E} + (D_2 - A_1 - S) N = 0, \quad (\text{B.1})$$

where the coefficients A_i and D_i are the factors of order i occurring in the Taylor expansion of A and D around E_0 . Their computation is tedious, but straightforward. The full second order expansion in $\epsilon = E - E_0$ is reported here:

$$\begin{aligned} E &= E_0 + \epsilon \\ \gamma &= \gamma_0 + \epsilon \\ \beta &= \beta_0 + \frac{1}{\beta_0 \gamma_0^3} \epsilon - \frac{3\beta_0^2 \gamma_0^2 + 1}{2\beta^3 \gamma^6} \epsilon^2 \\ \xi &= \xi_0 - \frac{\xi_0}{\beta_0^2 \gamma_0^3} \epsilon + \frac{\xi_0}{\beta_0^4 \gamma_0^4} \epsilon^2 \\ f &= f_0 + f_1 \epsilon + 1/2 f_2 \epsilon^2 \\ f_1 &= \frac{1 + 4\xi_0^2 \ln \xi_0}{\beta_0^2 \gamma_0^3} \\ f_2 &= -2 \frac{3\gamma_0^2 - 1 + 4\xi_0^2 + 12\gamma_0^2 \xi_0^2 \ln \xi_0 + 4\xi_0^2 \ln \xi_0}{2\beta_0^4 \gamma_0^6} \\ g &= g_0 + g_1 \epsilon + 1/2 g_2 \epsilon^2 \\ g_1 &= -\frac{\xi_0^2 + 2\gamma_0^2 \xi_0^2 \ln \xi_0 + (1/2)\beta_0^2 \gamma_0^2}{\gamma_0^5 \beta_0^2} \end{aligned}$$

$$\begin{aligned}
g_2 &= 2 \frac{14\xi_0^2\gamma_0^2 - 2\xi_0^2 + 4\gamma_0^2\xi_0^2 \ln \xi_0 + 12\gamma_0^4\xi_0^2 \ln \xi_0 + 3\beta_0^4\gamma_0^4}{4\gamma_0^8\beta_0^4} \\
A_T &= A_0 + A_1\epsilon + 1/2 A_2\epsilon^2 \\
A_1 &= I_{\text{acc}} \left[\frac{g_0 + f_0}{\beta_0} + (g_1 + f_1)\gamma_0\beta_0 \right] \\
A_2 &= 2I_{\text{acc}} \left[-\frac{g_0 + f_0}{2\gamma_0^3\beta_0^3} + \frac{g_1 + f_1}{\beta_0} + (g_2 + f_2)\gamma_0\beta_0 \right] \\
D_T &= D_0 + D_1\epsilon + 1/2 D_2\epsilon^2 \\
D_1 &= \frac{I_{\text{acc}}}{2} \left[f_0\beta_0 \frac{2\gamma_0^2 + 1}{\gamma_0} + f_1\gamma_0^2\beta_0^3 \right] \\
D_2 &= 2\frac{I_{\text{acc}}}{2} \left[f_2\gamma_0^2\beta_0^3 + f_1\beta_0 \frac{2\gamma_0^2 + 1}{\gamma_0} + f_0 \frac{2\gamma_0^4 - \gamma_0^2 + 2}{2\gamma_0^4\beta_0} \right]
\end{aligned}$$

Neglecting the term of order ξ^2 and setting $\gamma_0 = 1$ we get

$$D_0 = K\beta^3 (-5/4 - \log \xi) \quad (\text{B.2})$$

$$D_1 = K\beta (-11/4 - 3 \log \xi) \quad (\text{B.3})$$

$$D_2 = \frac{2K}{\beta} (-17/8 - 3/2 \cdot \log \xi) \quad (\text{B.4})$$

$$A_0 = 2K\beta (-1 - \log \xi) \quad (\text{B.5})$$

$$A_1 = \frac{2K}{\beta} (-1/4 - \log \xi) \quad (\text{B.6})$$

where $K = \frac{\pi}{8}\beta_A^2 I_{\text{ACC}}$, $\xi = \beta_A/\beta$.

The solution $N(E)$ will be approximatively given by a power-law around $E = E_0$

$$N(E) = N_0 \left(\frac{E}{E_0} \right)^{-\delta}. \quad (\text{B.7})$$

Plugging this function into Eq. (B.1) yields a quadratic equation for δ :

$$c_2\delta^2 + c_1\delta + c_0 = 0 \quad (\text{B.8})$$

with coefficients

$$c_2 = \frac{\tau D_0}{2E_0^2} \quad (\text{B.9})$$

$$c_1 = \frac{\tau}{E_0} \left(\frac{D_0}{2E_0} - D_1 + A_0 \right) \quad (\text{B.10})$$

$$c_0 = \tau D_2 - \tau A_1 - \sqrt{2E_0} \quad (\text{B.11})$$

The solution of the quadratic equation yields δ as a function of $I_\tau = I_{\text{ACC}} \cdot \tau$ and the model parameters. The asymptotic behavior of the solution is the following: δ is constant for $I_\tau \rightarrow \infty$, and δ is proportional to $1/\sqrt{I_\tau}$ for $I_\tau \rightarrow 0$.

Curriculum Vitæ

Name	Paolo Claudio Grigis
Date of birth	September 24, 1977
Place of birth	Locarno, Switzerland
Nationality	Swiss
1992 - 1996	Liceo cantonale di Locarno
1996 - 2001	Studies in Physics, ETH Zürich
2001	Diploma thesis: <i>Theory of quantum ferromagnetism</i> Thesis supervisor: Prof. Dr. Jürg Fröhlich
2002 - 2006	Research assistant at the Radio Astronomy and Plasma Physics Group, Institute of Astronomy, ETH Zürich
2006	Doctoral thesis: <i>Observations and Models of the Dynamical Evolution of Solar Flares</i> Thesis supervisor: Prof. Dr. A. O. Benz

List of Publications

Publications in Refereed Journals

- Electron Acceleration in Solar Flares: Theory of Spectral Evolution
P. C. Grigis and A. O. Benz
2006, *Astronomy and Astrophysics*, **458**, 641–651
- The Evolution of Reconnection along an Arcade of Magnetic Loops
P. C. Grigis and A. O. Benz
2005, *The Astrophysical Journal Letters*, **625**, L143–L146
- The spectral evolution of impulsive solar X-ray flares. II. Comparison of observations with models
P. C. Grigis and A. O. Benz
2005, *Astronomy and Astrophysics*, **434**, 1173–1181
- The spectral evolution of impulsive solar X-ray flares
P. C. Grigis and A. O. Benz
2004, *Astronomy and Astrophysics*, **426**, 1093–1101

Coauthored Publications in Refereed Journals

- Event-Based RHESSI Imaging Spectroscopy
K. Arzner, A. Zehnder, M. Battaglia, P. C. Grigis
2006, *Solar Physics*, submitted
- X-Ray Polarization of Solar Flares measured with RHESSI
E. Suarez-Garcia, W. Hajdas, C. Wigger, K. Arzner, M. Güdel, A. Zehnder and P. Grigis
2006, *Solar Physics*, in press
- Particle acceleration in solar flares: observations versus numerical simulations
A. O. Benz, P. C. Grigis, M. Battaglia
2006, *Plasma Physics and Controlled Fusion*, in press

- Nobeyama radio heliograph observations of RHESSI microflares
M. R. Kundu, E. J. Schmahl, P. C. Grigis, V. I. Garaimov and K. Shibasaki
2006, *Astronomy and Astrophysics*, **451**, 691–707
- A broadband FFT spectrometer for radio and millimeter astronomy
A. O. Benz, P. C. Grigis, V. Hungerbühler, H. Meyer, C. Monstein, B. Stuber and D. Zardet
2005, *Astronomy and Astrophysics*, **442**, 767–773
- Size dependence of solar X-ray flare properties
M. Battaglia, P. C. Grigis and A. O. Benz
2005, *Astronomy and Astrophysics*, **439**, 737–747
- Survey on Solar X-ray Flares and Associated Coherent Radio Emissions
A. O. Benz, P. C. Grigis, A. Csillaghy, and P. Saint-Hilaire
2005, *Solar Physics*, **226** 121–142
- RHESSI and radio imaging observations of microflares
M. R. Kundu, G. Trottet, V. I. Garaimov, P. C. Grigis and E. J. Schmahl
2005, *Advances in Space Research*, **35**, 1778-1784
- Micro-events in the active and quiet solar corona
A. O. Benz and P. C. Grigis
2003, *Advances in Space Research*, **32**, 1035-1042
- Microflares and hot component in solar active regions
A. O. Benz and P. C. Grigis
2002, *Solar Physics*, **210** 431–444

Conference Proceedings and Others

- RHESSI Observation of Flare Elements
P. C. Grigis and A. O. Benz
2005, Proceedings of the 11th European Solar Physics Meeting "The Dynamic Sun: Challenges for Theory and Observations" (ESA SP-600). 11-16 September 2005, Leuven, Belgium. Editors: D. Danesy, S. Poedts, A. De Groof and J. Andries. Published on CD ROM., p.35.1
- Time evolution of the spectral index in solar flares
P. C. Grigis, D. Buser and A. O. Benz
2005, Solar Magnetic Phenomena, Proceedings of the 3rd Summerschool

and Workshop held at the Solar Observatory Kanzelhöhe, Kärnten, Austria, August 25 – September 5, 2003. Edited by A. Hanslmeier, A. Veronig, and M. Messerotti. Astronomy and Astrophysics Space Science Library, vol. 320, Springer, Dordrecht, The Netherlands, 2005., p.199-202

Acknowledgments

When I started my career as a doctoral student I knew very little of solar physics. Fortunately, this fact did not discourage my advisor, Arnold Benz, to offer me the position. He trusted me to learn enough on the way, and supported me with his heedful advice and careful mentoring. He also gave me the opportunity to present my results at different meetings, which I greatly enjoyed. My sincere thanks to him for everything he did for me in the last four years.

I thank Manuel Güdel for accepting to be a co-referee of this thesis, for his sound advice, as well as for his interesting anecdotal expositions of what goes on behind the curtains of the scientific enterprise.

I am grateful to Jan Stenflo for kindly accepting to be a co-referee of this thesis.

My colleagues at the institute provided a friendly and fruitful work environment: Nadine Afram, Kaspar Arzner, Marc Audard, Marina Battaglia, Kevin Briggs, Simon Bruderer, Dominique Buser, Barbara Codoni, André Csillaghy, Laure Fouchet, Adrian Glauser, Reto Knaack, Owen Matthews, Peter Messmer, Hansueli Meyer, Christian Monstein, Gunnar Paesold, Pascal Saint-Hilaire, Kester Smith, Pascal Stäuber, Peter Steiner, Alessandra Telleschi, Thomas Wenzler.

I am indebted to Pascal Saint-Hilaire for teaching me everything he knew about RHESSI data analysis: without his support, this work would not have been possible. Furthermore, I thank Marina Battaglia for her eagerness to discuss various aspects of solar physics.

I am very grateful to the whole RHESSI team for providing easy access to the data analysis software: their efforts are the foundation upon which this work has been built.

Finally, I would like to thank my parents for their unwavering support during my studies.

Bibliography

- Arzner, K. 2002, *Sol. Phys.*, 210, 213
- Arzner, K., Güdel, M. 2004, *ApJ*, 602, 363
- Aschwanden, M. J. 2002, *Space Sci. Rev.*, 101, 1
- Aschwanden, M. J. 2005, *Physics of the Solar Corona. An Introduction with Problems and Solutions* (2nd edition), Springer, Berlin
- Battaglia, M & Benz, A. O. 2006, *A&A*, 456, 751
- Battaglia, M., Grigis, P. C., & Benz, A. O. 2005, *A&A*, 439, 737
- Benz, A. O. 1977, *ApJ*, 211, 270
- Benz, A. O., & Grigis, P. C. 2002, *Sol. Phys.*, 210, 431
- Bethe, H., & Heitler, W. 1934, *Royal Society of London Proceedings Series A*, 146, 83
- Brosius, J. W., Davila, J. M., Thomas, R. J., & Monsignori-Fossi, B. C. 1996, *ApJS*, 106, 143
- Brown, J. C. 1971, *Sol. Phys.*, 18, 489
- Brown, J. C., & Melrose, D. B. 1977, *Sol. Phys.*, 52, 117
- Brown, J. C., & Loran, J. M. 1985, *MNRAS*, 212, 245
- Brown, J. C., Krucker, S., Güdel, M., & Benz, A. O. 2000, *A&A*, 359, 1185
- Brown, J. C., Emslie, A. G., & Kontar, E. P. 2003, *ApJ*, 595, L115
- Buser, D. 2003, Diploma Thesis,
<http://e-collection.ethbib.ethz.ch/show?type=dipl&nr=106>
- Carrington, R. C. 1859, *MNRAS*, 20, 13
- Cliver, E. W., Dennis, B. R., Kiplinger, A. L., et al. 1986, *ApJ*, 305, 920

- Cliver, E. W. 1995, *Sol. Phys.*, 157, 285
- de Jager, C., & de Jonge, G. 1978, *Sol. Phys.*, 58, 127
- Delaboudinière, J.-P., et al. 1995, *Sol. Phys.*, 162, 291
- Dennis, B. R. 1985, *Sol. Phys.*, 100, 465
- Elwert, G. 1939, *Ann. Phys.* 34, 178
- Emslie, A. G., Kontar, E. P., Krucker, S., & Lin, R. P. 2003, *ApJ*, 595, L107
- Emslie, A. G., et al. 2004, *J. Geophys. Res.*, 109, 10104
- Fivian, M., Hemmeck, R., Mchedlishvili, A., & Zehnder, A. 2002, *Sol. Phys.*, 210, 87
- Fletcher, L. & Hudson, H. S. 2002, *Sol. Phys.*, 210, 307
- Forbush, S. E. 1946, *Phys. Rev.* , 70, 771
- Frost, K. J., & Dennis, B. R. 1971, *ApJ*, 165, 655
- Hey, J. S. 1946, *Nature*, 157, 47
- Hey, J. S., Parsons, S. J., & Phillips, J. W. 1948, *MNRAS*, 108, 354
- Hodgson, R. 1859, *MNRAS*, 20, 15
- Hudson, H. S. & Fárník, F. 2002, *ESA SP-506: Solar Variability: From Core to Outer Frontiers*, 261
- Gan, W. Q. 1998, *Ap&SS*, 260, 515
- Grigis, P. C. & Benz, A. O. 2004, *A&A*, 426, 1093
- Grigis, P. C., & Benz, A. O. 2005a, *A&A*, 434, 1173
- Grigis, P. C., & Benz, A. O. 2005b, *ApJ*, 625, L143
- Grigis, P. C., & Benz, A. O. 2006, *A&A*, 458, 641
- Hale, G. E. 1892, *Astron. Astrophys.*, 11, 917
- Holman, G. D., Sui, L., Schwartz, R. A. & Emslie, G. A. 2003, *ApJ*, 595, L97
- Hoyng, P., et al. 1981, *ApJ*, 246, L155
- Hudson, H. S. 1991, *Sol. Phys.*, 133, 357
- Hurford, G. J., et al. 2002a, *Sol. Phys.*, 210, 61

- Hurford, G. J., & Curtis, D. W. 2002b, *Sol. Phys.*, 210, 101
- Kane, S. R., & Anderson, K. A. 1970, *ApJ*, 162, 1003
- Kane, S. R., McTiernan, J. M., & Hurley, K. 2005, *A&A*, 433, 1133
- Kiplinger, A. L. 1995, *ApJ*, 453, 973
- Koch, H. W., & Motz, J. W. 1959, *Reviews of Modern Physics*, 31, 920
- Krucker, S., Benz, A. O., Bastian, T. S., & Acton, L. W. 1997, *ApJ*, 488, 499
- Krucker, S., & Benz, A. O. 1998, *ApJ*, 501, L213
- Krucker, S., Hurford, G. J., & Lin, R. P. 2003, *ApJ*, 595, L103
- Kundu, M. R., Schmahl, E. J., Grigis, P. C., Garaimov, V. I., & Shibasaki, K. 2006, *A&A*, 451, 691
- Isobe, T., Feigelson, E. D., Akritas, M. G., & Babu, G. J. 1990, *ApJ*, 364, 104
- Larosa, T. N., & Moore, R. L. 1993, *ApJ*, 418, 912
- Lin, R. P. & Schwartz, R. A. 1986, *ApJ*, 312, 462
- Lin, R. P., Dennis, B. R., Hurford, G. J., et al. 2002, *Sol. Phys.*, 210, 3
- Lin, R. P., Krucker, S.; Hurford, G. J, et al. 2003, *ApJ*, 595, L69
- Liu, W., Jiang, Y. W., Liu, S., & Petrosian, V. 2004, *ApJ*, 611, L53
- Lu, E. T. & Hamilton, R. J. 1991, *ApJ*, 380, L89
- Masuda, S., Kosugi, T., Hara, H., Tsuneta, S., & Ogawara, Y. 1994, *Nature*, 371, 495
- Metcalf, T. R., Hudson, H. S., Kosugi, T., Puetter, R. C., & Pina, R. K. 1996, *ApJ*, 466, 585
- Miller, J. A., Larosa, T. N., & Moore, R. L. 1996, *ApJ*, 461, 445
- Miller, J. A. 1998, *Space Sci. Rev.*, 86, 79
- Nakariakov, V. M., Melnikov, V. F., & Reznikova, V. E. 2003, *A&A*, 412, L7
- Parker, E. N. 1988, *ApJ*, 330, 474
- Parks, G. K. & Winckler, J. R. 1969, *ApJ*, 155, 117

- Peterson, L., & Winckler, J. R. 1958, *Phys. Rev. Lett.*, 1, 205
- Petrosian, V. & Liu, S. 2004, *ApJ*, 610, 550
- Pratt, R. H., & Tseng, H. K., 1975, *Phys. Rev. A*, 11, 1797
- Priest, E. R., & Forbes, T. G. 2002, *A&A Rev.*, 10, 313
- Qiu, J., Lee, J., & Gary, D. E. 2004, *ApJ*, 603, 335
- Roberts, B., Edwin, P. M., & Benz, A. O. 1984, *ApJ*, 279, 857
- Richardson, R. S. 1937, *PASP*, 49, 233
- Saint-Hilaire, P., Von Praun, C., Stolte, E., et. al. 2002 *Sol. Phys.*, 210, 143
- Saint-Hilaire, P., & Benz, A. O. 2005, *A&A*, 435, 743
- Schwartz, R. A., Csillaghy, A., Tolbert, A. K., Hurford, G. J., Mc Tiernan, J., & Zarro, D. 2002, *Sol. Phys.*, 210, 165
- Siarkowski, M., & Falewicz, R. 2004, *A&A*, 428, 219
- Smith, D. M., Lin, R. P., Turin, P., et al. 2002, *Sol. Phys.*, 210, 33
- Spitzer, L. *Physics of Fully Ionized Gases*, New York: Interscience Publishers, 1962
- Stepanov, A. V., et al. 2004, *Astronomy Letters*, 30, 480
- Sui, L., Holman, G. D., & Dennis, B. R. , 2005, *ApJ*, 626, 1102
- Sweet, P. A. 1969, *ARA&A*, 7, 149
- Takakura, T., Tsuneta, S., Nitta, N., & Ohki, K. 1983, *Sol. Phys.*, 86, 323
- Tandberg-Hanssen, E. & Emslie, A. G., 'The physics of solar flares', Cambridge University Press, 1988
- Trubnikov, B. A., 1965, *Reviews of Plasma Physics*, 1, 105
- Van der Linden, R. A. M. & the SIDC team, online catalogue of the sunspot index, <http://www.sidc.be/sunspot-data/>
- Veronig, A. M., & Brown, J. C. 2004, *ApJ*, 603, L117
- Yashiro, S., Gopalswamy, N., Michalek, G., St. Cyr, O. C., Plunkett, S. P., Rich, N. B., & Howard, R. A. 2004, *J. Geophys. Res.*, 7105

Zharkova, V. V., & Gordovsky, M. 2005, ESA SP-600: "The Dynamic Sun: Challenges for Theory and Observations", 147.1

Zioutas, K., Dennerl, K., DiLella, L., Hoffmann, D. H. H., Jacoby, J., & Papaevangelou, T. 2004, ApJ, 607, 575